

**A 4,600-YEAR STALAGMITE HIGH RESOLUTION GEOCHEMICAL AND PETROLOGIC
PALEOCLIMATE RECORD FOR NORTHEAST NAMIBIA**

by

HILLARY R. SLETTEN

(Under the direction of L. Bruce Railsback)

ABSTRACT

Multiple lines of evidence from an aragonite and calcite stalagmite from northeastern Namibia combine to provide a 4600-yr record of climate change. U/Th-series dating indicates that three episodes of very slow deposition ($S(n)$), occurred at ca. 3000 to 2060 BP ($S3$), 1120 to 800 BP ($S2$), and 600 to 370 BP ($S1$). Each of these intervals of slower growth is coincident with greater $\delta^{13}\text{C}$ and $\delta^{18}\text{O}$, a decrease in stalagmite width, deposition of aragonite, and variations in petrographic fabrics that indicate a positive correlation between greater $\delta^{13}\text{C}$ and increased crystal widths. All three S_n periods show both in and out-of-phase relationships with other southern African paleoclimate records that suggest evidence of climate change within the Little Ice Age (AD 1300-1800) and before the Medieval Warm Period (AD 1000-1300), respectively. The synthesis is one the first high-resolution paleoclimate records for this region of Namibia.

INDEX WORDS: Holocene, Paleoclimate, Stalagmite, Namibia, Petrography, Fabric, Aragonite,
Calcite

**A 4,600-YEAR STALAGMITE HIGH RESOLUTION GEOCHEMICAL AND PETROLOGIC
PALEOCLIMATE RECORD FOR NORTHEAST NAMIBIA**

by

HILLARY R. SLETTEN

B.S., The University of Dayton, 2005

A Thesis Submitted to the Graduate Faculty of The University of Georgia in Partial Fulfillment of the
Requirements for the Degree

MASTER OF SCIENCE

ATHENS, GEORGIA

2011

© 2011

Hillary R. Sletten

All Rights Reserved

**A 4,600-YEAR STALAGMITE HIGH RESOLUTION GEOCHEMICAL AND PETROLOGIC
PALEOCLIMATE RECORD FOR NORTHEAST NAMIBIA**

by

HILLARY R. SLETTEN

Major Professor: L. Bruce Railsback

Committee: George A. Brook
Douglas E. Crowe

Electronic Version Approved:

Maureen Grasso
Dean of the Graduate School
The University of Georgia
May 2011

ACKNOWLEDGEMENTS

“Coming together is a beginning. Keeping together is progress. Working together is success.”

~ Henry Ford ~

With this in mind, I give my warm thanks to the many collaborators and supporters of my master’s thesis research, education, and personal well-being. To Dr. L. Bruce Railsback for his patience in mentoring, attention to detail, and passion for teaching about the world of carbonates. To Dr. George Brook for providing the stalagmite (DP1) I investigated in this thesis project, for providing funding from his NSF grant under award abstract #0725090, and for lending his knowledge of and experience with southern African paleoclimate research. To Dr. Doug Crowe for serving on my committee and providing pointed advice when needed. To Keystone Granite Company in Elberton, Georgia for cutting DP1 free of charge. To Eugene Marais of the National Museum of Namibia for providing access to, and knowledge about Dante Cave, as well as assisting with the collection of DP1 with Ben Hardt from the University of Minnesota. To Julie Cox who trained me in how to operate the stable isotope lab equipment, assisted with sample processing, and was always available for questions when needed (even at 10 PM at night!). To Dr. Larry Edwards and Hai Cheng for their collaboration for the U-series dating of DP1 at the University of Minnesota Stable Isotope Laboratory. To Dr. Joe Lambert for running stable isotope samples on short notice and for opening the gates to the University of Alabama for me! To my research assistants: Tony Gesualdo for his time and effort in the XRD lab, and Joelle Freeman, for her patience and expertise while assisting with GIS figures. To my fellow grad students at the University of Georgia who have supported me in a variety of known and unknown ways during the past two years. And finally, to my friends and family, near and far, who have all extended their kindness and support in so many ways. All of you have helped jumpstart my academic career, bridge and mend my defeats, and pave pathways to success. Thank you!

TABLE OF CONTENTS

	Page
ACKNOWLEDGEMENTS	iv
LIST OF TABLES	vii
LIST OF FIGURES	viii
LIST OF ABBREVIATIONS AND SYMBOLS	ix
CHAPTER	
1 INTRODUCTION	1
1.1 Previous Paleoclimate Studies in Southern Africa.....	1
1.2 Stalagmites as Paleoclimate Records.....	1
1.3 Purpose of Study.....	7
2 GEOLOGY AND CLIMATE.....	8
2.1 Background.....	8
2.2 Geologic and Speleologic Setting	8
2.3 Environment and Climate Setting	9
3 HOLOCENE PALEOCLIMATE OF SOUTHERN AFRICA.....	16
3.1 Introduction to Southern African Geoarchives.....	16
3.2 Geoarchives	16
4 METHODS	24
4.1 General Description and Sampling	24
4.2 Age Dating and Growth Rate.....	24
4.3 C and O Stable Isotope Analysis	25

4.4 Mineralogy and Luminescence.....	26
4.5 Petrography.....	27
5 RESULTS.....	38
5.1 Age Model.....	38
5.2 Stable Isotope Data.....	38
5.3 Petrographic and Fabric Analysis.....	39
5.4 Dry and Wet Periods.....	42
6 DISSCUSSION.....	51
6.1 $\delta^{13}\text{C}$ and $\delta^{18}\text{O}$ Relationships to Sn Periods.....	51
6.2 Potential Causes of Alternating Aragonite and Calcite in DP1.....	52
6.3 Isotopic Variation with Differences in DP1 Fabric Classifications.....	54
6.4 DP1 Correlations to Other Southern African Paleoclimate Records.....	56
6.5 DP1 Correlation to Global Paleoclimate Records.....	58
7 CONCLUSIONS.....	64
REFERENCES	65
APPENDICES	
A DP1 SAMPLE, STABLE ISOTOPE, AND FABRIC DATA.....	72

LIST OF TABLES

	Page
Table 4.1: Start and end depths for DP1 thin sections	31
Table 4.2.a: Columnar calcite fabric classification descriptions	32
Table 4.2.b: Coarse aragonite fabric classification descriptions.....	33
Table 4.2.c: Needle aragonite fabric classification descriptions.....	34
Table 4.2.d: Massive needle aragonite fabric classification descriptions.....	35
Table 4.2.e: Massive botryoidal needle aragonite fabric classification descriptions.....	36
Table 4.2.f: Interwoven aragonite fabric classification descriptions.....	37
Table 5.1: Uranium and thorium isotopic compositions and ^{230}Th ages for DP1	43
Table 5.2: Summary of slow growth periods S1 to S3 for DP1.....	49
Table 5.3: Summary of slow growth interval (Sn) characteristics	50

LIST OF FIGURES

	Page
Figure 2.1: Site location map of Dante Cave.....	11
Figure 2.2: Biomes of Namibia.....	12
Figure 2.3: Grass cover of Namibia.....	12
Figure 2.4: Average annual temperatures in Namibia.....	13
Figure 2.5: Average annual rainfall of Namibia.....	14
Figure 2.6: Relative humidity values during the least humid months in Namibia.....	15
Figure 2.7: Relative humidity values during the most humid months in Namibia.....	15
Figure 3.1: Site locations of southern African paleoclimate studies discussed in Chapter 3.....	23
Figure 4.1: Stalagmite DP1 from Dante Cave in northeast Namibia.....	29
Figure 4.2: Photographs of analytical methods.....	30
Figure 5.1: Calculated growth rates (mm/yr) between 23 U/Th dated intervals for DP1.....	44
Figure 5.2: Photomicrographs of dissolution and aridification features.....	45
Figure 5.3: DP1 fabrics for 243 of 287 stable isotope values.....	46
Figure 5.4: Photomicrographs of a fabric progression from 1005 to 977 mm.....	47
Figure 5.5: DP1 time series using $\delta^{13}\text{C}$ and $\delta^{18}\text{O}$	48
Figure 6.1: Comparison of DP1 to other southern African Quaternary paleoclimate records.....	61
Figure 6.2: Holocene paleoclimate records in southern Africa.....	62
Figure 6.3: DP1 compared to the NorthGRIP ice core $\delta^{18}\text{O}$ record.....	63

LIST OF ABBREVIATIONS AND SYMBOLS

AD	anno domini	p _{CO2}	partial pressure of CO ₂
BC	before Christ	PDB	Pee Dee Belemnite
BP	before present (1950)	SMOW	standard mean ocean water
°C	degrees Celsius	Sn	slow growth interval
C	carbon	SST	seawater surface temperature
.ca	approximately	U/Th	uranium/thorium
Ca	calcium	UGA	The University of Georgia
CA	coarse aragonite	UV	ultra-violet
CAB	Congo Air Boundary	VPDB	Vienna Pee Dee Belemnite
CaCO ₃	calcium carbonate	XRD	X-ray diffraction
CC	columnar calcite	‰	per mil
cal yr.	calendar year		
cm	centimeters		
CO ₂	carbon dioxide		
DIC	dissolved inorganic carbon		
DOC	dissolved organic carbon		
DPI	Dante Purgatory 1		
g	grams		
H ₂ O	water		
H ₃ PO ₄	phosphoric acid		
IA	interwoven aragonite		
ICP-MS	inductively-coupled plasma mass spectrometer		
IPL	Impulse Photography of Luminescence		
ITCZ	Inter-tropical Convergence Zone		
LIA	Little Ice Age		
m	meters		
m ²	square meters		
Ma	million years		
mm	millimeters		
MWP	Medieval Warm Period		
MNA	massive needle aragonite		
MBNA	massive botryoidal needle aragonite		
µg	micrograms		

CHAPTER 1

INTRODUCTION

1.1 Previous Paleoclimate Studies in Southern Africa

Very few high-resolution, continuous terrestrial paleoclimate records exist for southern Africa, and even fewer in Namibia (Maslin and Christensen, 2007). To date, only two pre-existing high-resolution records have been interpreted for Namibia, both of which cover portions of the Holocene period (11,500 cal yr BP to the present). Identifying dry versus wet periods during the Holocene is of particular interest because there is a need to know about the natural variability underlying anthropogenic climate change, both on a regional and global scale (Mayewski et al., 2004). Patterns in natural variability are being determined by linking paleoclimate records together across the world, from terrestrial, marine, and glacial sources. As more records are studied, anthropogenic causes can be increasingly distinguished from natural causes as more information is collected about the triggers for dry and wet periods through time.

The drying and wetting cycles associated with semi-arid climates in southern Africa are not favorable for preserving traditional organic proxy data sources (Chase, 2009). This has resulted in sparse, geographically scattered, and often poorly dated high-resolution Holocene records. Despite the difficulty and inconsistencies in data collection and or interpretation, dry and wet periods have been documented in numerous paleo-proxies such as marine, dune and lake sediments, pollen, hyrax middens, and stalagmites. Of these, stalagmites may be one of the most useful climate proxies available.

1.2 Stalagmites as Paleoclimate Records

Stalagmites are secondary cave mineral deposits that form in karst environments through a series of precipitation and dissolution processes. Stalagmites are most commonly formed as a result of drip water exiting a bedrock fracture into an open-air cave, which then degasses while falling from the cave ceiling. During the process of degassing, the drip water releases carbon dioxide (CO₂) and becomes supersaturated with respect to calcium carbonate (CaCO₃). This causes the drip water to form a solid

mineral when it hits a surface. Stalagmites can grow for up to hundreds of thousands of years if not significantly disturbed. Caves provide an optimal environment to protect stalagmites, while still allowing them to be influenced by outdoor conditions for they are typically considered to have air temperatures that are constant and approximately the mean annual temperature of air outside the cave (McDermott et al., 2005).

In response to this relationship, stalagmites have been used as multi-proxy paleoclimate records for over 40 years to identify changes in climate such as rainfall variability, mean annual temperature, atmospheric circulation, and vegetation response to climate shifts. These variations are recorded in measurable parameters including stable isotope ratios (Hendy and Wilson, 1968; McDermott, 2004), mineralogy and inter-annual variations in growth laminae (Railsback et al., 1994), organic content (Ford, 1997), and growth rate change (McDermott, 2004). Most importantly, stalagmites can be precisely and absolutely dated using Uranium/Thorium (U/Th) methods (Edwards et al., 1988; Shen et al., 2002) allowing for fairly accurate time correlations with other climate records.

Interpretations from these proxies are correlated with other climate records (both instrumental and non-instrumental) to project future climate change or retrodict past climate. Past climate from stalagmites can be interpreted either broadly into warm and cool periods using well-dated stable isotope records, or more specifically into paleotemperature values. The latter method, however, is typically too complex to derive accurate paleotemperatures due to the multiple controls on the stable isotope system (McDermott, 2004) and is potentially not the most accurate method of stalagmite paleoclimate reconstruction. For this study, we made broad interpretations using stable isotope ratios combined with mineralogical, growth rate, petrographic, and luminescence data.

1.2.1 Mineralogy

The mineralogy of stalagmites is typically aragonite and calcite, two polymorphs of CaCO_3 . What triggers one to form instead of the other, especially in spelean environments, is still not fully understood. For carbonates in general, there are many suppositions as to why one preferentially precipitates over the other including: (1) enriched Mg/Ca ratios in solutions from bedrock sources that are more likely to form

aragonite (Berner, 1975); (2) the presence of sulfate, phosphate (Walter, 1986), iron (Meyer, 1984), or dissolved organic carbon (DOC) (Lebron and Suarez, 1996) in the drip solution; (3) temperature and evaporation variations (Walter, 1986; Harmon et al., 1983) (4) fluctuations in seasonal rainfall (Railsback, et al., 1994); and (5) CaCO_3 precipitation rate (Given and Wilkinson, 1985). Some, or all of these variables could cause one CaCO_3 polymorph to preferentially precipitate in spelean environments. For stalagmites, for instance, Railsback et al. (1994) conducted a study in Drotzky's Cave, Botswana where they observed that Mg/Ca ratios in calcite layers increased upward to the base of aragonite layers and that fluid Mg/Ca ratios in drip water were adequate for aragonite precipitation. Railsback et al. (1994) suggested that these factors, combined with increased evaporation within the cave, caused aragonite to form.

Both aragonite and calcite can aid in the interpretation of distinguishing dry and wet periods. In general, aragonite tends to form in response to greater supersaturation with respect to calcite, and forms in drier, more arid climates. Finch et al. (2003) have shown that aragonitic stalagmites are remarkably good indicators of rapid changes in climate such as past periods of drought at Cold Air Cave, South Africa. It has also been observed that massive aragonite, independent of the overlying bedrock being limestone or dolomite, is found in relatively warm caves (temperatures $>12^\circ\text{C}$) (Cabrol (1978); Frisia et al., (2002)) and since cave temperatures are representative of mean outdoor air temperature above the cave (McDermott et al., 2005), aragonite precipitation is often associated with drier climates. Conversely, the presence of calcite in stalagmites is likely related to the amount of rainfall, with relatively wetter conditions providing a "normal" or steady drip to flow over the stalagmite and promote calcite growth (Railsback et al., 1994).

1.2.2 Petrography

Carbonate petrographers concerned with crystal growth often study crystal morphology (width, length ratios, and elongation), habit (general appearance of faces or set of faces), and fabric (general appearance of a set of crystals that grow to form a textural pattern of crystals) (Gonzalez et al., 1992; Folk, 1974; Lahann, 1978; Given and Wilkinson, 1985). The petrographic study of spelean fabrics is a useful

parameter for paleoenvironmental studies, but is a widely underutilized method (Frisia et al., 2000). Of the research that has been conducted on stalagmite fabrics, most of the studies have been focused on calcite with little attention given to aragonite fabrics due to the greater number of calcite speleothems available to the researchers analyzing fabrics (Gonzalez et al., 1992; Frisia et al., 2000; Frisia et al., 2002). Given that calcite and aragonite are polymorphs, it is likely that similar mechanisms influence morphology, habit, and fabric structures.

Stalagmite petrographic studies have been conducted to determine environmental controls on the formation of carbonate layers, crystal morphology, and growth mechanisms. Railsback et al. (1994) used petrography to distinguish composite calcite and aragonite layers and to find that calcite layer thickness correlated with rainfall, such that thicker layers signified greater amounts of rainfall. Both calcite and aragonite layer thicknesses were found to correlate with temperature. Railsback et al. (2011) identified 18 petrographic surfaces in a stalagmite from Cova da Arcoia in the Serra do Courel of northwestern Spain to differentiate between enhanced (E) and low (L) flow drip water conditions. The presence of E surfaces was interpreted to mean wetter conditions; the presence of L surfaces meant drier phases.

Frisia et al. (2000) approached stalagmite petrographic studies by identifying and correlating fabrics with drip water parameters from active calcite stalagmites from the Italian Alps and southwestern Ireland. They compared isotopic values for some variations in fabrics to make inferences about morphology, and to conclude that supersaturation and discharge of the drip water caused differences in the types of fabrics that formed instead of other controls such as temperature. Because the supersaturation and the amount of discharge supplying a stalagmite are linked to the amount of regional rainfall, fabrics are potential markers for distinguishing dry and wet periods. Brook et al. (2010) also loosely compared isotopic values with variations in calcite fabrics using a stalagmite from Wonderwerk Cave, South Africa. They found that layered and microstromatolitic fabrics were formed during slower growth periods and had greater $\delta^{13}\text{C}$ and $\delta^{18}\text{O}$ values as compared to the concretionary fabric that formed during wetter periods characterized by lower $\delta^{13}\text{C}$ and $\delta^{18}\text{O}$ values. Petrographic, and particularly fabric

analyses, can thus provide another tool for paleoclimate interpretation instead of relying solely on isotopic or trace element data.

1.2.3 Luminescence

Luminescence is the process in which an atom, a molecule, or a crystal structure in a high energy or excited state relaxes to a lower energy state by emitting a photon (Baker et al., 1996). It results in either fluorescence, which is a fast energy transition from a singlet to another singlet, or in phosphorescence, which is a slow energy transfer from a triplet to a singlet. In stalagmites, as well as other speleothems, luminescence occurs when an ultra-violet (UV) or high-energy light source are applied, exciting molecules of humic and fulvic acids from organic plant material present within the CaCO_3 . Different energy sources cause different forms of luminescence including: (1) photoluminescence caused by UV or other light-source excitation, (2) X-ray luminescence produced by the excitation of the electrons by X-rays, (3) cathodoluminescence by electron-beam excitation, (4) thermoluminescence caused by heating, (5) candoluminescence caused by exposure to flames, and (6) triboluminescence caused by crushing (Shopov, 2006). Photoluminescence using the Impulse Photography of Luminescence (IPL) is the most common non-destructive, light-source method. Because luminescence is the property most sensitive to depositional conditions in cave minerals, these different analyses can be used to make paleoclimate inferences about climate (Tarashtan (1978); Shopov (1997)). With the aid of calibrations and models, variations in luminescence can potentially correlate to parameters such as the amount of vegetation cover, percent soil moisture, and degree of temperature above the cave (Baker et al., 1998).

1.2.4 C and O Stable Isotopes

Incorporated within CaCO_3 are carbon (C) and oxygen (O), each of which consists of stable isotopes that, when measured, provide a ratio that can be used to interpret past climate. The stable isotope ratios used include $^{13}\text{C}/^{12}\text{C}$, which varies in response to changes in the vegetation cover above the cave, and $^{18}\text{O}/^{16}\text{O}$, which varies in response to the amount of rainfall above the cave. The amount of rainfall has a direct relationship to the amount of vegetation growing above a cave, where greater $\delta^{13}\text{C}$ and $\delta^{18}\text{O}$ represent less

rainfall, less vegetation, and drier climate conditions (Repinski et al., 1999). Conversely, $\delta^{13}\text{C}$ and $\delta^{18}\text{O}$ represent more rainfall, more vegetation, and wetter climate conditions (McDermott et al., 2005).

This relationship further reflects the type of vegetation growing above a cave system. The isotopic signature from decaying plant material in the soil profile is incorporated in the precipitated spelean CaCO_3 . Dissolved inorganic content (DIC) from the plants reflects different types of plants because they produce different isotopic signatures within their cellular structures based on their metabolic processes in the photosynthetic pathway. The photosynthetic pathway of the plants are linked to climate, where C3 plants include trees and shrubs and are associated with more cooler/wetter conditions and C4 plants, which are dominated by grasses, typically grow in warmer/drier conditions (Cerling, 1999). For southern Africa, Bar-Matthews et al. (2010) have offered an opposing view based on studies in South Africa where C3 plants grow in warmer/wetter conditions (summer rainfall season) and C4 plants grow in cooler/drier conditions (winter rainfall season). For this study, we have ascribed to the interpretation by Cerling (1999) based on combined data results from the stalagmite under investigation, DP1.

In a C3 plant system, the DIC in percolating solution is about -14‰ to -18‰ when the solution becomes saturated with respect to CaCO_3 (McDermott, 2004). In a closed system, isolated percolating water reflects both the soil CO_2 and the signature of the dissolving bedrock. In a C3 system, with soil gas $\delta^{13}\text{C}$ of about -23‰ and a limestone bedrock with $\delta^{13}\text{C}$ of +1‰, the DIC $\delta^{13}\text{C}$ is usually about -11‰. In speleothem carbonate, the $\delta^{13}\text{C}$ values for C4 plants are +1‰, whereas $\delta^{13}\text{C}$ values for C3 plants are around -13‰ (Holmgren et al., 1999; Talma and Vogel, 1992). Upon deposition in an open or closed system, $\delta^{13}\text{C}$ for C4 and C3 plant signatures in speleothem calcite should be -12‰ to -8‰ and -2.3‰ to +1.5‰, respectively (Brook, 1999). In southern Africa, Holmgren et al. (2003) suggest that the $\delta^{13}\text{C}$ variations show transitions between C3 and C4 biomes, whereas Holzkämper et al. (2009) identify these variations as the relative dominance of C3 and C4 at the cave location.

In comparison, meteoric water moving through an open system dissolves much less of the bedrock because it does not have an indefinite supply of CO_2 in the soil to supply the bicarbonate reaction. The percolating water, therefore, does not reflect the carbon isotope signal from the bedrock

(McDermott et al., 2005). The $\delta^{13}\text{C}$ values for DIC are about -11‰ for C3 systems where the soil vapor $\delta^{13}\text{C}$ is about -23‰ and the bedrock has a $\delta^{13}\text{C}$ of +1‰ (McDermott, 2005). Most natural systems are partially to fully open, which allows for continuous meteoric water flow and dissolution through the phreatic zone.

1.3 Purpose of Study

Stalagmite Dante Purgatory 1 (DP1) from northeastern Namibia is ca. 16-yr interval climate record for the past 4600 cal yr BP, making it the first high-resolution paleoclimate record for this region, and the first stalagmite paleoclimate record for Namibia. In addition to contributing a new climate record to Namibia and southern Africa, we used multi-proxy methods to test the following hypotheses:

- (1) Increased amounts of precipitation fell above Dante Cave that caused DP1 to shift from narrow, consistent growth layers of aragonite to wider, more inconsistent layers of alternating aragonite and calcite deposition.
- (2) DP1 layers that have lower $\delta^{13}\text{C}$ values show relative variations in calcite growth patterns and fabrics, which are indicative of wetter climate conditions above Dante Cave.
- (3) DP1 layers that have greater $\delta^{13}\text{C}$ values show relative variations in aragonite growth patterns and fabrics, which are indicative of drier climate conditions above Dante Cave.
- (4) A classification of different petrographic crystal fabrics in DP1 can correlate and show a positive relationship with stable C and O isotope values for each sample interval to explain variations in paleoclimate.
- (5) Dry and wet periods can be delineated by combining observations of isotope data, growth rate, mineralogy, fabric classifications, dissolution surface features between layer boundaries, and relative presence of organic content.
- (6): DP1 is a datable stalagmite record that can be correlated with other regional and southern African climate records indicating similar periods of change.

CHAPTER 2

GEOLOGY AND CLIMATE

2.1 Background

The stalagmite under investigation, DP1, was collected in 2006 by Eugene Marais of the National Museum of Namibia and University of Minnesota graduate student Ben Hardt. Marais and Hardt found the inactive stalagmite lying on the ground of Dante Cave in northeast Namibia in a bottom chamber named “Purgatory”.

2.2 Geologic and Speleologic Setting¹

Dante Cave is located on the Ghaub Guest Farm (19° 28' 15" S; 17° 44' 58" E) in the Oshikoto Region of the Tsumeb District of Namibia (Figure 2.1). It is situated on the northeastern margin of the Otavi Mountainland, also referred to as the Karstveld. This is the only continuous karstic environment in Namibia (Irish et al., 2001) and includes a few very large underground lakes such as Dragonsbreath (surface area > 25,000 m²; depth >93 m) and Harasib (surface area 8900 m²; depth > 110 m). Overall, the Otavi Mountainland is characterized by poorly developed underground karst. The longest of more than 50 known caves in the area include Pofadder (2812 m), Ghaub (2708 m), and Dante (828 m; depth 65 m). Dante Cave consists of a number of medium sized chambers connected by serpentine passages. Access to the cave is through a single vertical entrance in the roof of the southernmost chamber, 9 m above a debris cone of collapsed rock. Steep solution passages lead to deeper chambers and passages at depths of about 40 to 60 m below the entrance level.

Dante Cave is capped and underlain by dolomite within the upper Tsumeb Subgroup within the Otavi Group. Carbonates of this group were deposited between 730 and 700 Ma during two cycles of deposition, now recorded as the Abenab and Tsumeb Subgroups (Miller, 1997). The Otavi Group is a

¹ Much of the information in this section about the environment and climate near Dante Cave was provided in a personal communication from Eugene Marais in 2011.

carbonate succession in the northern part of the Damara Orogen now known as the Damara Supergroup Complex (Figure 2.1) (Miller, 1983).

2.3 Environment and Climatic Setting

The present day vegetation above Dante Cave consists of deciduous woodland savanna (Mendelsohn et al., 2002) with a relatively high diversity of scattered tall trees within an area of smaller trees and shrubs. This vegetation occurs mostly where shallow soils (0 to 20 cm) form in pockets between large boulders and solution hollows in the dolomites, with open areas consisting of bare rock, or with a very thin covering of soil. Regionally, the shrub cover is 51 to 57% (Figure 2.2). The grass cover around the cave is sparse and dominated by annuals. This region has approximately 26 to 50% grass cover (Figure 2.3).

According to the Köppen-Geiger climate classification scheme (Kottek et al., 2006), the Oshikoto Region is considered a semi-arid climate where there is less rainfall than there is evapotranspiration. The mean annual temperature for a 17-yr period at the nearby Grootfontein meteorological station, 30 km away, is 21.0 ± 3.3 °C, though there is a marked seasonality in the air temperature with a mean austral summer (NDJ) temperature of 24°C and a mean winter temperature (MJJ) of 16°C (Figure 2.4).

The Oshikoto Region is located within the summer rainfall zone, where the majority of the rainfall occurs in the eight summer months from October to May. Mean rainfall at Grootfontein is 532 mm per annum (as determined over 65 years) with most rainfall expected during the JFM period, though the rainfall amount may vary by more than 600 mm yr^{-1} between individual years (rainfall ± 176.6). Other rainfall stations in the Otavi Mountainland such as Tsumeb (501 mm yr^{-1}), Otavi (519 mm yr^{-1}), and Ghaub (587 mm yr^{-1}) indicate the variability that may occur (Figure 2.5).

Due to the orographic effect of the Otavi Mountainland, which intercepts moisture influx from the northeast, the Mountainland forms an outlier with greater rainfall within the arid interior of Namibia. Evapotranspiration is thus greater with a potential evaporation of 2900 mm yr^{-1} and maximum evaporation rates from October to December, leading to a negative theoretical water balance for most of

the year. During the most humid months (NDJ), relative humidity is >90% whereas during the least humid months is 10 to 20% (Figures 2.6 and 2.7).

Precipitation in the Oshikoto and surrounding regions of southern Africa is driven predominantly by the Inter-Tropical Convergence Zone (ITCZ), the Subtropical High Pressure Zone, the Temperate Zone (Heine, 2005), and the Congo Air Boundary (CAB) between the Atlantic and Indian Oceans (Tyson, 1986). The ITCZ is a convective air mass pattern that shifts on an annual and seasonal basis, such that in winter the ITCZ and subsequent rain belts move into the Northern Hemisphere. In summer the ITCZ moves back into the Southern Hemisphere, creating a region of latent heat release in the southern African tropics. When the CAB moves southwest it generates tropical rainfall. Mid-latitude disturbances to these patterns impact the amount of annual and seasonal precipitation. The Subtropical High Pressure Zone, in association with the northward flowing cool Benguela upwelling current, create hyper-arid conditions, stronger winds, lower temperatures, and varying humidity (Heine, 2005; Gil-Romera et al., 2007; Tyson, 1986).

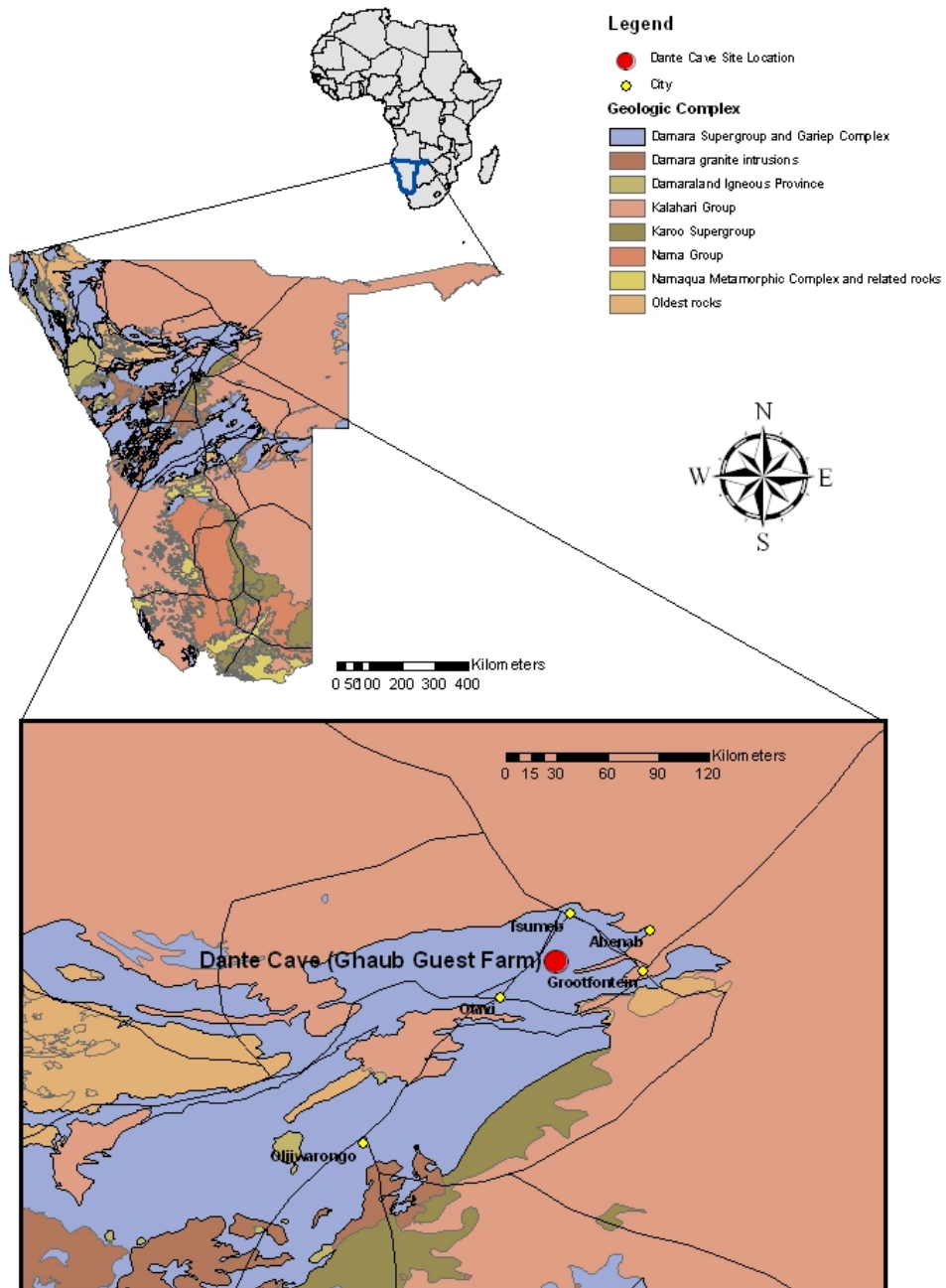


Figure 2.1. Site location map of Dante Cave located on the Ghaub Guest Farm, Oshikoto Region, northeast Namibia.

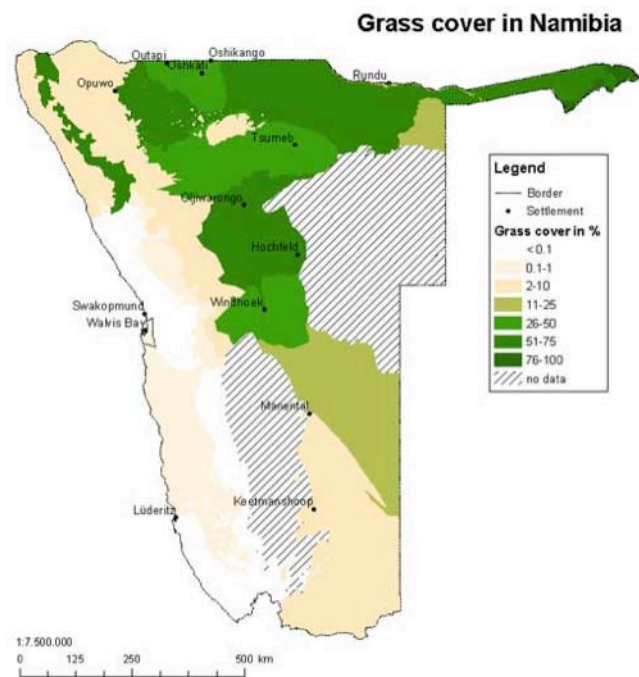
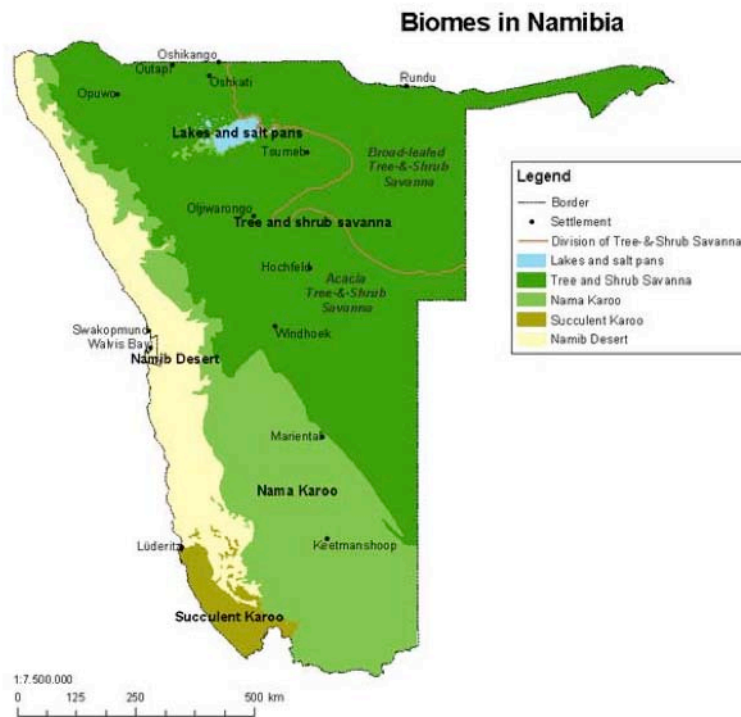


Figure 2.2. Biomes of Namibia. Figure 2.3. Grass cover of Namibia. (Maps produced by E1, 2003.)

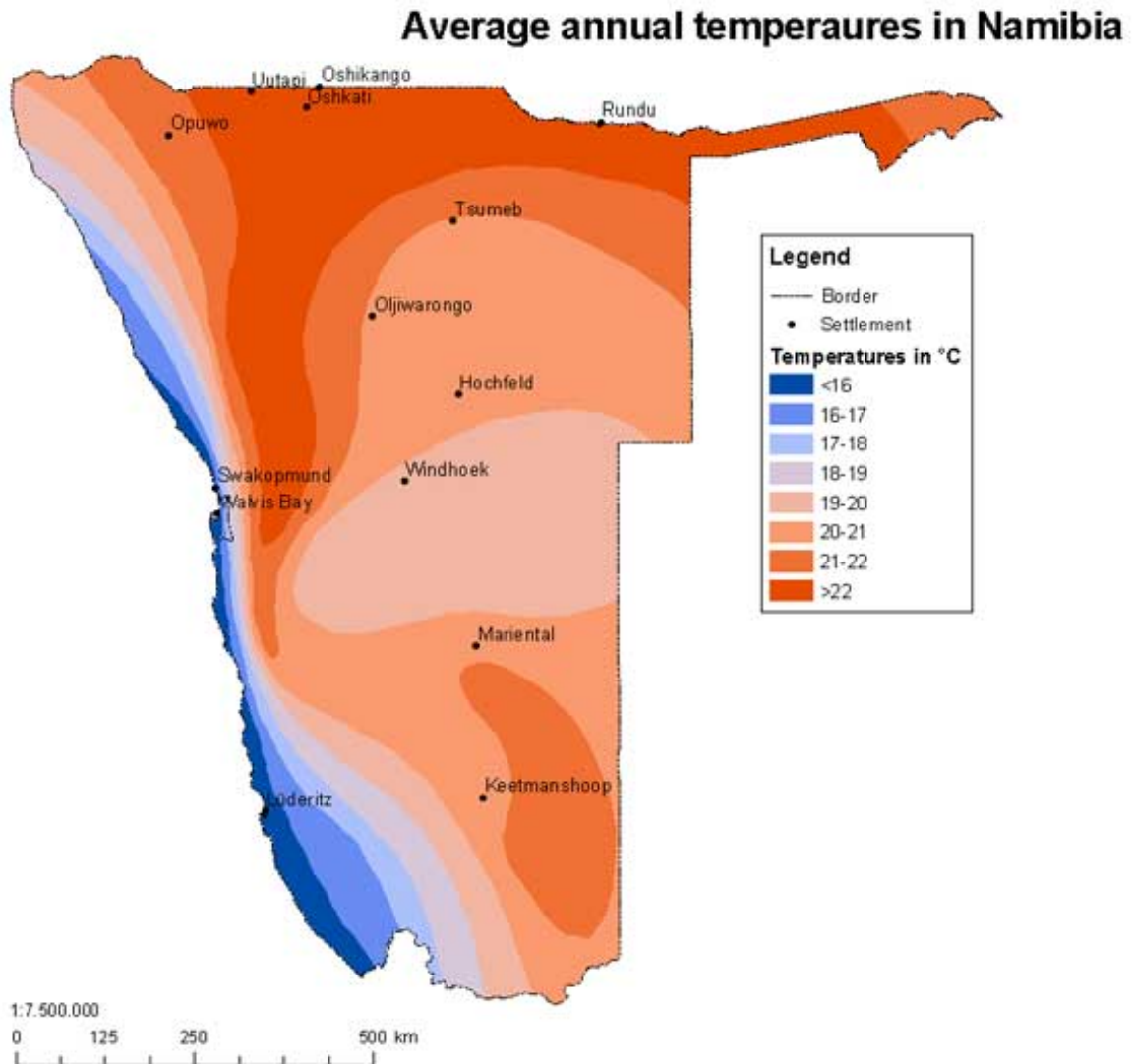


Figure 2.4. Average annual temperatures in Namibia (Map produced by E1, 2003.)

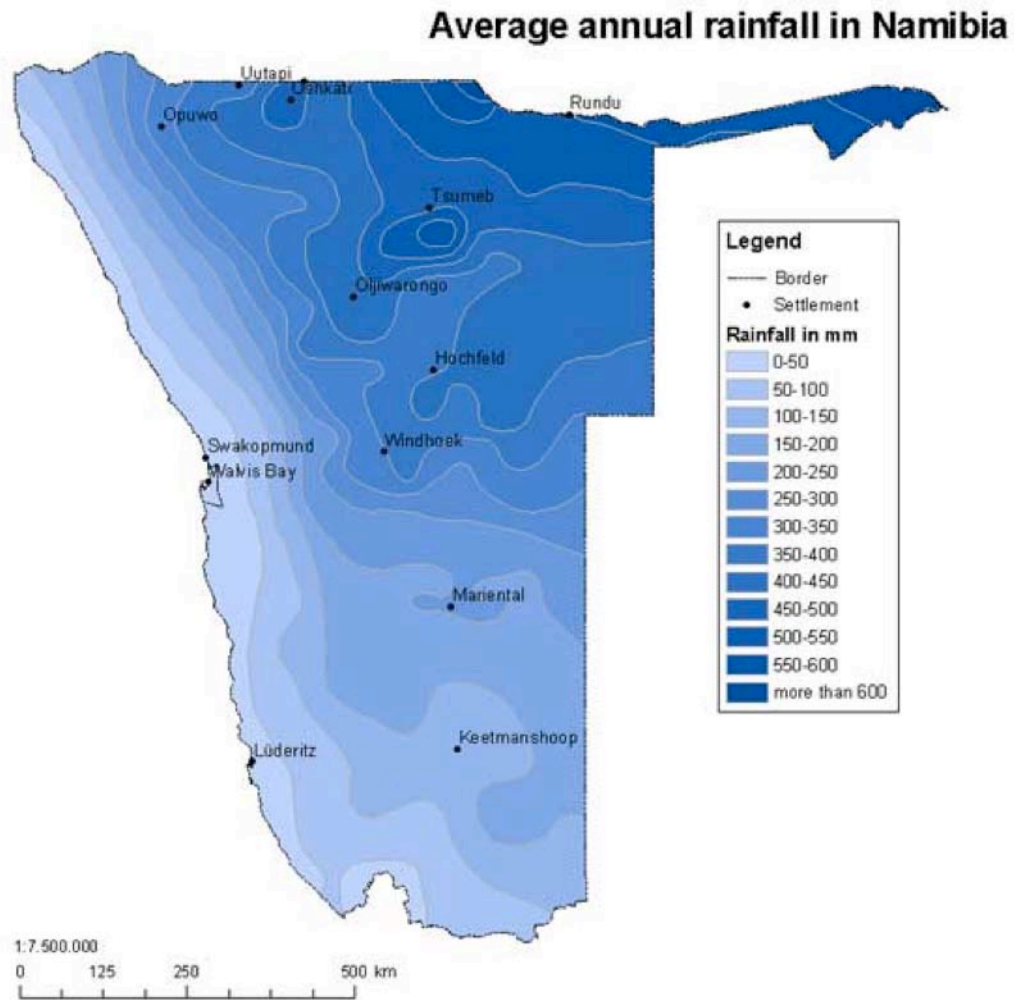


Figure 2.5. Average annual rainfall of Namibia. (Map produced by E1, 2003.)

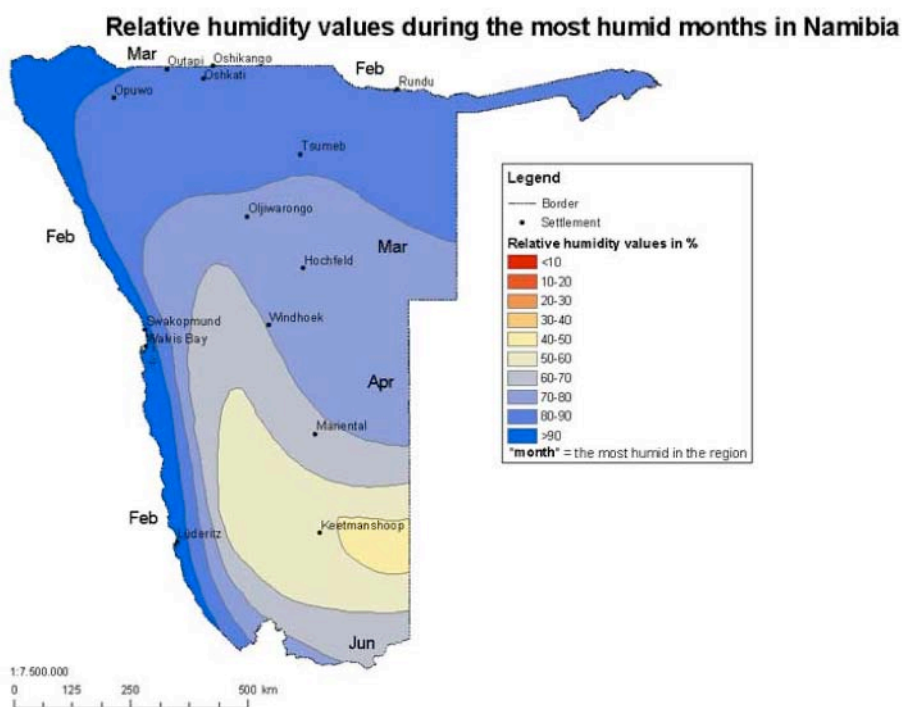
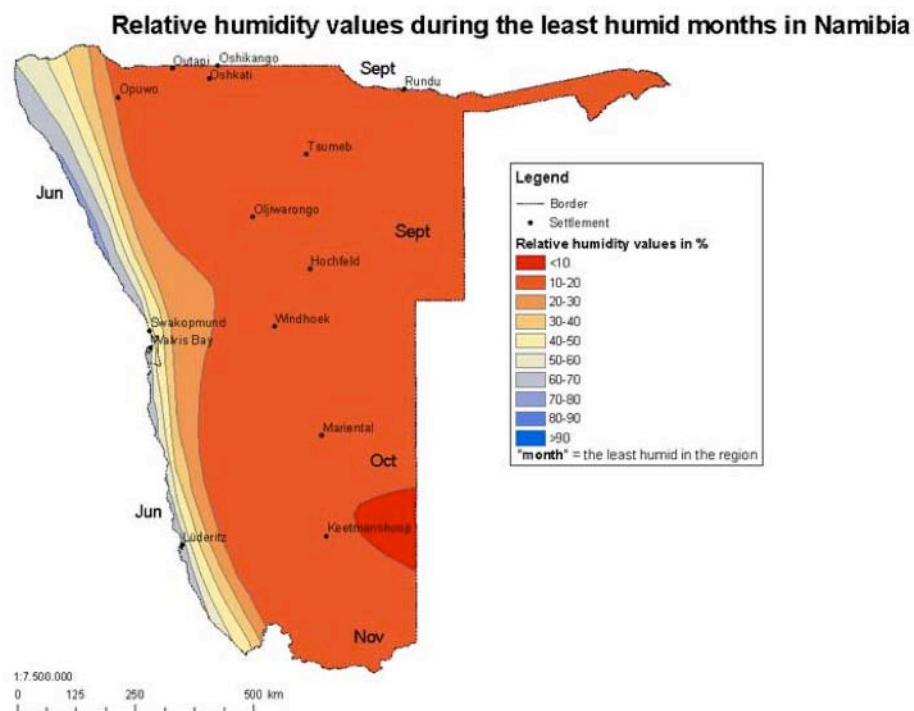


Figure 2.6. Relative humidity values during the least humid months in Namibia. Figure 2.7. Relative humidity values during the most humid months in Namibia (Maps produced by E1, 2003.)

CHAPTER 3

HOLOCENE PALEOCLIMATE OF SOUTHERN AFRICA

3.1 Introduction to Southern African Geoarchives

Holocene paleoclimates of southern Africa can be determined using a variety of geoarchives including (a) dunes, (b) cave deposits, (c) fluvial deposits, (d) slope deposits, (e) soils, (f) marine sediments, (g) groundwater, (h) pollen and hyrax dung, (i) trees, (j) molluscs and ostracods, (k) sebhka deposits, and (l) archaeological data. The data most relevant to this study come from cave deposits, pollen, and hyrax middens, and dune sediments with emphasis on records pertaining to the past 5000 cal yrs BP. The locations of the paleoclimate study sites discussed in this chapter are shown in Figure 3.1.

3.2 Geoarchives

3.2.1 Holocene Cave Deposits

One of the first southern African caves to be studied for paleoclimatological research was Echo Cave located in the Mogaba district of the eastern Transvaal, South Africa. Brook (1982) used travertine and sediment deposits from Echo Cave, along with other data from sites in Botswana and northeastern South Africa, to determine three cooler and wetter phases during the Holocene at 9700 to 7600, 7300 to 2200, and 1700 to 400 BP. For Echo Cave, Brook determined four climate phases and water table levels by identifying locations where and when cave formations formed. Wetter climates minimized or prohibited speleothem growth in the cave by raising the water table and filling lower chambers with water (Phases I, II, and III). Drier conditions stabilized between 11,500 and 7500 BP, which lowered the water table and re-established speleothem deposition (Phase IV).

The single most continuous temperature record from caves in southern Africa comes from a 30,000-yr stalagmite from Cango Cave, Southern Cape, South Africa. Talma and Vogel (1992) determined $\delta^{18}\text{O}$ values along a 2.6 m long growth axis. Using ^{14}C dated samples and $\delta^{18}\text{O}$ values from

the artesian Uitenhage aquifer, they were able to estimate the $\delta^{18}\text{O}$ of cave drip water from the past using Craig's (1965) expression. Talma and Vogel (1992) found that temperatures were more or less constant during the past 5000 years and 4 to 7°C lower than temperatures today from 30,000 to 13,800 BP. Results indicated that $\delta^{13}\text{C}$ shifted from values near -11‰ PDB at 47,000 BP, increasing to -5‰ between 5000 and 2000 BP, and then decreasing to present-day values near -7‰ (Talma and Vogel, 1992). Concluding that stalagmite formation at Cango Cave took place in an open system, Talma and Vogel (1992) determined that vegetation cover could be used as a climate indicator. Isotopic results indicated that C3 plants almost completely covered the landscape near the last glacial maximum, and starting at about 5000 BP, C4 plants progressively increased with a $\delta^{13}\text{C}$ maximum at about 2000 BP. Talma and Vogel associated C4 plants with a wet growing season, which is contradictory to the majority of vegetation climate models.

Holmgren et al. (1999) reported the first high-resolution stalagmite paleoclimate record for southern Africa using a 6600-yr stalagmite (T7) from Cold Air Cave, Makapansgat Valley, Northern Province, South Africa. They sampled 0.5 m of the 1 m T7 stalagmite along the central growth axis at approximately 2 mm for $\delta^{13}\text{C}$. This resulted in a 3000-yr record with 10-yr intervals between samples. Using the Hendy Test (Hendy, 1971), Holmgren et al. (1999) found there to be no correlation between $\delta^{13}\text{C}$ and $\delta^{18}\text{O}$ along individual growth layers indicating that the stalagmite theoretically grew under equilibrium conditions. There was, however, a strong correlation between width of growth layers and precipitation, as well as a positive correlation between color of layers and annual temperature, where darker layers showed greater $\delta^{13}\text{C}$ and $\delta^{18}\text{O}$ values that correspond to warmer, wetter conditions according to Holmgren et al.'s (1999) interpretation. A 500-yr cool period was recorded between AD 1300 and 1800; the lowest temperatures are at ca. AD 1700. This period overlaps with the "Little Ice Age" experienced in the Northern Hemisphere. Other cool, dry periods occurred from around AD 800 to 900 and AD 440 to 520. The most prolonged warm, wet period took place from AD 40 to 400.

Repinski et al. (1999) also compiled a paleoclimate record for Cold Air Cave using a 300 mm stalagmite (T5) composed entirely of aragonite. U/Th-series dating results showed that the first period of

growth for T5 occurred from ca. 4400 to 4000 BP followed by a 3000-yr hiatus. Growth resumed from 800 to 600 BP. The $\delta^{18}\text{O}$ values ranged from -5.5 to -2.3‰ and the $\delta^{13}\text{C}$ ranged from -6.6 to -1.9‰. The greatest $\delta^{18}\text{O}$ values were found during the older growth period (4400 to 4000 BP).

Brook et al. (1990) determined a record from the Kalahari Desert in northwestern Botswana using a flowstone and column from Drotsky's Cave. Drotsky's Cave developed in dolomite marble and is in an area that receives 400 to 450 mm/yr of rainfall. A 0.5 m core from the column provided dated deposition from ca. 15,000 to 2000 to 3000 BP. The column also yielded two periods of dry, aeolian events indicated by sand blown grains trapped in the carbonate. The earlier event occurred from 14,520 to 5360 BP and the later event was after 5360 BP. Brook et al. (2010) combined the Drotsky Cave records with those from Lobatse II Cave in southeastern Botswana that receives about 550 mm/yr of rainfall. The combined records indicate speleothem deposition at ca. 197,000; 45,000 to 39,000; 32,000; 26,000 to 23,000; 19,400 to 13,000; 6900 to 4000; and 2000 to the present. A dry phase at ca. 1300 BP was indicated by a stalagmite in the southwest entrance of Drotsky's Cave deposited on aeolian sand.

With time, southern African cave studies have become more integrative in their record correlations. For instance, Brook et al. (2010) derived a 35,000-yr paleoclimate record by correlating geochemical and pollen data from a predominantly calcite stalagmite (W-1) in Wonderwerk Cave in the Kalahari region of South Africa. Because W-1 was an extremely large stalagmite, Brook et al. (2010) collected a horizontal core perpendicular to the central growth axis. They determined that pollen data supplemented speleothem data to confirm that greater/lower $\delta^{13}\text{C}$ and $\delta^{18}\text{O}$ values can be interpreted as drier/wetter conditions at Wonderwerk Cave. Radiocarbon ages indicated slow growth periods or hiatuses from ca. 33 to 23,000 and 13,300 to 4000 BP. Three wetter phases were identified from ca. 35 to 33,000, and 23 to 13,300, and 4000 BP to the present. Additionally, Brook et al. (2010) identified three distinct petrographic fabrics to help determine changes in environmental and hydrologic conditions. These fabrics included (1) a layered fabric, which was interpreted to show dry conditions, is formed from a thin film of water that produced regular spelean layers with only a few detritus grains larger than clay particles; (2) a microstromatolitic fabric, which represents modified dry conditions when climate was

relatively drier, or when local air flow conditions promoted higher rates of evaporation; and (3) a concretionary fabric, which records periods of high flow rate and large amounts of detrital deposition. They found that layered and micostromatolitic fabrics were formed during slower growth periods and had greater $\delta^{13}\text{C}$ and $\delta^{18}\text{O}$ values as compared to a concretionary fabric that formed during wetter periods with lower $\delta^{13}\text{C}$ and $\delta^{18}\text{O}$ values. Brook et al. (2010) suggested that greater $\delta^{13}\text{C}$ and $\delta^{18}\text{O}$ values result from C4 vegetation growing above the cave during drier conditions, while lower $\delta^{13}\text{C}$ and $\delta^{18}\text{O}$ values area result from C3 vegetation growing above the cave during wetter conditions.

3.2.2 Hyrax Middens

Hyraxes are herbivores that externally resemble guinea pigs and measure between 30 and 70 cm long. They live in arid regions and have a unique behavior, in that they habitually defecate and urinate in discrete latrine areas over long periods of time (Gil-Romera et al., 2007). With time, these stratigraphically sequenced latrines of thick urine (known as hyraceum) become fossilized hyrax middens that often contain pollen. Additionally, the fossil middens can be analyzed for $\delta^{15}\text{N}$ and $\delta^{13}\text{C}$ as a means to interpret the type of vegetation (C3 or C4) the hyrax were consuming at the time of urination. Researchers using hyrax middens use this relationship between stable isotope ratios and vegetation type to make paleoclimate connections between the amounts of rainfall and subsequently, the amounts of vegetation above a cave system. Paleoclimate records from hyrax middens are the only other “high-resolution” records for Namibia aside from stalagmite DP1.

Gil-Romera et al. (2007) used fossil pollen from 33 samples from six hyrax middens located on the eastern desert edge in the northwestern Kaokoveld of northern Namibia (denoted as the Namib Desert Rock Shelter site in Figure 3.1). Despite not knowing the age range of each hyrax sample, Gil Romera et al. (2007) assumed constant deposition in order to estimate their ^{14}C dates between samples. Combined, this ca. 5200 yr BP continuous record indicates a relative progressive increase in the tree/grass ratio during the last millennium, generally interpreted to mean that the vegetation shifted from a tree and shrub biome to a Nama-Karoo biome, which is dominated by herbs and shrubs. Gil-Romera et al. (2007) identified a hiatus in their pollen record from ca. 4200 to 1690 BP, which they attributed to moisture

declines related to intrinsic savanna dynamics. Difference in the pollen spectra could also have been influenced by poor age constraint of the sample and the stochastic pattern of rainfall in the area.

Chase (2009) studied three middens from the south-facing flank of Kleine Spitzkoppe in western-central Namibia, which borders the hyper-arid Namib Desert. This area receives about 135 mm yr^{-1} of rainfall in which $>70\%$ falls during the winter months (JFM) and is controlled by the ITCZ and ZAB. The $\delta^{15}\text{N}$ values range from 13.4 to 7.4‰ and indicate increased humid conditions from ca. 8700 to 7500, 6900 to 6700, 5600 to 4900, and 4200 to 3500 BP, which was then followed by a more arid phase until ca. 300 yr BP.

Chase et al. (2010) studied southern Africa's Holocene monsoon seasons using a hyrax midden from Austerlitz in northwestern Namibia. This record shows a series of rapid aridification events starting at ca. 3800 cal yr BP along with a progressive decrease in regional humidity throughout the Holocene. Today this location receives about 140 mm yr^{-1} of rainfall, the amount of which is predominantly influenced by the ITCZ and CAB. The record spans between 4825 to 4538 cal yr BP and 1522 to 1385 cal yr BP with a 1 mm isotope sample resolution representing 20 to 35 years of accumulation. Chase et al. (2010) argued that when combined with isotope records from Cold Air Cave, South Africa (Holmgren et al., 1999) and sea surface temperature (SST) records from marine core MD79257 from the SW Indian Ocean (Bard et al., 1997; Sonzogni et al., 1998; Chase et al., 2010), their data show a progressive Holocene aridification. This climate response seems to correlate with Northern Hemisphere patterns, instead of following anti-phase Southern Hemispheric patterns, which is what most climate modelers would expect. In addition to records existing in lower resolutions and/or with different patterns, Chase et al. (2010) noted that little data is available in Southern Hemispheric regions to make complete interpretations. However, they conclude that correlations can be made between marine and terrestrial records that link the Benguela upwelling system and regional climates. Specifically, they asserted that the Austerlitz midden has similarities to Cold Air Cave, Angola, the Congo Basin, and the Northern Hemisphere tropics. They attribute aridification to be caused by solar and Earth's geomagnetic forcings.

3.2.3 Dune Sediments

In southern Africa, dating sand dune activation using optically stimulated luminescence (OSL) has been a method of identifying variations in sediment supply, wind strength, and vegetation. These proxies are traditionally interpreted to be indicators of aridity and precipitation, but there may be a need for reevaluation of this technique as more reliable age dates become available (Chase, 2009). As of 2009, 219 luminescence ages had been published for the linear dune fields of the Kalahari Desert; 78 from the northern Kalahari and 141 from the southwestern Kalahari. Chase (2009) reviewed and synthesized these records to determine that three major phases of dune development took place from ca. 60 to 40, 30 to 25, and 17 to 4 ka BP, which are inconsistent with both glacial and interglacial phases of dune development. Chase suggests that the records do not correspond with the cold/dry (glacial) and warm/wet (interglacial) for southern Africa. The northern Kalahari records show increased humidity from ca. 43 to 36, 35 to 26, 22 to 10, and 6 to 1 ka, while southern Kalahari records indicated increased humidity from ca. 37 to 17 and 12 to 6 ka with potentially drier phases from ca. 10 to 9 and 4 to 2 ka.

Brook et al. (2007) conducted sediment and dating analyses of relict Holocene shorelines on the western boundary of Etosha Pan in Namibia. These shorelines were once arcuate, or possibly, clay lunette dunes. Brook et al. (2007) collected several auger sediment samples about 100 m north of the Okondeka waterhole for grain size analysis. Additionally, they collected bucket sand auger samples for OSL dating of three prominent shoreline flats. Sediment samples contained high U/Th ratios because of wind blown clays and salts incorporated into the dune sediments. This causes disequilibrium in the ^{238}Th decay chain, which resulted in U/Th-series dates to have uncertainties between 16 and 48% for the. This uncertainty only impacts about 25% of the decay chain, and given this premise, U/Th dates were considered to still be good estimates of the ages of the shorelines at Etosha Pan, which ranged from 6400 to 2100 BP. Brook et al. (2007) compared the Etosha paleo-shoreline dates to other Holocene records from the region. Some of these record results are as follows: pollen in sediments at Lake Otjikoto indicates relatively dry conditions after 4000 cal yr BP, wetter conditions before 1000 cal yr BP, and drier conditions through to the present (Scott et al., 1991); pollen from fossil hyrax dung in the Huab River valley in northwest Namibia show a

slight increase in moisture availability from 6000 to 1000 BP, which was followed by arid conditions after 1000 BP (Gil-Romero et al., 2006); increased flow is recorded by higher lake levels at Lake Ngami in Botswana after 8000 BP, after 6800 BP, from 4600 to 3500 BP, and at 1700 BP (Brook et al., 2007); younger terraces in the Nadas, Hoarusib, and Hoanib valleys in the northern Namib desert indicate increased river flow from 4500 to 1200 BP; increased silt deposits at Homeb in the Kuiseb valley suggest wetter phases from ca. 6800 to 4800 BP; and fluvial sediments at the end of the Tsauchab River indicate wetter periods at ca. 9000, 900, and 300 BP (Brook et al., 2006). Wetter conditions at Etosha Pan were at 6400 and 2100 BP.

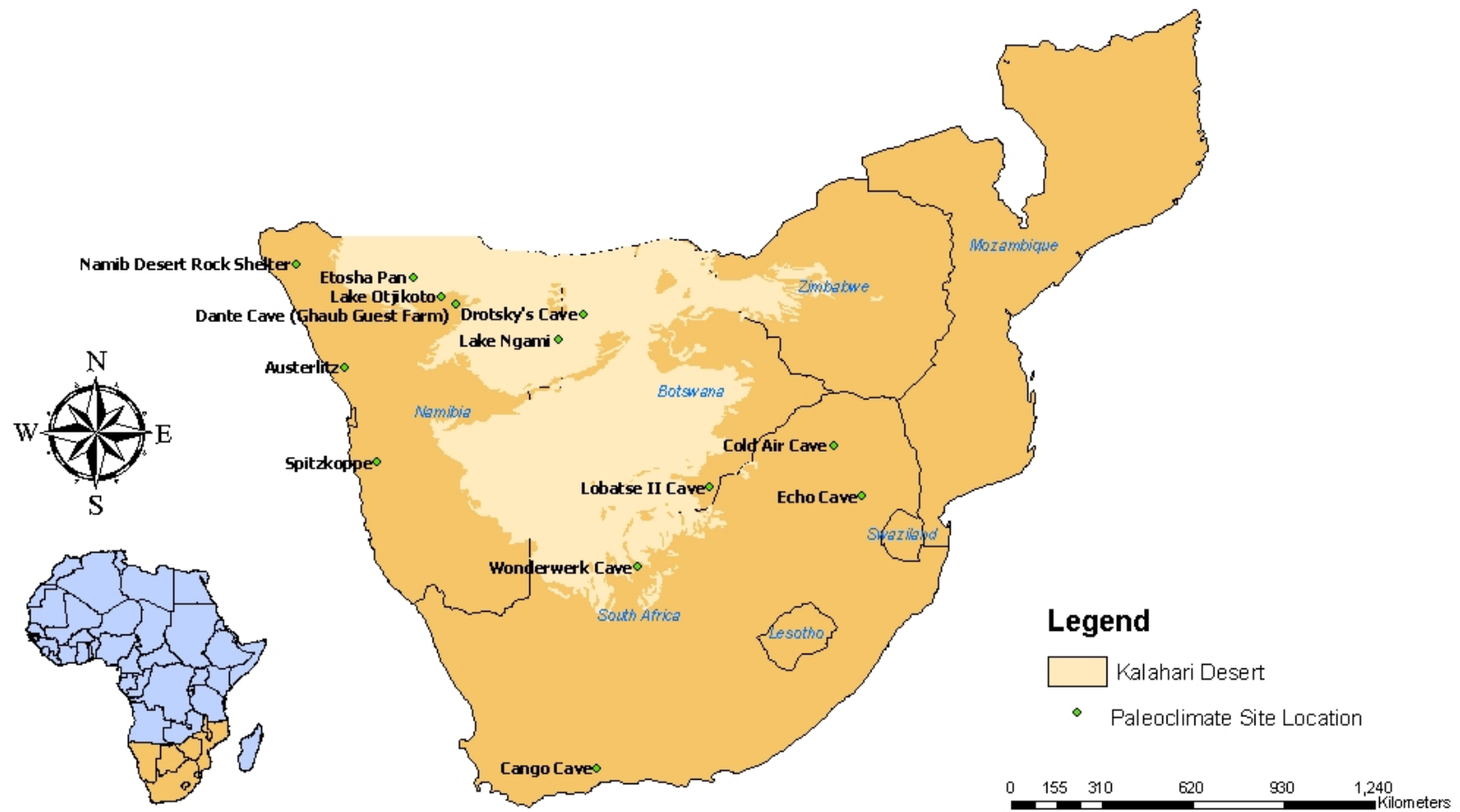


Figure 3.1. Site locations of southern African paleoclimate studies discussed in Chapter 3.

CHAPTER 4

METHODS

4.1 General Description and Sampling

DP1 measures about 150 cm in length along the center growth axis and varies in width from 8 cm at its base to 21 cm at its widest point (Figure 4.1). For easier descriptions, DP1 was divided into two segments (A and B) as further discussed in Section 5.3.1. DP1 was cut lengthwise using a diamond tipped circular blade saw. Half of the stalagmite was in the possession of The University of Georgia (UGA) Speleothem Laboratory and available for analysis, hereafter described as DP1. Staff at the Keystone Granite Company in Elberton, Georgia cut off the outer flank of the upper 70 cm of DP1 so that it had a flat working surface (Figure 4.2.a,b). At the UGA Speleothem Lab, Sletten then cut DP1 along its central axis (Figure 4.2.c), where one quadrant was further cut into 28 chips for thin sections (Figure 4.2.d), and the other quadrant was retained for powder samples. All powder samples were collected using a dental drill and an HP-4 gauge bur (Figure 4.2.e).

4.2 Age Dating and Growth Rate

In 2007 Ben Hardt, who collected DP1 in 2006 from Dante Cave in Namibia in collaboration with Eugene Marais, drilled 11 powder samples offset from the center growth axis for U-series dating, which when analyzed, captured a total record of about 4600 years BP. In March 2009, Sletten collected an additional 15 powder samples. Samples were drilled from calcite and aragonite layers that appeared to be free of detritus. Detritus contains a higher concentration of ^{230}Th that is not derived from the co-precipitated ^{234}U from calcite or aragonite deposition, and in turn, accelerates the radiometric clock resulting in inaccurate dates (Ford, 1997). Additionally, Sletten collected samples from layers to fill in gaps from Hardt's sequence of dates to obtain a greater resolution in age.

Sletten's samples were drilled, weighed to approximately 0.15 g, and transferred on weighing paper to borosilicate glass vials. Samples were shipped to the Stable Isotope Laboratory at the University of Minnesota, USA for dating analysis using inductively-coupled plasma mass spectrometry (ICP-MS) on a Finnigan-MAT Element. The chemical procedure used to separate U and Th is similar to that described in Shen et al. (2002). Decay constants used for ^{230}Th , ^{234}U , and ^{238}U were $9.1577 \times 10^{-6} \text{ yr}^{-1}$, $2.8263 \times 10^{-6} \text{ yr}^{-1}$, and $1.55125 \times 10^{-10} \text{ yr}^{-1}$, respectively (Cheng et al., 2000). Corrected ^{230}Th ages assume the initial $^{230}\text{Th}/^{232}\text{Th}$ atomic ratio of $4.4 \pm 2.2 \times 10^{-6}$. This is a ratio for a "bulk earth" or crustal material at secular equilibrium, with a $^{232}\text{Th}/^{238}\text{U}$ value of 3.8. The error of this "bulk earth" value is assumed to be $\pm 50\%$. The error in the final "corrected age" incorporates this uncertainty. Linear interpolation between dated intervals was used for calculating age dates for each isotope sample. Reported dates have been adjusted such that BP stands for "Before Present", where the "Present" is defined as the year AD 1950. Growth rates were determined by dividing differences in depth for U/Th dated intervals by differences in U/Th dates shown in the following equation (Eq [1]):

$$\frac{(\text{Depth Below Sample} - \text{Depth of Sample})}{(\text{Age of Depth Below Sample} - \text{Age of Depth Above of Sample})} \quad [1]$$

4.3 C and O Stable Isotope Analysis

In 2007, Hardt drilled 40 powder samples for C and O stable isotope analysis from the first 22.5 cm. Of these 40 samples, four were not analyzed. His work was conducted at the University of Minnesota Stable Isotope Laboratory using a Finnegan MAT 252 isotope ratio mass spectrometer equipped with a Kiel carbonate device.

In 2010, Sletten hand drilled and sampled approximately 0.05 g of powder for 251 samples for C and O stable isotope analysis. Of these, 168 samples were analyzed at the UGA Stable Isotope Laboratory. Samples were reacted under vacuum with distilled 100% orthophosphoric acid (H_3PO_4) at 50°C following McCrea (1950) and Al-Aasm et al. (1990) (Figure 4.2.e,f). CO_2 was collected by

conventional cryogenic methods and analyzed on a Finnegan Delta E gas source ratio mass spectrometer at the UGA Stable Isotope Laboratory. All isotope ratios are reported in per mil (‰) relative to Vienna Pee Dee Belemnite (VPDB). Laboratory standards were prepared for each set of about 10 samples and have been calibrated to NBS-19 ($\delta^{13}\text{C} = +1.95\text{‰}$, $\delta^{18}\text{O} = -2.2\text{‰}$ relative to VPDB) and NBS-18 ($\delta^{13}\text{C} = -5.0\text{‰}$, $\delta^{18}\text{O} = -23\text{‰}$ relative to VPDB). The 2σ error of the combined extraction and analysis is 0.04‰ for $\delta^{13}\text{C}$ and 0.05‰ for $\delta^{18}\text{O}$.

The remaining 83 isotope samples were analyzed at the University of Alabama Stable Isotope Laboratory using a GasBench-IRMS system by implementing methods similar to those described by Debajyoti and Skrzpek (2007). Isotope values relative to VPDB were standardized to the NBS-19 standard. Correction to all measured ^{18}O compositions were made to account for reaction temperature 50°C . Reproducibility (2σ) for $\delta^{13}\text{C}$ was calculated to be $\pm 0.16\text{‰}$ and $\pm 0.3\text{‰}$ for $\delta^{18}\text{O}$.

For all aragonite isotopic values reported in conjunction with a time series, 1.7‰ was subtracted from $\delta^{13}\text{C}$ for aragonite (Romanek et al., 1992) and 0.8‰ from $\delta^{18}\text{O}$ (Kim et al., 2007). The transformed aragonite values account for aragonite's inherent fractionation of heavier isotopes in comparison to calcite and removes the mineralogical bias when reporting stable isotope data in a time series. The aragonite transformation thus reports all isotopic data in relation to calcite. For the fabric analysis, raw isotopic values were used in order to preserve the original data and to better distinguish differences between fabrics, particularly within the aragonite fabrics.

4.4 Mineralogy and Luminescence

Using a Bruker D8 X-ray Diffractometer at the Department of Geology at UGA, X-ray diffraction (XRD) was used to differentiate between calcite and aragonite layers for 156 of 287 isotope samples (Figure 4.2.h). Samples were scanned from 20 to 65° 2θ using $\text{Co}_{K\alpha}$ radiation with 10 deg/min scan rates. Thin section analysis was conducted to interpret the mineralogy of layers between isotope samples resulting in mineralogical identification of 257 of 287 isotopic samples. The remaining 30 samples did not have accompanying thin sections for mineral identification, but XRD results from samples within those intervals indicated consistent mineralogy. Visual Luminescent Analysis (Shopov, 1997) was used to

excite stalagmite fluorescence. Visual observations of relative variations in fluorescence were made to distinguish relative shifts in the amount of organic content between layers. This method was a cross-referencing tool for differentiation between layers and was not a quantitative method of luminescence activators. In general, layers of brighter luminescence indicate greater amounts of humic and/or fulvic acids associated with plant material that is then preserved in the spelean CaCO_3 (Baker et al., 1998).

4.5 Petrography

A total of 25 large (50 mm x 75 mm) thin sections designated DP1-1 to DP1-28 were prepared by Quality Thin Sections in Tucson, Arizona. Table 4.1 shows the depths covered by each thin section. Thin section chips DP1-5 and DP1-25 were not made into thin section because an inadequate amount of material was cut for a full thin section. DP1-23 was not made into a thin section because it was originally thought to contain analogous layers with little petrographic significance. Thin sections were analyzed under transmitted and polarized light using a Leica DM EP and a Leitz Lab 12 Pol S petrographic microscope at UGA to identify structural and crystal growth variations between layers, fabrics, and mineralogy.

4.5.1 Fabric Analysis

Initial assessment of the thin sections revealed that there was a variety of fabrics recorded in DP1. In particular, layers of aragonite showed sequential patterns of widening crystals during periods of relatively high aridity noted by the isotopic results. This relationship gave further cause to investigate whether or not variations in spelean fabrics correlated with greater $\delta^{13}\text{C}$ and $\delta^{18}\text{O}$ values. To conduct this study, a fabric classification system was developed that includes one calcite and five aragonite fabric classifications based on crystal orientation, nucleation, width, and/or morphology, which are summarized in Table 4.2. The fabrics are as follows: columnar calcite (CC), coarse aragonite (CA), needle aragonite (NA), massive needle aragonite (MNA), massive botryoidal needle aragonite (MBNA), and interwoven aragonite (IA).

To correlate fabrics to isotopic values, a fabric classification was designated for 243 of the 287 intervals with isotopic data. The remaining 44 intervals at depths of 190 to 202 mm, 1212 to 1299 mm,

and 1354 to 1401 mm did not have an accompanying thin section for reasons stated in Section 4.4, and so, were not included in the analysis. This process required very precise measurement of intervals both on the DP1 body and in thin section. All fabric identifications were made using one width of scope view (4.8 mm or 2.0 mm) along the central growth axis such that fabric identifications correlated best with XRD and isotopic results. Linear regression was used to determine the amount of variation explained between the $\delta^{13}\text{C}$ and $\delta^{18}\text{O}$ values for the different fabric classifications.

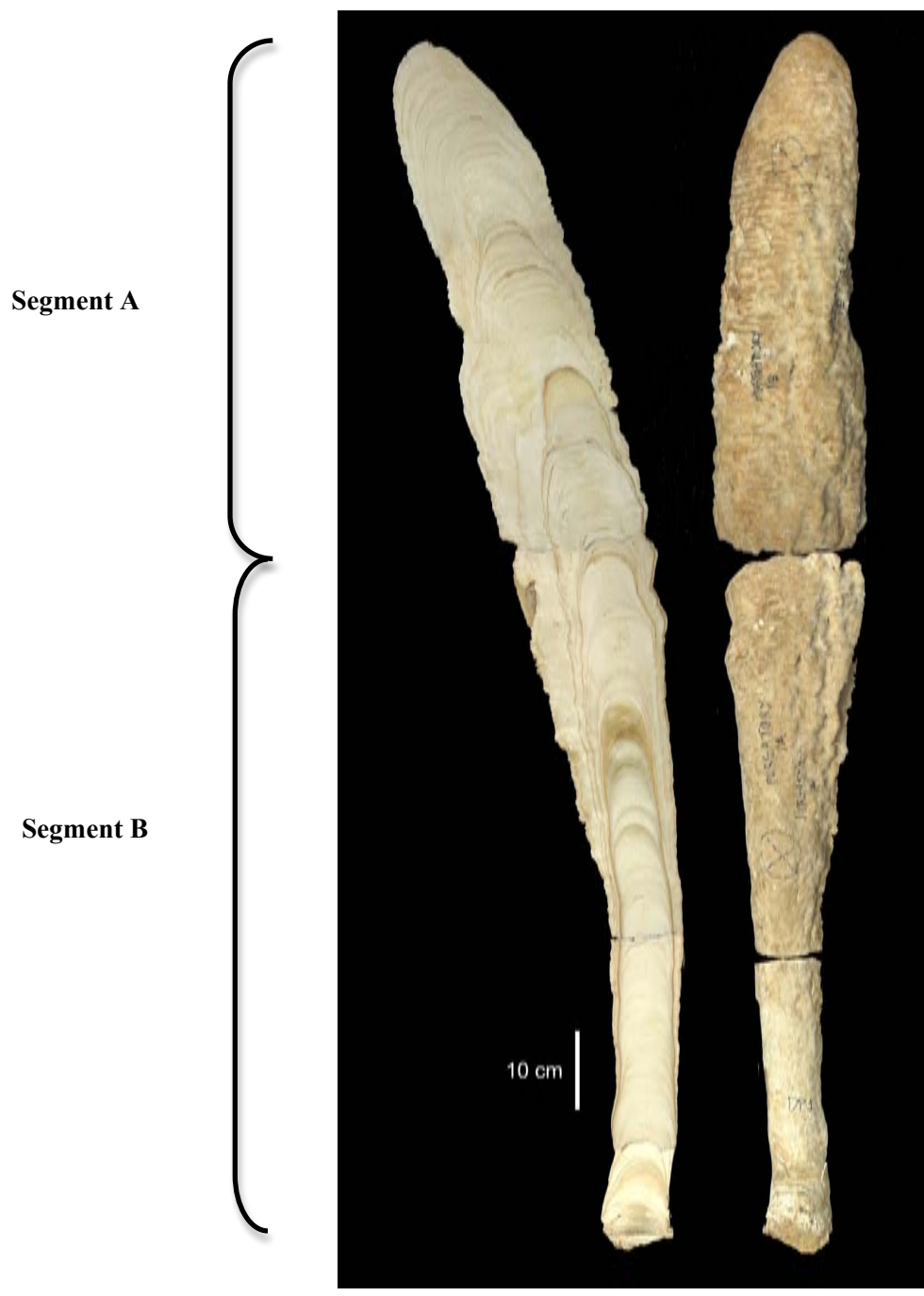


Figure 4.1 Stalagmite DP1 from Dante Cave in northeast Namibia.

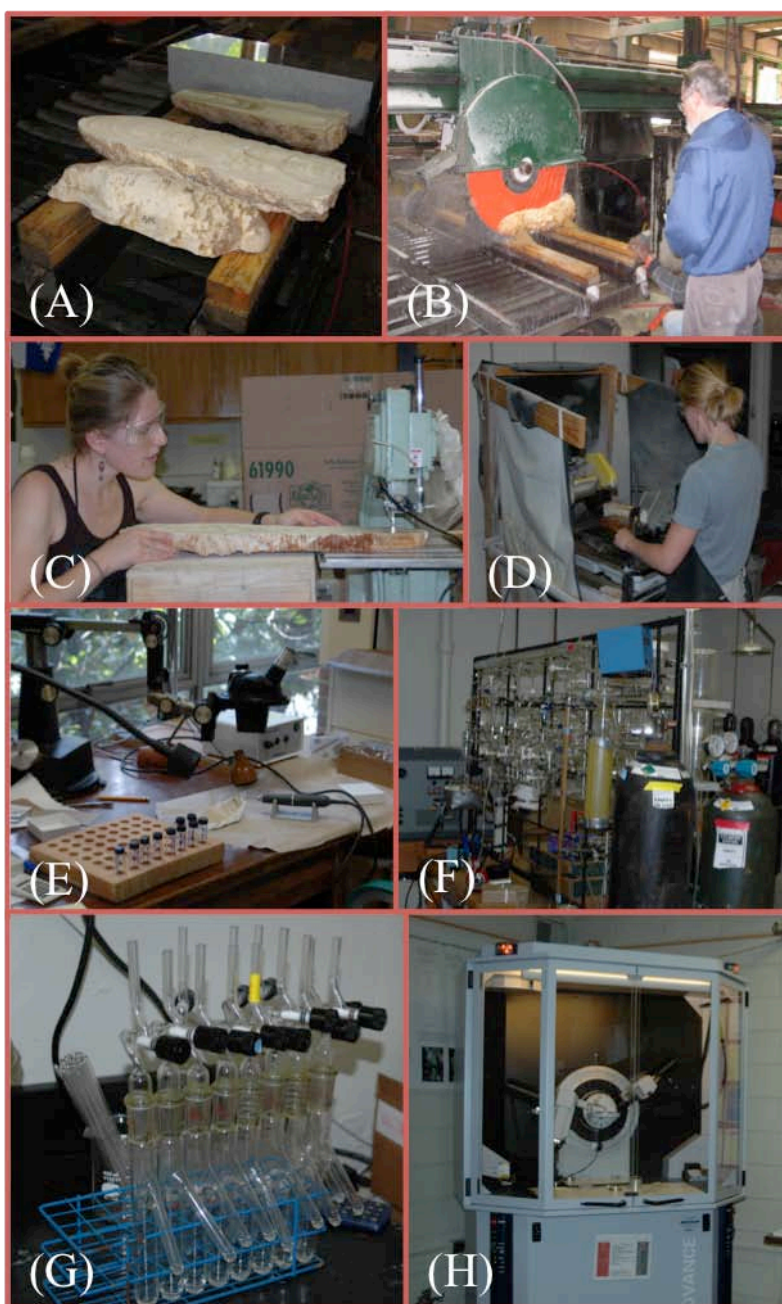
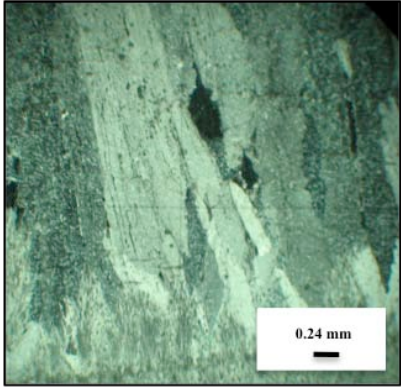
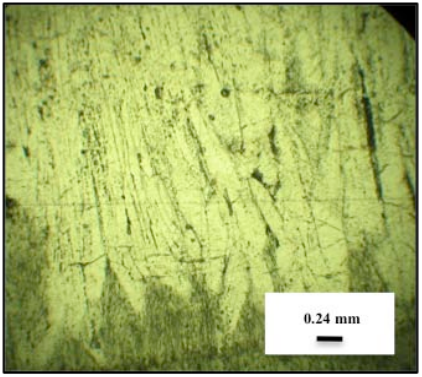
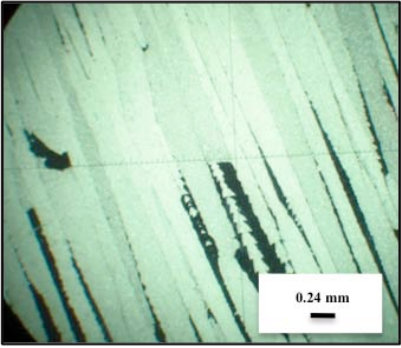
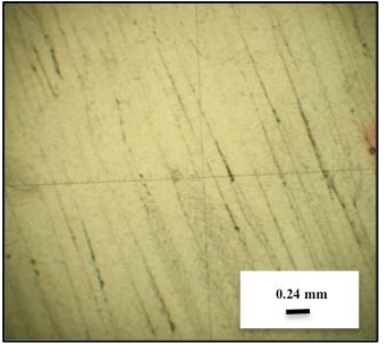
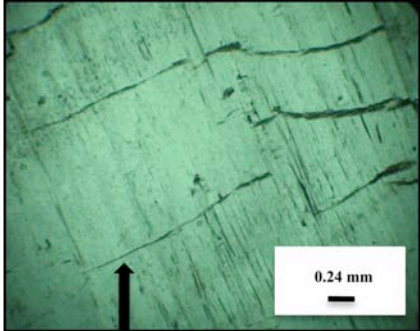
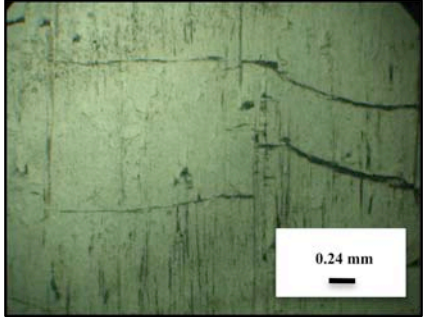
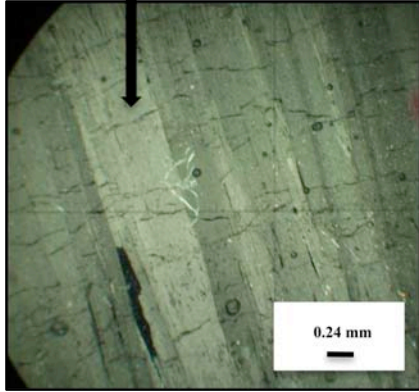
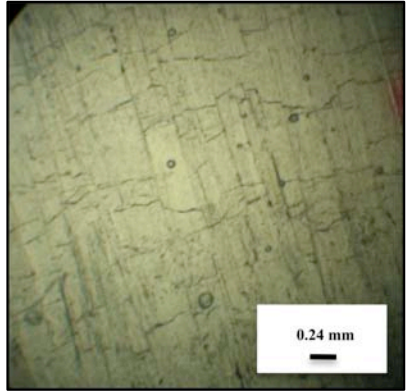


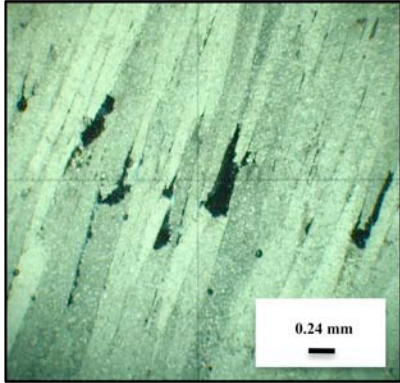
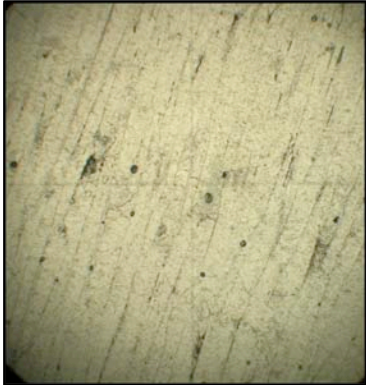
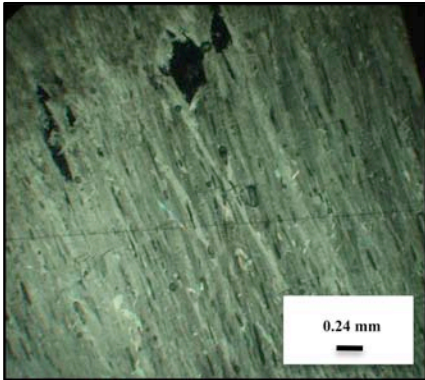
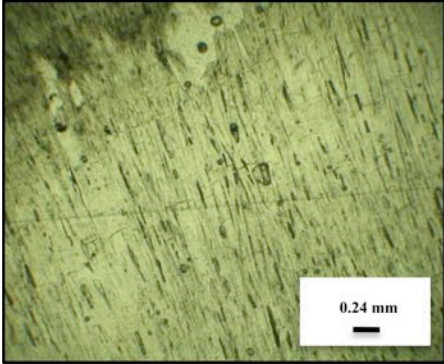
Figure 4.2. Photographs of analytical methods: (a) Stalagmite DP1 before being cut into slabs at the Keystone Granite Company, Elberton, Georgia; (b) Bruce Railsback observing the top half of DP1 being cut into a slab using a large diamond tip blade saw; (c) Hillary Sletten cutting the top half of DP1 along the center axis using a smaller diamond tipped blade saw at the UGA Sedimentology Petrology and Geochemistry Lab; (d) Hillary Sletten cutting DP1 thin section chips in the Rock Saw Lab at UGA; (e) Dental drill set-up for powder sampling; (f) UGA Stable Isotope Lab vacuum extraction line; (g) Phosphoric acid reaction vessels for isotope analysis; (h) Bruker D8 X-ray Diffractometer at the Department of Geology at UGA.

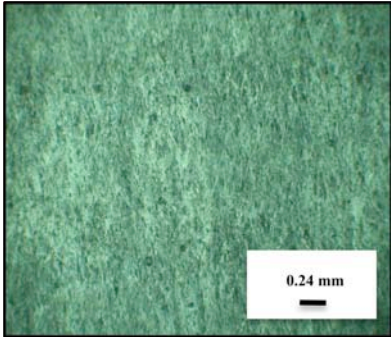
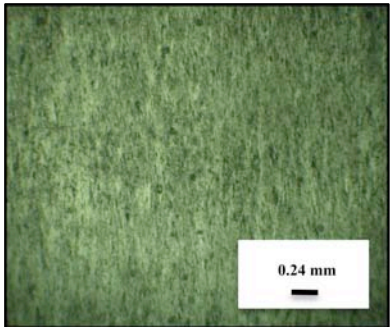
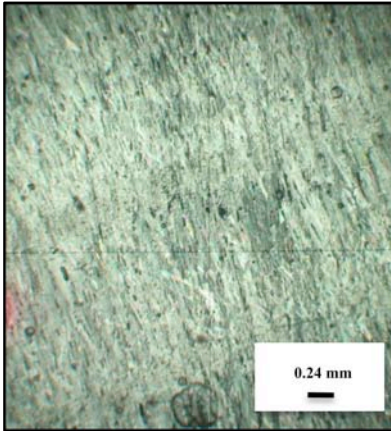
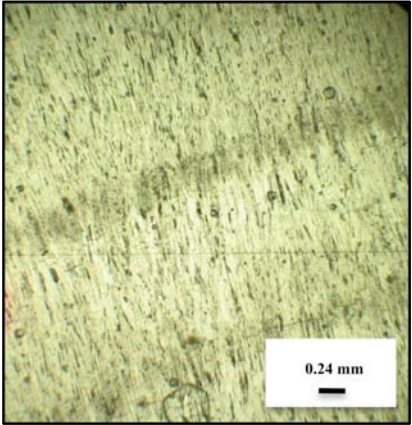
Table 4.1 Start and end depths for DP1 thin sections.

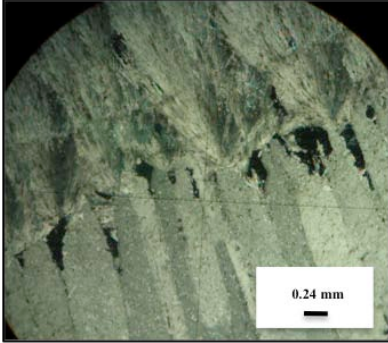
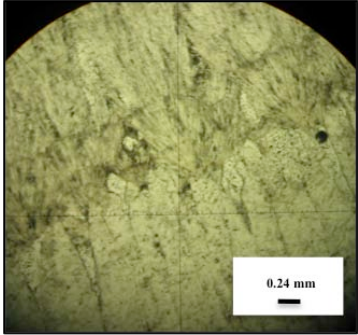
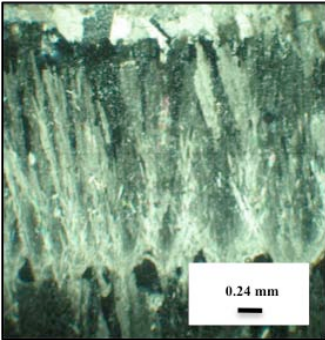
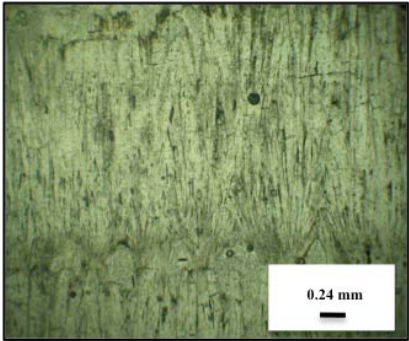
Thin Section ID	Start Depth from Top of DP1 (mm)	End Depth from Top of DP1 (mm)
DP1-1	0	64
DP1-2	64	102
DP1-3	110	150
DP1-4	151	190
DP1-5	190	202
DP1-6	203	246
DP1-7	252	315
DP1-8	318	381
DP1-9	382	441
DP1-10	442	501
DP1-11	504	568
DP1-12	570	612
DP1-13	613	676
DP1-14	682	721
DP1-15	724	788
DP1-16	790	829
DP1-17	833	897
DP1-18	898	961
DP1-19	962	1025
DP1-20	1035	1099
DP1-21	1100	1163
DP1-22	1164	1212
DP1-23	1212	1299
DP1-24	1299	1354
DP1-25	1354	1401
DP1-26	1402	1457
DP1-27	1466	1523
DP1-28	1524	1584

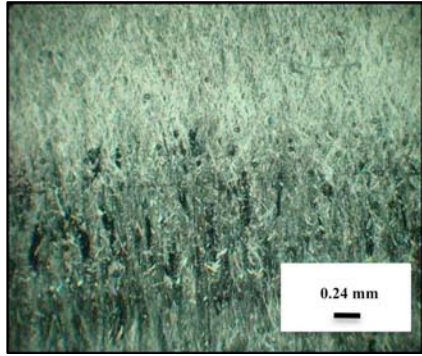
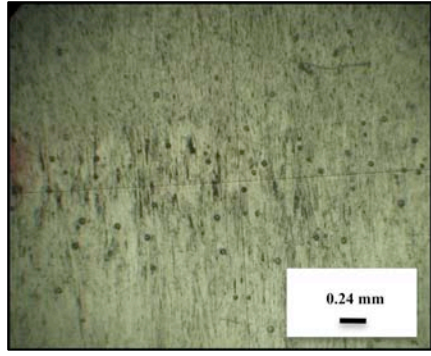
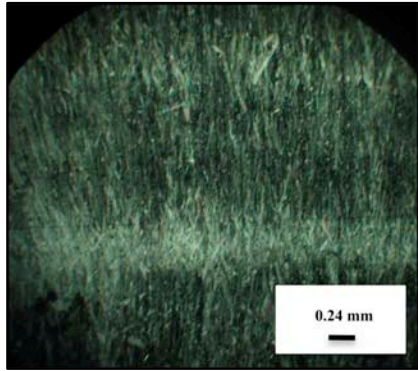
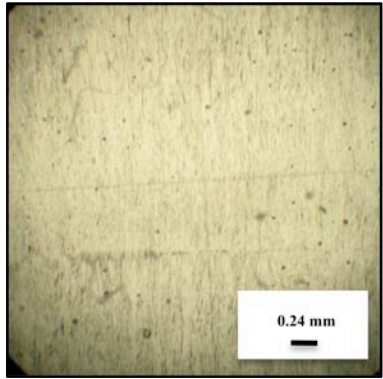
Fabric	Table 4.2.a Fabric Classification Descriptions		Depth (mm)	Examples of Variations in Fabrics	
				Polarized	Transmitted
Columnar Calcite (CC)	Crystal Orientation and Nucleation	<ul style="list-style-type: none"> * Bladed crystals vertically oriented or slightly angled to about 30° along the c-axis * CC crystals nucleate on all other fabrics except for CA 	69		
	Crystal Dimensions and Morphology	<ul style="list-style-type: none"> * Crystal widths have a 4:1 ratio or greater * More arid conditions or space for degassing to take place promote jagged intercrystalline boundaries 	394		

Fabric	Table 4.2.b Fabric Classification Descriptions		Depth (mm)	Examples of Variations in Fabrics	
				Polarized	Transmitted
Coarse Aragonite (CA)	Crystal Orientation and Nucleation	<p>* Crystals are vertically oriented along the c-axis; parallel growth</p> <p>* CA crystals typically nucleate from increasing widths of NA crystals</p>	906		
	Crystal Dimensions and Morphology	<p>* Crystal widths range from 0.05-0.5 mm</p> <p>* Broad, planar crystals with defined cleavage planes</p>	972		

Fabric	Table 4.2.c Fabric Classification Descriptions		Depth (mm)	Examples of Variations in Fabrics	
				Polarized	Transmitted
Needle Aragonite (NA)	Crystal Orientation and Nucleation	* Crystals are vertically oriented along the c-axis; parallel growth * NA crystals nucleate on all other fabric types	252		
	Crystal Dimensions and Morphology	* Crystal widths range from 0.02-0.2 mm	756		

Fabric	Table 4.2.d Fabric Classification Descriptions		Depth (mm)	Examples of Variations in Fabrics	
				Polarized	Transmitted
Massive Needle Aragonite (MNA)	Crystal Orientation and Nucleation	<p>* Crystal orientation is often non-distinct with no clear intercrystalline boundaries; some sub-parallel orientation</p> <p>* MNA crystals nucleate on all other fabric types</p>	263		
	Crystal Dimensions and Morphology	<p>* Crystal widths average ≤ 0.02 mm</p>	586		

Fabric	Table 4.2.e Fabric Classification Descriptions		Depth (mm)	Examples of Variations in Fabrics	
				Polarized	Transmitted
Massive Botryoidal Needle Aragonite (MBNA)	Crystal Orientation and Nucleation	<p>* Crystals generally oriented vertically along c-axis</p> <p>* MBNA crystals nucleate form a single point, often on euhedral crystal boundaries.</p> <p>* Some MBNA layers form on planar/truncated crystal boundaries.</p>	146		
	Crystal Dimensions and Morphology	<p>* Crystal widths average ≤ 0.02 mm</p>	275		

Fabric	Table 4.2.f Fabric Classification Descriptions		Depth (mm)	Examples of Variations in Fabrics	
				Polarized	Transmitted
Interwoven Aragonite (IA)	Crystal Orientation and Nucleation	<ul style="list-style-type: none"> * Majority of crystals overlap at about 45° * Crystals vary from no space between crystals to about 0.15 mm spacing * IA crystals nucleate on all other fabric types 	778		
	Crystal Dimensions and Morphology	<ul style="list-style-type: none"> * Crystal widths range from $\leq 0.02-0.15$ mm 	877		

CHAPTER 5

RESULTS

5.1 Age Model

A chronology was created using 22 of the 26 powder samples for time series dating. Three of the samples (DP1-450, -654, and -705) produced age results that were out of sequence in the time series and were removed from the analysis (Table 5.1). Samples DP1-450 and DP1-705 both contained detritus in the powder, and DP1-654 had an unusual U content, possibly caused by diagenesis. For the final calculated dates, the 22 viable results had error estimates of 2% or less with the exception of DP1-315 and DP1-250 that had error estimates of 5%, and DP1-103 that had an error estimate of 3%. This is caused by a higher inaccuracy in U/Th dating of younger materials that have had little time to decay (Railsback et al., 2011; van Beynen et al., 2008). Accordingly, age data indicate that DP1 was deposited between ca. 4600 and 14 BP, but not at a continuous growth rate (Figure 5.1). Growth rates vary from 21.0 mm/yr to 1.2 mm/yr⁴, with 21.0 mm/yr being a rate calculated for one year between two U/Th dates (DP1-671 and -690). The overall average growth rate for DP1 was 0.35 mm/yr.

5.2 Stable Isotope Data

Values of $\delta^{13}\text{C}$ in the 287 samples from stalagmite DP1 range from -4.7 to -11.0‰ VPDB (Appendix A). Values for corrected² aragonite range from -4.7 to -11.0‰ VPDB and in calcite they range from -10.4 to -7.2 ‰ VPDB. Values of $\delta^{18}\text{O}$ in the 287 samples from stalagmite DP1 range from -6.6 to -11.6‰ VPDB. Values for aragonite range from -11.4 to -6.6‰ VPDB and in calcite they range from -11.6 to -8.4‰ VPDB. When comparing the isotopic variations in both aragonite and calcite, there are three periods where 10 or more consecutive $\delta^{13}\text{C}$ and $\delta^{18}\text{O}$ values are greater than the mean value of -9.5‰ and -8.1‰

² For all aragonite isotopic values reported in conjunction with a time series, $\delta^{13}\text{C}$ for aragonite was corrected +1.7‰ (Romanek et al., 1992) and $\delta^{18}\text{O}$ +0.8‰ (Kim and O'Neil, 2007) to account for aragonite's inherent fractionation of heavier isotopes in comparison to calcite.

VPDB, respectively. These greater values were recorded from 3126 to 2059 BP, 1113 to 800 BP, and 586 to 364 BP.

5.3 Petrographic and Fabric Analysis

5.3.1 Variation Among Layers

Petrographic observation of annual layers, confirmed with XRD analysis, shows layers to be composed of primary aragonite and calcite with no re-crystallization along the central growth axis. The top 690 mm of DP1 consists of alternating layers of aragonite and calcite (Appendix A), herein referred to as Segment A. Aragonite layers range from 0.25 to 2 mm thick, and calcite layers range from 8 to 38 mm thick. Segment A is also non-symmetrical on both sides of the growth axis. On the left side, DP1 thickens to a maximum of 13.5 mm from the axis in Segment A, whereas on the right side, it thickens to 7 mm at the same depth.

In comparison, the bottom half of DP1, herein referred to as Segment B, extends from 690 mm to the bottom and is composed of aragonite layers with an average thickness of 2 mm. In general, widths on the left side of the axis are double the width of that on the right until about 1051 mm from the top, where each side has about equal widths to the base of DP1.

5.3.2 Layers with Dissolution and Aridification Features

DP1 dissolution features include cavities and layers of detritus between layer boundaries. All cavity features are in Segment A (77 mm, 113 mm, 474 mm, 493 mm, 557 mm, 520 mm, and 610 mm) with none present in Segment B. Figure 5.2.a shows varying sizes and pathways of cavity dissolution between two layers of massive needle aragonite (MNA) at 113 mm. This suggests that porous layers above later allowed water to enter DP1 and dissolve along boundary layers, making the cavities secondary features related to later events than what was originally recorded at that layer depth. Petrographic relationships for the other six dissolution features provide less evidence about whether dissolution happened prior to deposition of the material immediately above or later in the stalagmite's history.

Layers of detritus are present at 55 mm, 75 mm, 284 mm, and 685 mm in Segment A, and at 748 mm, 743 mm, 801 mm, 1111 mm, 1136 mm, and 1482 mm in Segment B. Figure 5.2.b at 250 mm from

the top of DP1 shows where MNA nucleates on a layer of detritus above evenly truncated needle aragonite (NA) at or near the growth axis. The layer of detritus would likely be deposited by an increased amount of groundwater flowing over DP1 and later coating it with a layer of mud, potentially causing crystal truncation. This combination of layers captures a wet, erosional phase between two drier periods of deposition. Moving along the same layer at 250 mm toward the flank of DP1, the nucleation shifts to MBNA above a thinned detritus layer that coated the NA, indicating a less wet environment or nucleation surface, more degassing signified by smaller crystal size, and a shift in the fabric (Figure 5.2.c).

Evidence of more extensive drying surfaces occurs at 86 mm (Figure 5.2.d) and 275 mm. At 85 mm MBNA was precipitated on columnar calcite (CC). Below this boundary at ~86 mm, CC forms a surface layer with smooth intercrystalline boundary layers (Figure 5.2.e), suggesting uninterrupted growth. At the 84 mm surface layer boundary, the CC intercrystalline boundary layers become jagged and separated from which MBNA forms. This may suggest CC growth was interrupted or reduced as evaporative conditions in the cave increased. Using the transformed aragonite values to compare the MBNA layer to the CC layer shows that the isotope values are greater in the MBNA than the CC. $\delta^{13}\text{C}$ shifts from -10.9 to -9.1‰ VPDB for MBNA to CC layers, respectively, and $\delta^{18}\text{O}$ shifts from -11.4 to -10.6‰ VPDB for MBNA to CC layers, respectively.

A similar case where crystals progress from smooth intercrystalline boundaries to jagged ones within a layer is seen at 241 mm (Figure 5.2.f). Here, MNA precipitated on NA and became separated and jagged at the boundary, perhaps indicating another drying phase. In some cases, as with the example at ~86 mm, these petrographic observations of crystal growth switching from uninterrupted growth to interrupted growth show correlation with isotopic values that shift from lower to greater values between the fabrics, which supports a relative environmental change from wetter to drier conditions inside Dante Cave.

5.3.3 Correlation of Fabrics with $\delta^{13}\text{C}$ and $\delta^{18}\text{O}$ Values

Variations between derived fabric classifications show a direct relationship to enrichment in ^{13}C and ^{18}O with $\delta^{13}\text{C}$ values ranging from -10.4 to -3.0‰ VPDB and $\delta^{18}\text{O}$ values ranging from -11.6 to -5.8‰ VPDB

(Figure 5.3). The R^2 value for the entire dataset of $\delta^{13}\text{C}$ and $\delta^{18}\text{O}$ is 0.64, indicating a significant amount of variation in $\delta^{13}\text{C}$ is explained by the variation in $\delta^{18}\text{O}$. When plotted, fabrics group by their isotopic range and have varying R^2 values from the R^2 value of the overall dataset. Only one fabric classification was found for calcite, columnar calcite (CC), which has a 4:1 or greater length-to-width ratio. CC formed on all fabric surfaces except for coarse aragonite (CA). Calcite fabrics ($R^2 = 0.26$) have isotope values that range from -10.4 to -7.2‰ VPDB for $\delta^{13}\text{C}$ and -11.66 to -8.4‰ VPDB for $\delta^{18}\text{O}$.

Aragonite fabrics group according to their ^{13}C concentrations, which are reflected in changes in crystal width (Figure 5.3). As $\delta^{13}\text{C}$ values increased, crystal widths measured within the different fabrics also increased. The fabric with the most variation explained by ^{13}C concentrations is massive botryoidal needle aragonite (MBNA) ($R^2 = 0.83$). It has an average crystal width of ≤ 0.02 mm and nucleates on all other types of fabrics where individual botryoids radiate from a central point of nucleation. MBNA has isotope values that range from -9.3 to -5.4‰ VPDB for $\delta^{13}\text{C}$ and -11.6 to -8.4‰ VPDB for $\delta^{18}\text{O}$.

Interwoven aragonite (IA) ($R^2 = 0.34$) crystal widths range ≤ 0.02 to 0.15 mm and has some variation of interwoven crystals at approximately 45° . Individual crystals widen, but the overall fabrics become denser. IA has isotope values that range from -8.8 to -4.5‰ VPDB for $\delta^{13}\text{C}$ and -9.9 to -7.17‰ VPDB for $\delta^{18}\text{O}$. Massive needle aragonite (MNA) ($R^2 = 0.27$) crystal widths average ≤ 0.02 mm; however, MNA orientation is often indistinguishable with a petrographic microscope because the crystals are so densely formed that intercrystalline boundaries are not visible. MNA has isotope values that range from -8.2 to -5.3‰ VPDB for $\delta^{13}\text{C}$ and -10.5 to -7.2‰ VPDB for $\delta^{18}\text{O}$. Both IA and MNA nucleate on all other types of fabric surfaces.

Needle aragonite (NA) ($R^2 = 0.45$) crystal widths range from 0.02 to 0.2 mm; crystals are oriented along the c-axis. NA nucleates on all types of fabrics and is the fabric that most commonly transitions into CA. NA has isotope values that range from -8.3 to -4.3‰ VPDB for $\delta^{13}\text{C}$ and -9.7 to -5.8‰ VPDB for $\delta^{18}\text{O}$. CA ($R^2 = 0.06$) has the least amount of variation explained by ^{13}C concentrations; however, it is the fabric with widest crystals, which range from 0.05 to 0.5 mm. CA has isotope values that range from -4.7 to -3.0‰ VPDB for $\delta^{13}\text{C}$ and -8.1 to -6.1‰ VPDB for $\delta^{18}\text{O}$.

Enrichment of ^{13}C was observed to change with progressive widening of crystal dimensions and associated fabrics from 1075 to 1066 mm, 1005 to 977 mm and 263 to 278 mm. The progression from 1005 to 977 mm is shown in Figure 5.4 where crystal widths widen continuously from 0.02 to 0.15 mm at 1005 mm in the IA layer to 0.1 to 0.3 mm at 977 mm in the CA layer.

5.4 Dry and Wet Periods

Combined isotopic and mineralogical results indicate that there are three periods of slow growth or hiatuses, which are designated as slow growth intervals (Sn) (Figure 5.5). The depths, ages, and growth rates of these periods are summarized in Table 5.2. The Sn intervals are marked by the three periods where 10 or more consecutive $\delta^{13}\text{C}$ and $\delta^{18}\text{O}$ values are higher than the mean value of -8.1‰ and -9.5‰ VPDB, respectively. Each of these periods is exclusively composed of aragonite and for the majority of the Sn phase, aragonite grew at growth rates ≤ 0.33 mm/yr, which is below the overall DP1 growth rate average of 0.35 mm/yr. S1 and S2 are both bounded by layers of calcite before and after the Sn periods and have relatively darker luminescence than the calcite layers above and below. Within all three Sn periods there are variations of fabrics that progress from a fabric with a finer crystal width to a wider, coarser crystal width, which correlate with higher $\delta^{13}\text{C}$ values. CA is found only in S3, which is the Sn period with the greatest $\delta^{13}\text{C}$ values (-4.7 to -3.0‰ VPDB) in the 4600-yr record. The combination of these relationships indicates that the climate during the Sn periods was drier than what was recorded in comparatively wetter time periods (Table 5.3).

Wetter phases primarily occurred in cycles during 1285 to 14 BP (Segment A) with average growth rates of 0.53 mm/yr relative to the drier period from 4600 to 1285 BP (Segment B) with slower average growth rates of 0.27 mm/yr. Luminescence of calcite layers in Segment A is greater than that of aragonite layers in the same segment indicating that calcite layers contain greater amounts of humic and/or fulvic acids due to greater amounts of organic matter above the cave. Two distinct wetter episodes occurred at 1261 BP, and from 202 to 170 BP. Each had consecutively lower $\delta^{13}\text{C}$ and $\delta^{18}\text{O}$ values and the presence of 34 years and 32 years of calcite precipitation, respectively.

Table 5.1 Uranium and thorium isotopic compositions and ^{230}Th ages for DP1 using ICP-MS as analyzed by Ben Hardt (BH) and Hai Cheng (HC) at the University of Minnesota Isotope Laboratory.

Sample ID	Analyzed By ^g	^{238}U ppb		^{232}Th ppt		$d^{234}\text{U}$ measured		[$^{230}\text{Th}/^{238}\text{U}$] activity		^{230}Th Age uncorrected		^{230}Th Age corrected ^{c,e}		$\delta^{234}\text{U}_{\text{initial}}$ corrected		^{230}Th Age corrected (BP) ^f	
DP1-T	BH	2073.0	±5.7	209	±1	300.1	±1.9	0.000866765	±0.00024	73	±21	71	±21	300.2	±1.9	14	±21
DP1-103	BH	4840.0	±9.6	37	±1	284.5	±1.6	0.00234777	±0.00005	200	±4	200	±4	284.7	±1.6	143	±4
DP1-250	BH	1091.7	±2.7	34	±1	299.6	±2.8	0.005224762	±0.00019	440	±16	439	±16	300.0	±2.8	382	±16
DP1-315	BH	3104.7	±10.9	48	±1	269.4	±2.9	0.008777115	±0.00015	757	±13	757	±13	270.0	±2.9	700	±13
DP1-448	HC	1756	±2	776	±16	277.1	±2.0	0.0103	±0.0000	882	±4	871	±8	278	±2	811	±8
DP1-450	BH	1105.4	±1.9	28617	±101	279.2	±1.8	0.014150384	±0.00054	1214	±46	624	±420	279.7	±1.8	567	±420
DP1-550	BH	1940.3	±4.8	82	±1	292.9	±2.3	0.0138637	±0.00023	1177	±20	1176	±20	293.8	±2.3	1119	±20
DP1-570	HC	2269	±2	2269	±2	283.7	±1.9	0.0142	±0.0000	1210	±4	1208	±4	285	±2	1148	±4
DP1-654	HC	174.5	±0.3	137	±3	262.7	±3.6	0.0176	±0.0003	1533	±28	1515	±31	264	±4	1455	±31
DP1-671	BH	1902.8	±4.1	287	±1	287.4	±2.0	0.01576526	±0.00021	1345	±18	1341	±18	288.5	±2.0	1284	±18
DP1-690	BH	2376.5	±5.0	242	±2	295.1	±2.1	0.015857611	±0.00021	1344	±18	1342	±18	296.2	±2.1	1285	±18
DP1-705	BH	1421.5	±2.4	210	±2	294.3	±1.7	0.023006759	±0.00031	1957	±27	1953	±27	296.0	±1.7	1896	±27
DP1-709	HC	4181	±5	182	±4	287.5	±1.6	0.0167	±0.0000	1421	±3	1420	±3	289	±2	1360	±3
DP1-775	BH	3763.8	±7.1	25	±2	296.0	±1.6	0.018175303	±0.00019	1541	±16	1541	±16	297.2	±1.6	1484	±16
DP1-859	HC	3235	±4	143	±3	291.4	±1.7	0.0198	±0.0000	1682	±4	1681	±4	293	±2	1621	±4
DP1-1003	HC	3076	±3	114	±2	320.4	±1.6	0.0341	±0.0001	2851	±6	2850	±6	323	±2	2790	±6
DP1-1052	HC	3604	±4	123	±3	361.5	±1.8	0.0388	±0.0001	3147	±7	3146	±7	365	±2	3086	±7
DP1-1084	HC	5595	±8	136	±3	365.0	±1.9	0.0422	±0.0001	3420	±9	3419	±9	369	±2	3359	±9
DP1-1131	HC	3125	±4	624	±13	336.7	±1.7	0.0440	±0.0001	3641	±8	3637	±8	340	±2	3577	±8
DP1-1189	HC	2835	±3	536	±11	326.9	±1.9	0.0468	±0.0001	3906	±9	3902	±9	330	±2	3842	±9
DP1-1234	HC	2282	±3	167	±3	327.0	±2.1	0.0483	±0.0001	4033	±10	4031	±10	331	±2	3971	±10
DP1-1285	HC	2460	±3	735	±18	319.1	±1.8	0.0494	±0.0003	4157	±28	4151	±28	323	±2	4091	±28
DP1-1374	HC	4029	±5	3597	±72	334.5	±1.8	0.0539	±0.0001	4488	±10	4468	±17	339	±2	4408	±17
DP1-B	BH	4705.8	±19.0	1226	±5	353.0	±2.3	0.056557755	±0.00039	4655	±33	4649	±33	357.6	±2.4	4592	±33
DP1-1475	HC	3759	±5	3170	±64	349.2	±2.0	0.0569	±0.0001	4692	±12	4674	±17	354	±2	4614	±17

Analytical errors are 2s of the mean. $d^{234}\text{U} = (r^{234}\text{U}/^{238}\text{U})_{\text{activity}} - 1) \times 1000$.

^b $d^{234}\text{U}_{\text{initial}}$ corrected was calculated based on ^{230}Th age (T), i.e., $d^{234}\text{U}_{\text{initial}} = d^{234}\text{U}_{\text{measured}} \times e^{234\lambda T}$, and T is corrected age.

^c $^{230}\text{Th}/^{238}\text{U}_{\text{activity}} = 1 - e^{-1230T} + (d^{234}\text{U}_{\text{measured}}/1000)[I_{230}/(I_{230} - I_{234})](1 - e^{-(1230 - 1234)T})$, where T is the age.

Decay constants are $9.1577 \times 10^{-6} \text{ yr}^{-1}$ for ^{230}Th , $2.8263 \times 10^{-6} \text{ yr}^{-1}$ for ^{234}U , and $1.55125 \times 10^{-10} \text{ yr}^{-1}$ for ^{238}U (Cheng et al., 2000).

^d The degree of detrital ^{230}Th contamination is indicated by the [$^{230}\text{Th}/^{232}\text{Th}$] atomic ratio instead of the activity ratio.

^e Age corrections were calculated using an average crustal $^{230}\text{Th}/^{232}\text{Th}$ atomic ratio of $4.4 \times 10^{-6} \pm 2.2 \times 10^{-6}$.

Those are the values for a material at secular equilibrium, with the crustal $^{232}\text{Th}/^{238}\text{U}$ value of 3.8. The errors are arbitrarily assumed to be 50%.

^f B.P. stands for "Before Present" where the "Present" is defined as the year 1950 A.D.

^g BH (Ben Hardt) samples were analyzed in 2007. HC (Hai Cheng) samples were analyzed in 2010. BP date corrections are made to the respective years.

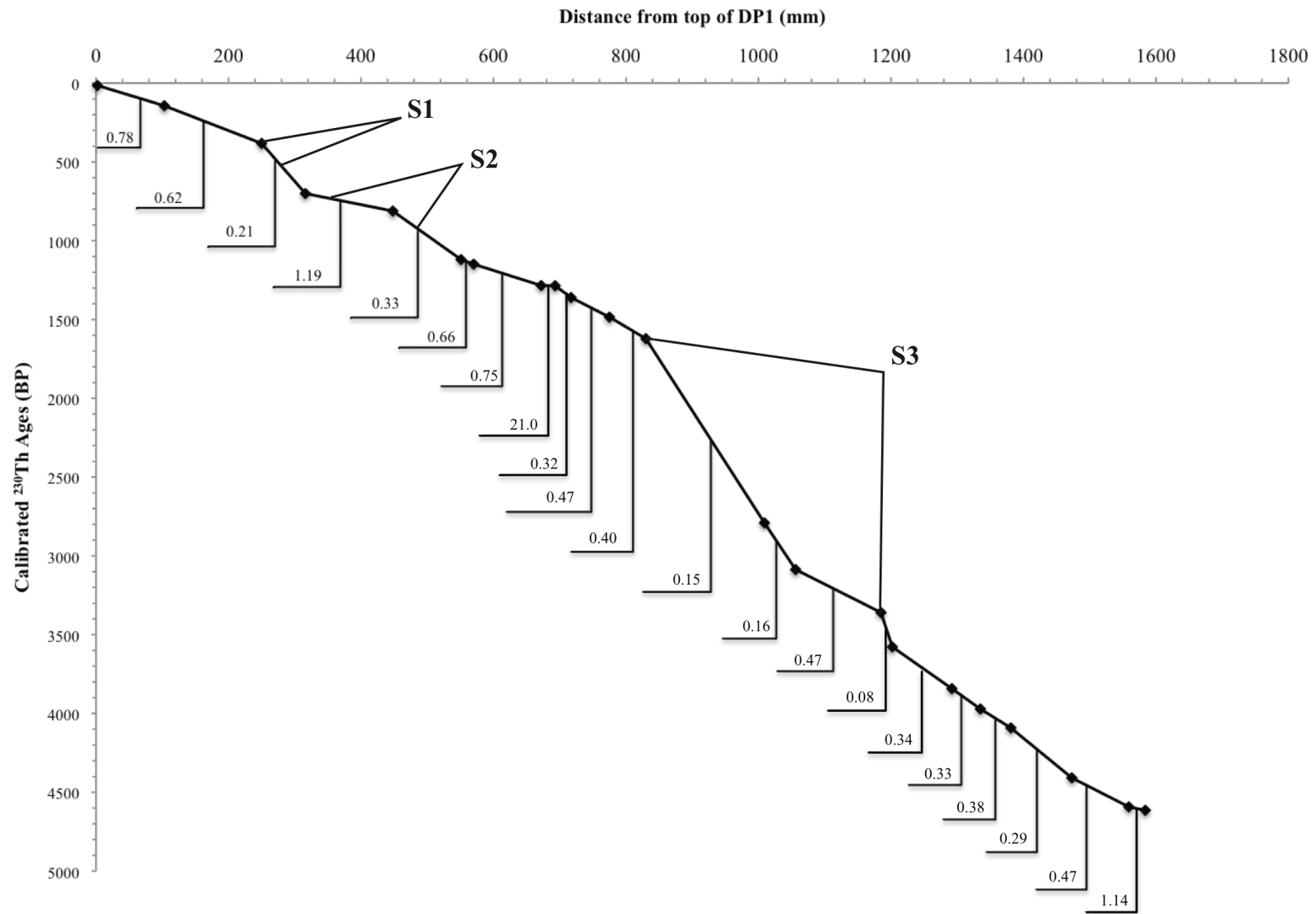


Figure 5.1. Calculated growth rates (mm/yr) between U/Th dated intervals of DP1.

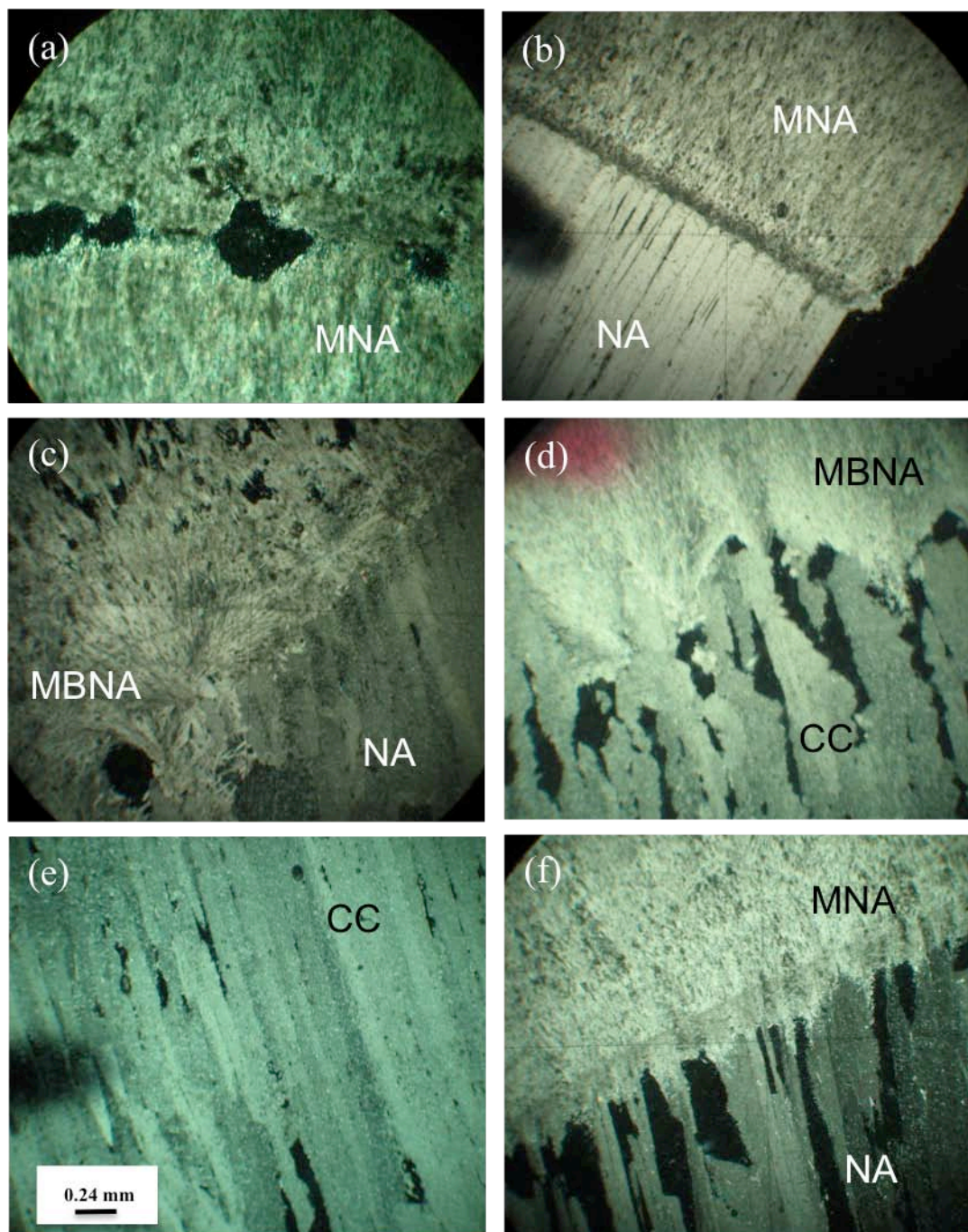


Figure 5.2. Photomicrographs all at the same scale of dissolution and aridification surfaces of (a) dissolution cavities in layers of massive needle aragonite (MNA) at 113 mm; (b) needle aragonite (NA) eroded with a layer of detritus that is bounded by MNA at 250 mm; (c) massive botryoidal needle aragonite (MBNA) overlying NA moving toward the flank of the layer at 250 mm; (d) MBNA forming from calcite with very jagged intercrystalline boundaries at 86 mm; (e) fabric just below jagged calcite at 86 mm is columnar calcite (CC) with smooth intercrystalline boundaries; (f) MNA forming from very jagged NA at 241 mm.

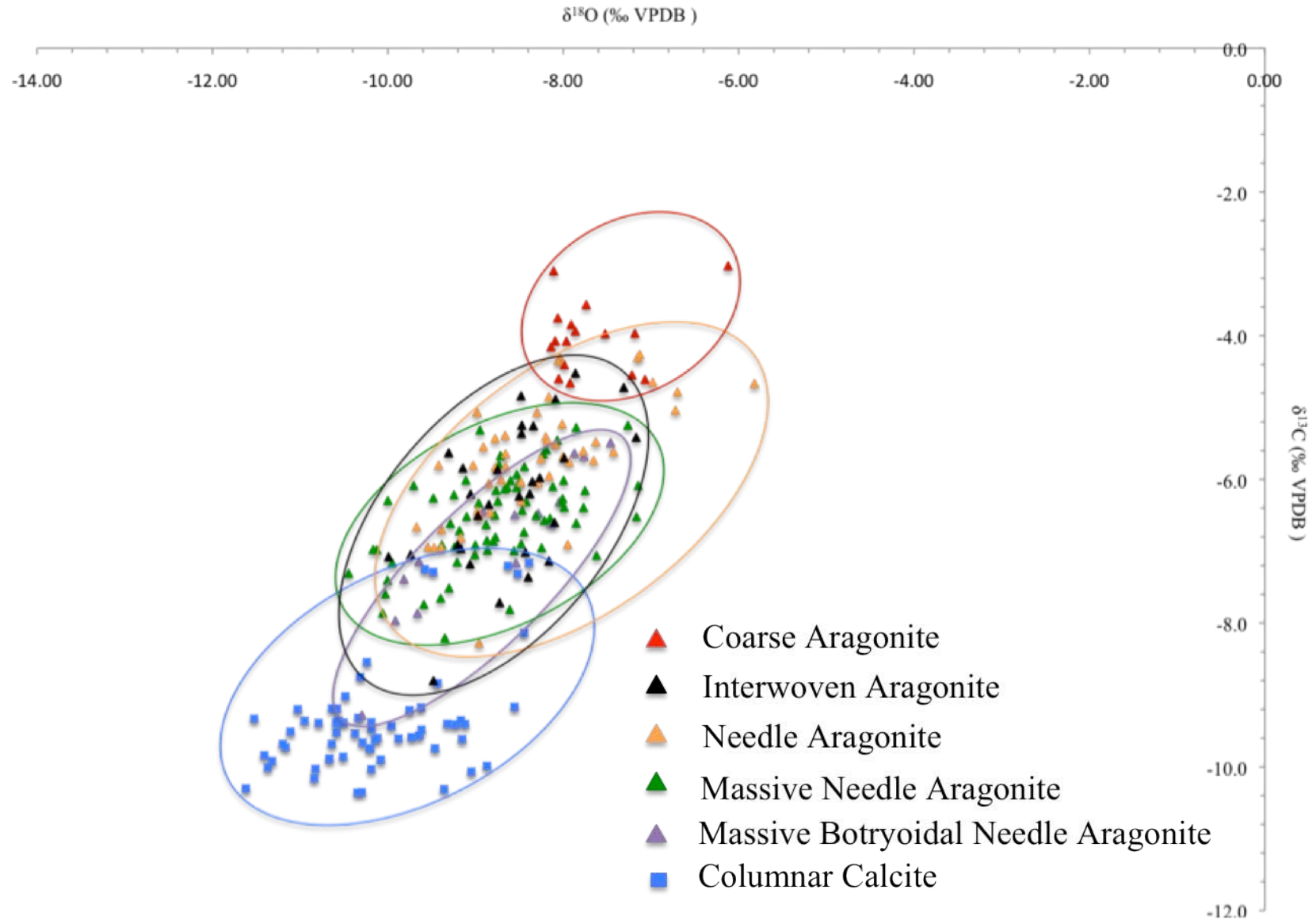


Figure 5.3 DP1 fabrics for 243 of 287 stable isotope values. Ellipses are included as a visual aid for the reader to better identify how the data grouped by fabric type.

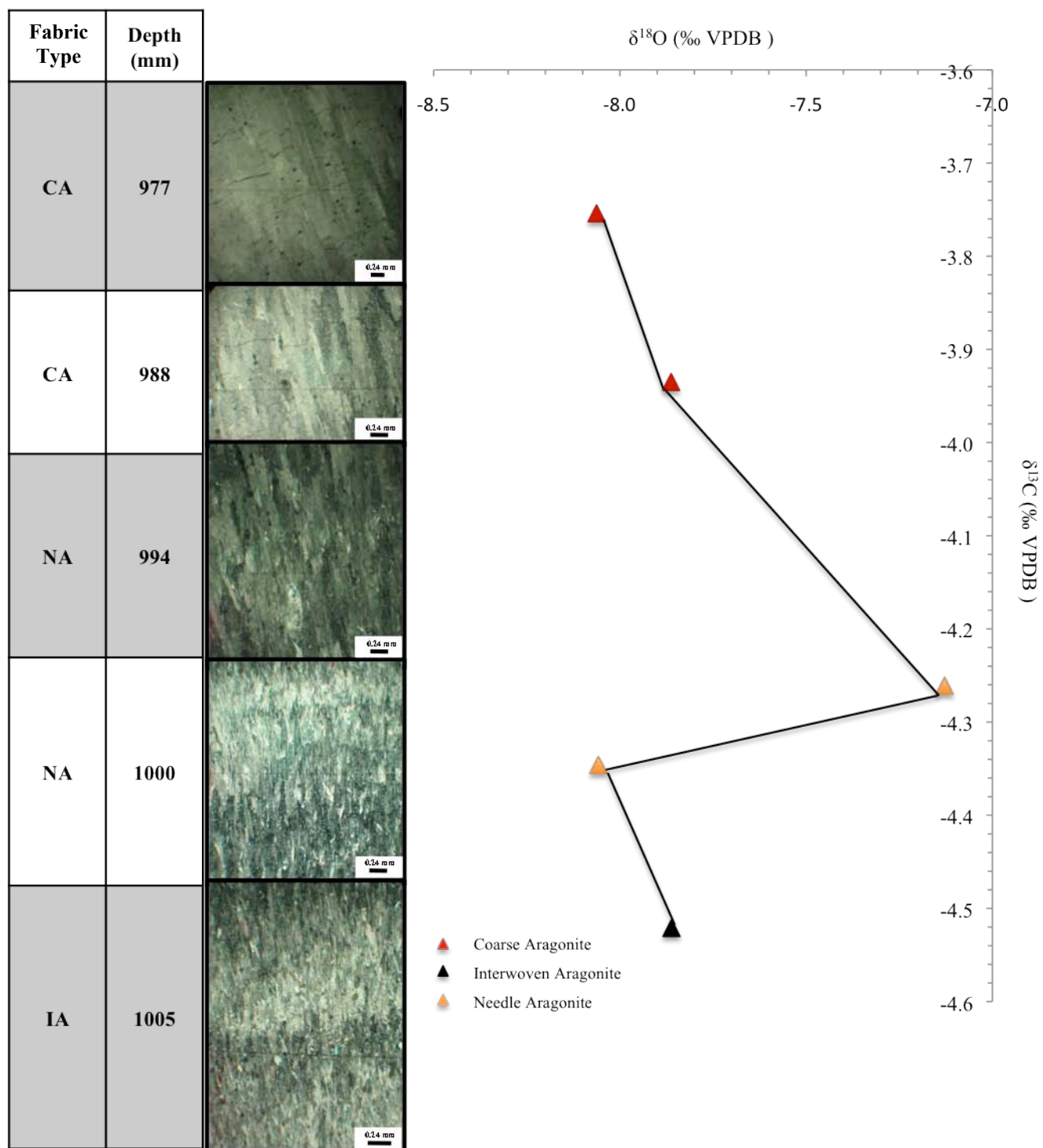


Figure 5.4 Photomicrographs of a fabric progression from 1005 to 977 mm from the top of DP1. Corresponding isotope data for each fabric show an increase in $\delta^{13}\text{C}$ values crystal widths measured in the fabrics become wider from 1005 to 977 mm.

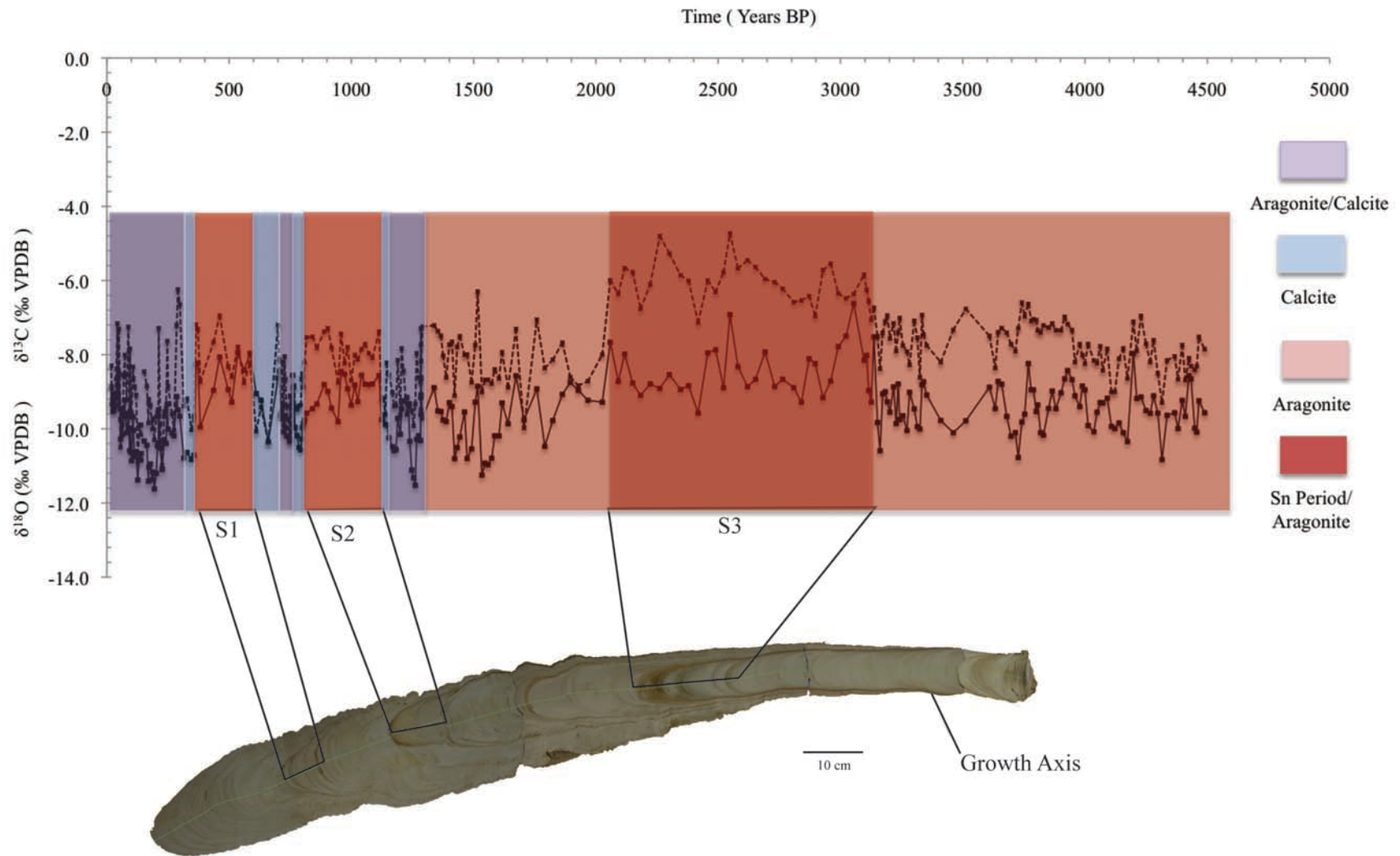


Figure 5.5 DP1 time series using $\delta^{13}\text{C}$ and $\delta^{18}\text{O}$ (using corrected aragonite values) and mineralogy to identify slow growth periods S1 (586-364 BP), S2 (1113-800 BP), and S3 (3126-2059 BP). DP1 widths narrowed during Sn periods.

Table 5.2 Summary of slow growth periods S1 to S3 for DP1.

Period (Sn)	Depth (mm)	Age (BP)	Age (AD/BC)	Growth Rate (mm/yr)
S1	293-241	586-364	AD 1364-1586	0.21
S2	549-450	1113-800	AD 837-1150	1.19 (811-800 BP) 0.33 (1113-811 BP)
S3	1075-861	3126-2059	109 BC-AD 1187	0.15 (2790-2059 BP) 0.16 (3086-2790 BP) 0.47 (3126-3086 BP)

Table 5. 3. Summary of slow growth interval (*Sn*) characteristics.

<i>Sn</i> Characteristics	Likely Immediate Causes	Broader Environmental Significance
Slow growth	Slower drip rate	Less rainfall
Diminished DP1 width	Slower drip rate	Less rainfall
Greater $\delta^{18}\text{O}$	Less rainfall	Less rainfall
Greater $\delta^{13}\text{C}$	Less vegetation	- Less rainfall - Less vegetation
Aragonite mineralization	- Less drip water - Greater amounts of time for degassing of CO ₂	- Less rainfall - More evaporative conditions
Coarse aragonite (CA) mineralization	- Extremely low drip rate - Even greater amounts of time for degassing of CO ₂	- Little to no rainfall - More evaporative conditions

CHAPTER 6

DISCUSSION

6.1 $\delta^{13}\text{C}$ and $\delta^{18}\text{O}$ Relationships to Sn Periods

Stalagmite $\delta^{13}\text{C}$ values are influenced by: (1) the C isotope exchange between meteoric waters and bedrock above the cave; (2) the composition and amount of vegetation above the cave; and (3) kinetic fractionation of C in precipitating waters, especially due to CO_2 degassing (Brook et al., 2010; McDermott, 2004). All of these influences have a direct relationship to the *amount* of rainfall above the cave, such that stalagmite $\delta^{13}\text{C}$ values reflect variations in the amount of rainfall and can therefore be used to interpret past rainfall records. Lower $\delta^{13}\text{C}$ values in cave calcite have been shown by Bar-Mathews et al. (1996) and Baker et al. (1997) to be caused by an increase in carbonic acid production through enhanced root respiration and microbial activity. Since soil productivity is a direct function of the amount of rainfall (Fox and Koch, 2003), $\delta^{13}\text{C}$ is an indicator of relative rainfall amounts. Hence, lower $\delta^{13}\text{C}$ values would signify more rainfall and greater $\delta^{13}\text{C}$ would indicate less rainfall as the $^{13}\text{C}/^{12}\text{C}$ ratio decreases. In the latter situation less rainfall would provide less water to the surface and groundwater systems, in turn producing less vegetation. All of these variables are indicative of a relative drier climate.

Three slow growth periods occur in DP1: 3126 to 2059 BP (S3), 1113 to 800 BP (S2), and 586 to 364 BP (S1). Each of these Sn periods is marked by greater $\delta^{13}\text{C}$ ranging from -8.8 to -4.7‰ VPDB compared to non-Sn periods, which have $\delta^{13}\text{C}$ ranging from -11.0 to -6.2‰ VPDB. Greater $\delta^{13}\text{C}$ values can be linked to less vegetative cover above the cave, and therefore less regional rainfall during periods of more arid climate. This further suggests that climate conditions during the Sn phases likely supported a C4 biomass.

Stalagmite $\delta^{18}\text{O}$ values represent both the $\delta^{18}\text{O}$ of the cave drip water and the temperature of the cave in which the stalagmite formed (McDermott, 2005). Stalagmite $\delta^{18}\text{O}$ also reflects changes in the

amount of rainfall based on studies that have shown positive correlation between instrumental rainfall data and $\delta^{18}\text{O}$ values in stalagmites (Brook et al., 2010), where lower $\delta^{18}\text{O}$ signifies more rainfall due to the ‘amount effect’ (Dansgaard, 1964; Rozanski et al., 1993). Holmgren et al. (2003) argued that *greater* $\delta^{18}\text{O}$ values represented more rainfall in the Cold Air Cave, South Africa stalagmite T8 record. Evidence of greater $\delta^{18}\text{O}$ values recorded in DP1 parallel the interpretation of Brook et al. (2010) for Wonderwerk Cave, South Africa since the DP1 $\delta^{18}\text{O}$ values are coincident with greater $\delta^{13}\text{C}$ during the Sn periods when aragonite was precipitated, all signifying less rainfall during these slow growth periods. DP1 $\delta^{18}\text{O}$ values during Sn phases range from -10.0 to -6.6‰ VPDB. Relatively lower $\delta^{18}\text{O}$ values ranging from -11.6 to -7.5‰ VPDB are recorded in DP1 during wetter, calcite precipitating periods. Overall, DP1 provides a southern African record where drier, more arid climate is represented by greater $\delta^{13}\text{C}$ and $\delta^{18}\text{O}$ values, and wetter climate by lower $\delta^{13}\text{C}$ and $\delta^{18}\text{O}$ values.

6.2 Potential Causes of Alternating Aragonite and Calcite in DP1

In southern Africa, most speleothems that form in the dolomitic Transvaal Supergroup are aragonitic, likely due to greater concentrations of Mg^{2+} dissolving from the bedrock and generally arid conditions (Holmgren et al., 1999). A few specimens, including DP1 from Dante Cave, Namibia; W5 from Wolkberg Cave, South Africa (Holzkämper et al., 2009); LII4 from Lobatse II Cave, Botswana (Holmgren et al., 1995); and an unnamed stalagmite from Drotsky’s Cave, Botswana (Railsback et al., 1994) provide records with both aragonite and calcite. The fluctuation between the two CaCO_3 polymorphs suggests different geochemical and microclimatic conditions that are connected to climate variations during stalagmite formation. In particular, aragonite has been identified as a polymorph that forms in more arid conditions (Holzkämper et al., 2009). This interpretation can also be applied to slow growth periods for the DP1 climate record.

Alternating layers of aragonite and calcite could be influenced by elemental sources from surrounding bedrock shifting the Mg/Ca and/or Sr/Ca ratios, changes in drip water amount, variability between degassing and evaporation within the cave, and/or shifts in temperature. McDonald et al. (2004) investigated Mg/Ca and Sr/Ca ratios and their relationship to drought conditions in a 30-month study on

the hydrochemistry of cave drip water from Kooringa Cave, eastern Australia during the AD 2002 to 2003 El Niño event. This 1-yr event caused the study site to experience 10 consecutive months of drought conditions. McDonald et al. (2004) collected data from two drip sites before, during, and after the drought. During the drought they observed a decrease in the amount of cave drip water and an increase in $[Mg/Ca]_{drip}$ and $[Sr/Ca]_{drip}$, which they attributed to increased residence times of CO_2 -rich percolation waters in the soil and bedrock. Longer residence times allow these waters to move closer to chemical equilibrium with the soil carbonate and bedrock, producing higher dissolved loads. Lower amounts of percolating water (i.e. during dry periods) cause less recharge to fracture veins, thus supersaturating the fluid with $CaCO_3$ as CO_2 in the air pockets degasses. This triggers $CaCO_3$ precipitation along the veins, preferentially removing Ca^{2+} and leaving the solution enriched in trace elements such as Mg^{2+} (Fairchild et al., 2000; McDonald et al., 2004). McDonald et al. (2004) observed $[Mg/Ca]_{drip}$ and $[Sr/Ca]_{drip}$ ratios at Kooringa Cave decreased and drip rates increased when the system returned to a positive moisture balance.

Railsback et al. (1994) suggested that increases in Mg/Ca from the bottom of calcite layers to just below aragonite layers, along with possible increases in temperature, caused aragonite to form in the alternating calcite and aragonite stalagmite from Drotsky's Cave, Botswana. Combining the results from McDonald et al. (2004), Railsback et al. (1994) and others who postulate increased Mg/Ca ratios promote aragonite formation (Holzkämper et al., 2009; Talma et al., 1974; Frisia et al., 2002) suggests that in DP1, aragonite, which grew during Sn periods and other periods of time with greater $\delta^{13}C$ and $\delta^{18}O$, may have formed from increases in Mg/Ca ratios. The Mg/Ca ratio could have increased from decreases in rainfall, thus causing increased residence times of meteoric waters in the bedrock allowing for a greater enrichment of trace elements in the drip water forming DP1. Lower amounts of rainfall would therefore signify drier climate conditions, possibly associated with warmer air temperatures. Future analysis of trace elements in DP1 would help explore this explanation.

6.3 Isotopic Variation with Differences in DP1 Fabric Classifications

Little evaluation of isotopic differences between stalagmite fabrics has been done, particularly in southern Africa. Holzkämper et al. (2009) did a comparison between $\delta^{13}\text{C}$ and $\delta^{18}\text{O}$ values and mineralogy in a Pleistocene stalagmite from Wolkberg Cave, South Africa. They found that, apart from a hiatus from 46.3 ka to 40.1 ka, there was no correlation between $\delta^{13}\text{C}$ and $\delta^{18}\text{O}$ along the growth axis with respect to alteration between calcite and aragonite. However, they identified a weak correlation between $\delta^{13}\text{C}$ and $\delta^{18}\text{O}$ in aragonite ($R^2 = 0.32$).

Using $R^2 = 0.5$ as a threshold of significance based on variation within the data, there is a weak correlation between $\delta^{13}\text{C}$ and $\delta^{18}\text{O}$ in all calcite samples ($R^2 = 0.24$) and a greater correlation between $\delta^{13}\text{C}$ and $\delta^{18}\text{O}$ and all aragonite samples ($R^2 = 0.44$). When aragonite is classified by different fabrics, the $\delta^{13}\text{C}$ and $\delta^{18}\text{O}$ correlation for one fabric (massive botryoidal needle aragonite - MBNA) was significant ($R^2 = 0.83$). This may suggest that MBNA grew during the greatest range of rainfall and vegetation conditions that existed above Dante Cave since it is the fabric that explains the greatest amount of variance between $\delta^{13}\text{C}$ and $\delta^{18}\text{O}$. Contrastingly, coarse aragonite (CA) has the smallest R^2 value for all of the DP1 fabrics ($R^2 = 0.06$), which may indicate that CA grew in the most restricted types of rainfall and vegetation conditions above Dante Cave. The evidence that CA only grew during the S3 interval, had the greatest $\delta^{13}\text{C}$ and $\delta^{18}\text{O}$ values for the entire DP1 record, and had some of the slowest growth rates in the record during the CA precipitation (0.15 to 0.16 mm/yr) supports this hypothesis. For all CaCO_3 samples, there is a strong correlation between $\delta^{13}\text{C}$ and $\delta^{18}\text{O}$ ($R^2 = 0.64$) further supporting that the amount of rainfall above the cave is directly related to the amount of vegetation growing above the cave.

Brook et al.'s (2010) fabric analysis of stalagmite W-1 at Wonderwerk Cave, South Africa is also relevant to the DP1 record (see Section 3). Brook et al. (2010) determined the following three petrographic fabrics: (1) a layered fabric, which was interpreted to show dry conditions, is formed from a thin film of water that produced regular spelean layers with only a few detritus grains larger than clay particles; (2) a microstromatolitic fabric, which represents modified dry conditions when climate was relatively drier, or when local air flow conditions promoted higher rates of evaporation; and (3) a

concretionary fabric, which records periods of high flow rate and large amounts of detrital deposition. They found that layered and micostromatolitic fabrics were formed during slower growth periods and had greater $\delta^{13}\text{C}$ and $\delta^{18}\text{O}$ values as compared to a concretionary fabric that formed during wetter periods with lower $\delta^{13}\text{C}$ and $\delta^{18}\text{O}$ values. Similarly, coarse aragonite (CA) fabrics formed during the Sn periods of DP1 and had the greatest $\delta^{13}\text{C}$ and $\delta^{18}\text{O}$ values as compared to the other fabrics. Both the W-1 and DP1 records suggest that fabrics can be used to differentiate between wet and dry phases, as well as more detailed variation within arid phases.

Frisia et al. (2000) also defined a fabric classification system for stalagmites. Their classifications were based on a suite of active and inactive stalagmite samples from the Italian Alps and southwestern Ireland and were primarily focused on calcite fabrics, and not aragonite fabrics. Frisia et al. (2000) defined the following fabrics found in stalagmites: columnar (elongate c-axis crystals with a length-to-width ratio $\leq 6:1$; $\cong 4$ to $100\ \mu\text{m}$ wide and $\geq 100\ \mu\text{m}$); fibrous or elongate (columnar fabrics with crystal length-to-width ratios greatly exceeding $6:1$); microcrystalline (white and dark-brown laminae with crystals $< 4\ \mu\text{m}$ wide and $5\text{-}50\ \mu\text{m}$ long); and dendritic (branching polycrystals $> 100\ \mu\text{m}$ long and $\cong 10\ \mu\text{m}$ wide; porous fabric). When correlated with drip water concentration data collected from the caves, Frisia et al. (2000) found that the dendritic fabric was associated with speleothems characterized by periods of rapid dripping that alternated with long periods of extremely slow drip that became impractical to monitor. They observed that dendritic fabrics were found in sections of the stalagmite with a reduced diameter, which is often associated with a lower flow regime.

Comparatively, columnar and fibrous fabrics were respectively associated with constant and higher drip rates. The dendritic drip water was measured to have a relatively low supersaturation with respect to CaCO_3 . Dendritic fabrics were the most enriched with the greatest $\delta^{13}\text{C}$ values at a given $\delta^{18}\text{O}$ value when compared with columnar and microcrystalline fabrics formed in the same cave. Dendritic $\delta^{18}\text{O}$ values were about the same, or slightly greater, in comparison to columnar and microcrystalline fabrics. Based on their study, Frisia et al. (2000) concluded that dendritic fabrics formed when 1) there was exchange with the outer atmosphere in the cave, or 2) prolonged degassing occurred. They also

determined that speleothem calcite fabrics are controlled by supersaturation and discharge, and not temperature.

Although a drip water comparison was not available for the study of DP1, the fabric analysis shows that the coarse aragonite (CA) fabric has greater $\delta^{13}\text{C}$ values (-5.4 to -3.0‰ VPDB) compared to the other fabrics classified in DP1. Needle aragonite (NA) exhibits the next greatest $\delta^{13}\text{C}$ values (-9.7 to -4.2‰ VPDB) in DP1 and is most often the nucleating surface for CA. Combined isotopic, mineralogical, and growth rate data indicate that CA grew during some of the slowest growth periods within the DP1 4600-yr record, suggesting that it is associated with more extensive arid, evaporative conditions. Brook et al.'s (2010) fabric analysis of stalagmite W-1 at Wonderwerk Cave, South Africa also supports this relationship (See Section 3.2.1). Brook et al. (2010) found for W-1 that layered and microstromatolitic fabrics were formed during slower growth periods and had greater $\delta^{13}\text{C}$ and $\delta^{18}\text{O}$ values as compared to a concretionary fabric that formed during wetter periods with lower $\delta^{13}\text{C}$ and $\delta^{18}\text{O}$ values. Layered and microstromatolitic fabrics were associated with drier conditions, just like CA and/or NA in DP1.

Gonzalez and Lohmann (1987) have shown that at any given isotopic composition of drip water, rapid and extended degassing results in greater $\delta^{13}\text{C}$ values, which may also occur with evaporation. This, in conjunction with the results from Frisia et al. (2000) and Brook et al. (2010), suggests that fabrics with greater $\delta^{13}\text{C}$ values with respect to the other fabrics in the same stalagmite (or potentially the same cave) may be indicators of dry phases, while fabrics of relatively lower $\delta^{13}\text{C}$ values may be indicators of wet phases. Fabric and isotopic correlation analysis, therefore, is another tool researchers can use to delineate dry and wet phases for the paleoenvironmental reconstruction of stalagmites.

6.4 DP1 Correlations to Other Southern African Paleoclimate Records

DP1 is interpreted to represent a generally wetter phase than the drier period before it; conversely, regional and cave conditions could have been too wet before DP1 started precipitating, causing the water table to increase and flood the cave. In either case, DP1 started forming at ca. 4600 cal yr BP and it precipitated under relatively dry conditions until ca. 1285 cal yr BP. Precipitation then progressed into a generally wetter phase at ca. 1285 cal yr BP to present. Correlating DP1 to other southern African

paleoclimate studies on a large scale (dry versus wet phases) is difficult because records are geographically scattered, often discontinuous, and or poorly dated. Chase (2009) compiled several southern African climate studies to compare dry and wet periods during the Quaternary (Figure 6.1). Only a few show drier conditions than at present from ca. 4600 to 1285 BP. Lack of strong correlations may point to the great variation in local climate conditions at the site, and or the unreliable nature of the proxy-medium being used for paleoclimate analysis. This draws attention to the greater need for more high-resolution, well-dated records from southern Africa.

However, on a finer scale the DP1 paleoclimate record connects to other southern African records. Deposition of DP1 began ca. 4600 cal yr BP, which correlates with the start of deposition of speleothems at Drotzky's Cave in Botswana (Brook et al., 1990), deposition of stalagmite T5 at Cold Air Cave, South Africa from 4400 to 4000 BP that was then followed by a 3000-yr hiatus (Repinski et al., 1999), a high lake level at Lake Ngami in Botswana from 4600 to 3500 BP (Brook et al., 2007), and higher lake levels at 4000 BP at Etosha Pan (Brook et al., 2007). Increased humid conditions were recorded at about the same time in the Klein Spitzkoppe hyrax middens in eastern Namibia (Chase et al., 2009), as well as from 8000 to 4000 BP in the southern Kalahari dune activation records (Chase, 2009). With the exception of Cold Air Cave, these are the closest available paleoclimate records to Dante Cave, with the cave and hyrax midden proxies being the most comparable in terms of resolution. All of these records suggest that at the time DP1 started to form, regional climate became relatively wetter than the time period before it.

Portions of the DP1 Sn periods, as well as other notable isotopic and depositional variations outside of the Sn periods, also correlate to other paleoclimate records. In DP1, S3 occurred from 3126 to 2059 BP, with aragonite being deposited continuously from 4600 to 1285 BP, suggesting an overall drier climate. The southern Kalahari dune activation records indicate a drier period from 4000 to 2000 BP (Chase, 2009) (Figure 6.1). During the same time interval at Drotzky's Cave, speleothem deposition did not occur, but resumed from 2000 BP to the present (Brook et al., 1990). Records at Wonderwerk Cave, South Africa show that at ca. 4000 BP markedly greater $\delta^{13}\text{C}$ was recorded, which is also the case in the

DP1 record (Figure 6.2). Closer to Dante Cave at lake Otjikoto, Scott et al. (1991) interpreted pollen spectra to indicate drier conditions at 4000 BP. At Cango Cave, South Africa C3 vegetation (i.e. wetter conditions) covered the area above the cave near the last glacial maximum, and starting at about 5000 BP, C4 plants (i.e. drier conditions) progressively increased with a $\delta^{13}\text{C}$ maximum at about 2000 BP. This coincides with the end of the S3 event at Dante Cave at about 2059 BP. Relationships for S1 and S2 are further described in Section 6.5.

6.5 DP1 Correlation to Global Paleoclimate Records

DP1 and a few other southern African records have shown connections to more global events such as the Little Ice Age (LIA) (ca. AD 1400 to 1800) and the Medieval Warm Period (MWP) (ca. AD 900 to 1300) (Tyson et al., 2000). These events have been primarily described in records from the Northern Hemisphere, where during the LIA climate conditions became colder and wetter triggering glaciation, and where warmer and drier conditions marked the period of medieval warming. Some southern African paleoclimate records mark these periods by showing either in or out-of-phase relationships with the Northern Hemisphere records.

The DP1 record shows both in-phase and out-of-phase relationships with increases and decreases in the available isotopic data from the Austerlitz and Klein Spitzkoppe hyrax midden records and the Cold Air Cave stalagmites in South Africa (Figure 6.2), both of which are interpreted to have signals of the LIA and MWP. Within the region of Austerlitz, Namibia, Chase et al. (2010) determined that progressive aridification began at ca. 3800 cal yr BP (Figure 6.2.a). At the same time, DP1 was precipitating aragonite; however, DP1 and the Cold Air Cave stalagmites recorded relatively lower $\delta^{18}\text{O}$ (i.e. wetter conditions) showing an out-of-phase isotopic relationship with the Austerlitz record. Based on the Klein Spitzkoppe hyrax midden record, Chase et al. (2009) postulated that middle-eastern Namibia experienced an arid phase from 3500 to 1300 BP with rapid aridification at 4800 and 2700 BP (Figure 6.2.b). This record shows a progressive increase in $\delta^{15}\text{N}$ at the onset of the LIA from ca. AD 1650 to 1350 and the MWP from ca. AD 1250 to 850.

Tyson et al. (2000) and Holmgren et al. (2003) document the LIA and MWP by identifying changes in both $\delta^{13}\text{C}$ and $\delta^{18}\text{O}$ recorded in stalagmites from Cold Air Cave, South Africa. Lower $\delta^{18}\text{O}$ was recorded during the first half of the MWP at Cold Air Cave and rapidly increased at about 800 BP. DP1 shows just the opposite, with greater $\delta^{18}\text{O}$ during the S2 event during the first half of the MWP, and more fluctuating variations in $\delta^{18}\text{O}$ during the second half. These fluctuations in DP1 are coincident with alterations between aragonite and calcite.

At the onset of the LIA at about 550 BP (AD 1450), the Klein Spitzkoppe, Cold Air Cave, and DP1 records all appear to show greater isotopic values, indicating warmer climate conditions and would therefore illustrate an out-of-phase relationship with the onset of more extensive glaciation during the Neoglacial (Figure 6.2). At about AD 1700 an outlying warm period occurred in the middle of the LIA in the Northern Hemisphere. All three of the southern African paleoclimate records mentioned here show lower isotope values (i.e. wetter conditions) and relatively out-of-phase relationships with the Northern Hemisphere.

Although the connections are more distant, dry and wet phases on a larger scale may provide a context for the variations observed in DP1, even if just to recognize that change at approximately the same times was being documented in several global records. Mayewski et al. (2004) reviewed about 50 globally distributed paleoclimate records for the Holocene and found six periods of rapid climate change, three of which overlap with the DP1 Sn periods. These periods include: 3500 to 2500, 1200 to 1000, and 600 to 150 cal yr BP. Mayewski et al. (2004) reported that the interval 3500 to 2500 cal yr BP was marked by pronounced aridity in East Africa, the Amazon Basin, Ecuador, and the Caribbean/Bermuda region. At the same time cooler conditions were seen in SSTs off southern Africa and eastern South Africa. DP1 shows signals of both wet and dry conditions during this phase, with relatively wetter conditions from ca. 3500 to 3100 BP with 3100 BP showing more significant increase in wetness before a rapid shift to drier conditions, which lasted through ca. 1800 BP (S3). From 1200 to 1100 cal yr BP there was a slight increase in atmospheric CO_2 , which coincided with the drought-related collapse of the Maya civilization in the Yucatan (Hodell et al., 1991, 2001; Mayewski et al., 2004). S2 in DP1 begins at about

the same time at ca. 1100 BP. Finally, Mayewski et al. (2004) summarize that starting at ca. 600 cal yr BP the poles got colder and the tropical latitudes experienced wetter conditions. S1 in DP1 began at ca. 580 BP, suggesting an out-of-phase relationship with the general global trends.

Global trends are comparable with DP1 using the NorthGRIP ice core $\delta^{18}\text{O}$ data (Johnsen et al., 2001) (Figure 6.3). Ice core $\delta^{18}\text{O}$ is more analogous with temperature, whereas stalagmite $\delta^{18}\text{O}$ is more related to amounts of precipitation. In general, the past 8000 BP years can be divided into two step-down progressions of decreasing trends in ice core $\delta^{18}\text{O}$, where cooler conditions set in at about 4600 BP marking a Neoglacial phase at the start of the first step-down. This is at about the same time relatively wetter conditions developed at Dante Cave and DP1 began to precipitate. This suggests an in-phase relationship with the global temperature trends. During the first step-down period, DP1 grew in relatively arid conditions, precipitating only aragonite at a fairly constant rate. At the second step-down in the ice core record at ca. 1800 cal yr BP, DP1 continued to form aragonite until 1285 BP. Interestingly, the unnamed stalagmite from nearby Drotsky's Cave, Botswana (Railsback et al., 1994) started forming before 1460 ± 130 BP (the earliest dated sample available), which was about the same time of the second global step-down into cooler and wetter climate conditions. The unnamed stalagmite also started forming at the same time DP1 recorded the lowest $\delta^{18}\text{O}$ value (-11.5% VPDB) since it started precipitation at ca. 4600 cal yr BP, showing more evidence of regionally wetter conditions that may fit into a more global record of similar change.

After the second step-down, DP1 started to alternate between aragonite and calcite. This marked a comparatively overall wetter period at Dante Cave. In summary, DP1 shows isotopic, and often mineralogical, fluctuations at the same time as increases or decreases in $\delta^{13}\text{C}$ and $\delta^{18}\text{O}$ in other Holocene southern African and global paleoclimate records. Whether the relationships are in- or out-of phase between DP1 and the other records highlights the regional and global paleoclimate variations that are being studied today.

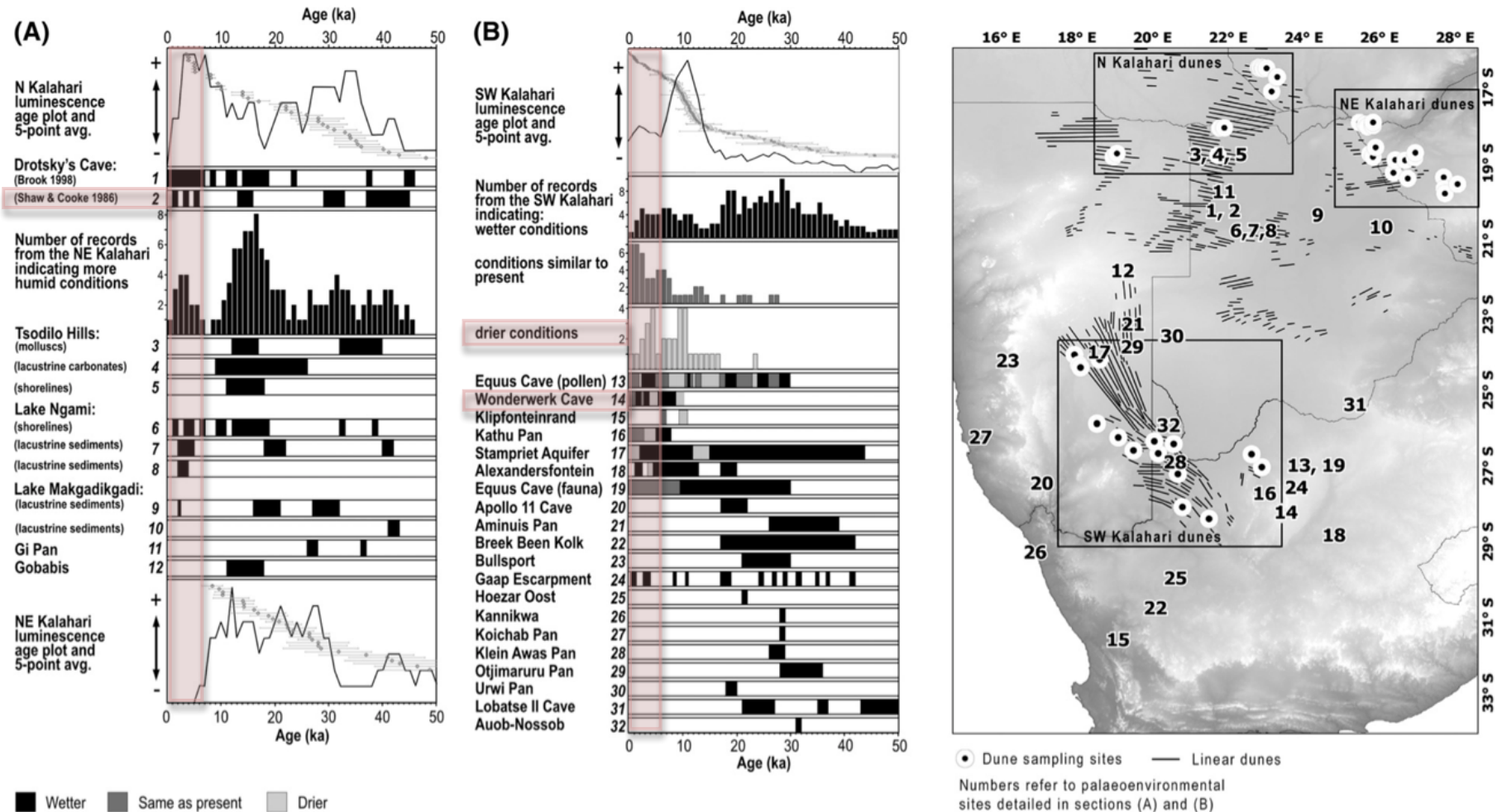


Figure 6.1. Comparison of DP1 to other southern African Quaternary paleoclimate records. This figure is from Chase (2009). Red overlays indicate DP1 age range from 4600 to 14 BP and records that show correlating dry and wet patterns. Site locations cited in Chase (2009). Some of the data presented in this figure may be non-continuous records, and/or dated using ^{14}C dating methods, which may yield older dates for materials affected by the hard water effect observed in parts of southern Africa (Brook et al., 2011).

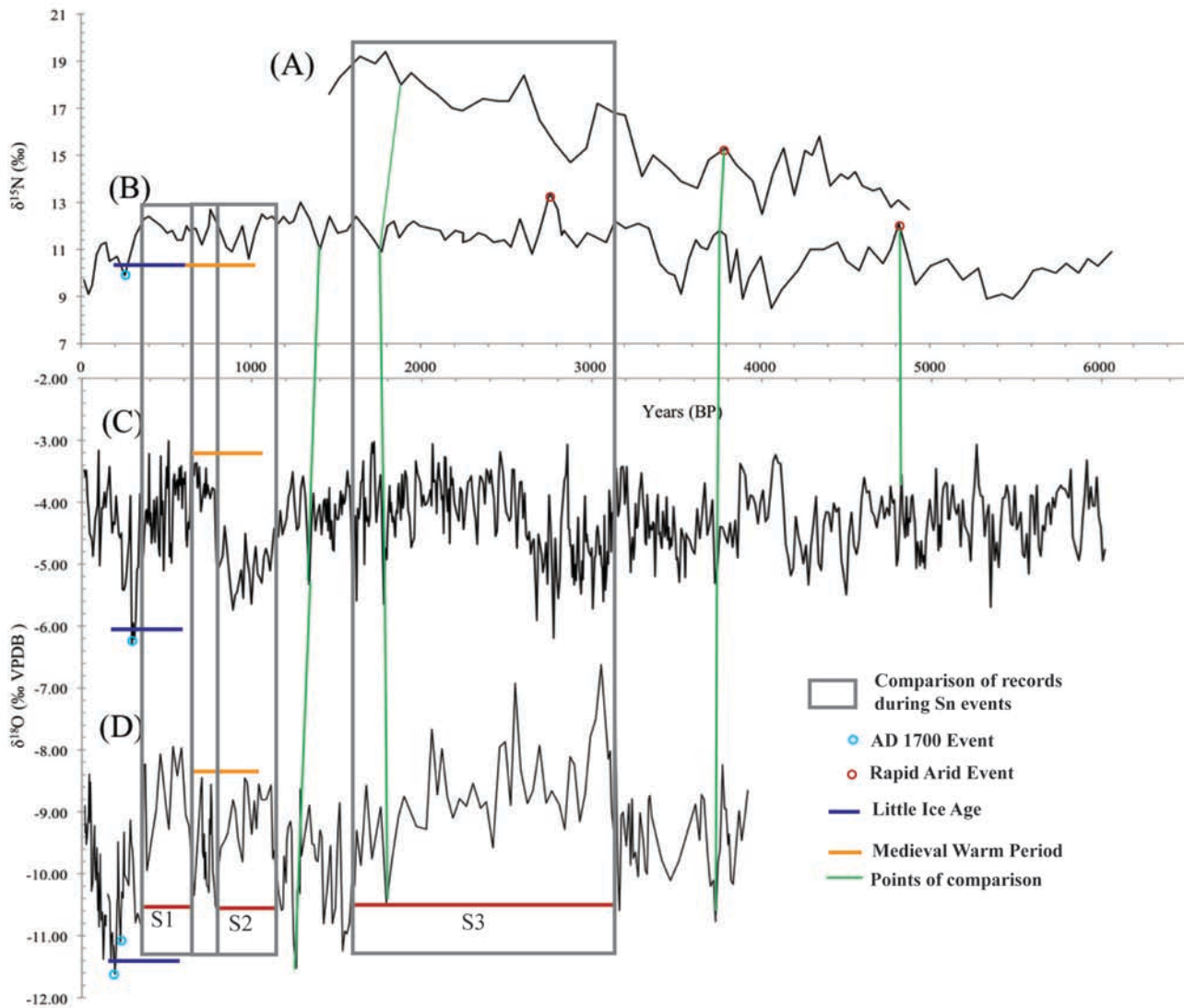


Figure 6.2 Holocene paleoclimate records in southern Africa (a) Austerlitz hyrax midden ca. 4500 to 1500 BP, Namibia (Chase et al., 2010); (b) Klein Spitzkoppe hyrax midden 11,700 to 0 BP Namibia (Chase et al., 2009) (c) Cold Air Cave stalagmites 10,000 to 6,000 BP, South Africa (Holmgren et al., 2003); (d) Dante Cave DP1 record 4600 to 14 BP, Namibia. Green lines highlight peaks that show both in and out-of-phase relationships between the records.

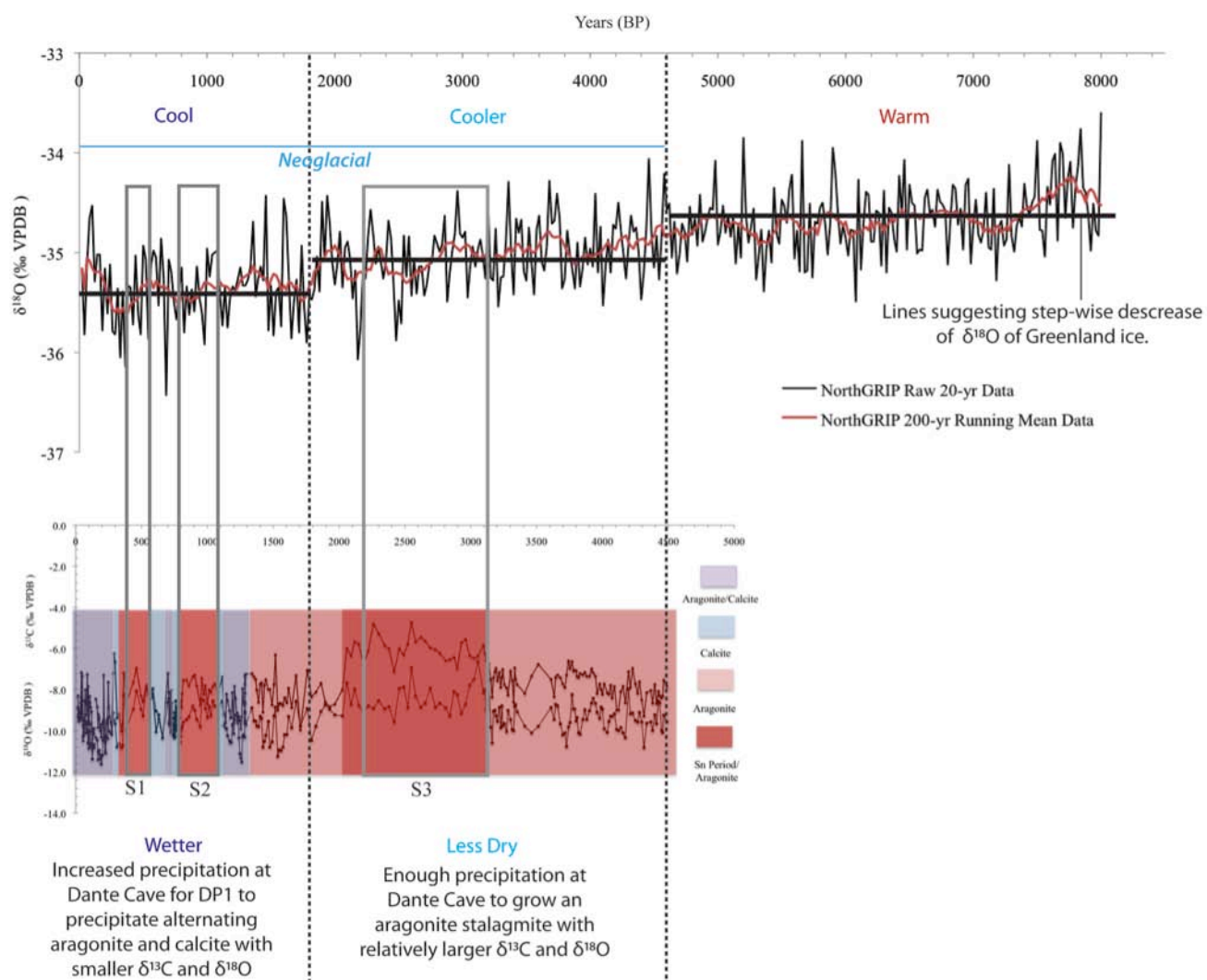


Figure 6.3 DP1 compared to the NorthGRIP ice core $\delta^{18}\text{O}$ record from 8000 to 20 BP (Johnsen et al., 2001).

CHAPTER 7

CONCLUSIONS

The conclusions from the paleoclimate reconstruction of DP1 are as follows:

1. Three slow growth periods (Sn) were determined from 3126 to 2059 BP (S3), 1113 to 800 BP (S2), and 586 to 364 BP (S1) based on the following: precipitation of only aragonite, comparatively greater $\delta^{13}\text{C}$ and $\delta^{18}\text{O}$ values recorded in the aragonite, decreases in growth rate, and decreases in overall stalagmite width.
2. At ca. 1300 BP a relative increase in the amount of rainfall with an increase in diversity or abundance in vegetation coverage above the cave caused calcite to start precipitating on DP1.
3. Variations in aragonite fabric types have a positive correlation to values of greater $\delta^{13}\text{C}$. Crystal width within IA, NA, and CA fabrics progressively widen in conjunction with greater $\delta^{13}\text{C}$ suggesting that changes in aragonite fabrics may be another tool for researchers to use when delineating dry periods from wet periods in stalagmite paleoclimate records.
4. All three Sn periods show both in and out-of-phase relationships with other southern African paleoclimate records that suggest evidence of climate change within the Little Ice Age (AD 1300-1800) and before the Medieval Warm Period (AD 1000-1300), respectively.
5. DP1 started forming at ca. 4600 cal yr BP, which was about the same time global $\delta^{18}\text{O}$ values recorded in the NorthGRIP ice core stepped down to a lower average from the previous 4500 years. This signaled a cooler phase relative to previous conditions in both the Northern and Southern Hemispheres.

REFERENCES

- Al-Aasm, I.S., Taylor, B.E., South, B., 1990, Stable isotope analysis of multiple carbonate samples using selective acid extraction: *Chemical Geology*, v. 80, 119-125.
- Baker, A., Barnes, W.L., Smart, P.L., 1996, Speleothem luminescence intensity and spectral characteristics: Signal calibration and a record of palaeovegetation change: *Chemical Geology*, v. 130, 65-76.
- Baker, A., Ito, E., Smart, P.L., McEwan, R.F., 1997, Elevated and variable values of (super 13) in a speleothems in British cave system: *Chemical Geology*, v. 136, 263-270.
- Baker, A., Genty, D., Smart, P., 1998, High-resolution records of soil humification and paleoclimatic change from variations in speleothem luminescence excitation and emission wavelengths: *Geology*, v. 26, 903-906.
- Bard, E., Rostek, F., Sonzogni, C., 1997, Interhemispheric synchrony of the last deglaciation inferred from alkenone palaeothermometry: *Nature*, v. 385, 707-710.
- Bar-Matthews, M., Ayalon, A., Kaufman, A., 1996, Late Quarternary paleoclimate in the eastern Mediterranean; stable isotope systematics of Soreq Cave speleothems: *Karst Waters Institute Special Publication*, v. 2, 10-12.
- Bar-Matthews, M., Marean, C.W., Jacobs, Z., Karkanas, P., Fisher, E.C., Herries, A.I.R., Brown, K., Williams, H.M., Bernatchez, J., Ayalon, A., Nilssen, P.J., 2010, A high resolution and continuous isotopic speleothem record of paleoclimate and paleoenvironment from 90 to 53 ka from Pinnacle Point on the south coast of South Africa: *Quaternary Science Reviews*, v. 29, 2131-2145.
- Berner, R.A., 1975, The role of magnesium in the crystal growth of calcite and aragonite from sea water: *Geochemica et Cosmochimica Acta*, v. 39, 489-504.
- Brook, G.A., 1982, Stratigraphic evidence of quaternary climatic change at Echo Cave, Transvaal, and paleoclimatic record for Botswana and northeastern South Africa: *Catena*, v. 9, 343-351.
- Brook, G.A., Burney, D.A., Coward, J.B., 1990, Desert paleoenvironmental data from cave speleothems with examples from the Chihuahuan, Somli-Chalbi, and Kalahari deserts: *Palaeogeography, Palaeoclimatology, Palaeoecology*, v. 76, 311-329.
- Brook, G.A., 1999, Arid zone paleoenvironmental records from Cave Speleothems. In: Singhvi, A.K., Derbyshire, E. (Eds.), *Paleoenvironmental Reconstruction in Arid Lands*, Oxford & IBH, New Delhi, 217-262.
- Brook, G.A., Ellwood, B.B., Railsback, L.B., Cowart, J.B., 2006, A 164 ka record of environmental change in the American Southwest from a Carlsbad Cavern speleothem: *Palaeogeography, Palaeoclimatology, Palaeoecology*, v. 237, 483-507.

Brook, G.A., Marais, E., Srivastava, P., Jordan, T., 2007, Timing of lake-level changes in Etosha Pan, Namibia, since the middle Holocene from OSL ages of relict shorelines in the Okondeka region: *Quaternary International*, v. 175, 29-40.

Brook, G.A., Scott, L., Railsback, L.B., Goddard, E.A., 2010, A 35 ka pollen and isotope record of environmental change along the southern margin of the Kalahari from stalagmite and animal dung deposits in Wonderwerk Cave, South Africa: *Journal of Arid Environments*, 1-15.

Brook, G.A., Railsback, L.B., Marais, E., 2011, Reassessment of carbonate ages by dating both carbonate and organic material from an Etosha Pan (Namibia) stromatolite: Evidence of humid phases during the last 20 ka: *Quaternary International*, v. 229, 24-37.

Burton E. A., Walter L. M., 1987, Relative precipitation rates of aragonite and Mg calcite from seawater: temperature or carbonate ion control?: *Geology*, v. 15, 111–114.

Cabrol, P., 1978, Contribution à l'étude du concrétionnement carbonaté des grottes du sud de la France, morphologie, genèse et diagenèse: *Centre d'Etudes et de Recherches Géologiques et Hydrogéologiques, Mémoires, Montpellier, France*, v. 12, 275.

Cerling, T.E., 1999, Stable carbon isotopes in palaeosol carbonates: *Special Publications int. Ass. Sediment*, v. 27, 43-60.

Chase, B., 2009, Evaluating the use of dune sediments as a proxy for palaeo-aridity: a southern African case study: *Earth Science Reviews*, v. 93, 31-45.

Chase, B.M., Meadows, M.E., Scott, L., Thomas, D.S.G., Marais, E., Sealy, J., and Reimer, P.J., 2009, A record of rapid Holocene climate change preserved in hyrax middens from southwestern Africa: *Geological Society of America*, v. 37, no. 8, 703-706.

Chase, B.M., Meadows, M.E., Carr, A.S., Reimer, P.J., 2010, Evidence for progressive Holocene aridification in southern Africa recorded in Namibian hyrax middens: Implications for African Monsoon dynamics and the "African Humid Period", *Quaternary Research*, v. 74, 36-45.

Cheng, H., Edwards, R.L., Hoff, J., Gallup, C.D., Richards, D.A., and Asmerom, Y., 2000, The half-lives of uranium-234 and thorium-230: *Chemical Geology*, v. 169, 17-33.

Clark, I., Fritz, P., 1997, *Environmental isotopes in hydrology*: Lewis Publishers, New York.

Craig, H., 1965, The measurement of oxygen isotope paleotemperatures. In: Tongiorgi, E. (Ed.), *Stable Isotopes in Oceanographic Studies and Paleotemperatures*. Consiglio Nazionale delle Ricerche Laboratorio di Geologia Nucleare, Pisa, 166-182.

Craig, H., Gordon, L.I., 1965, Deuterium and oxygen 18 variations in the ocean and the marine atmosphere. In: Tongiorgi, E. (Ed.), *Stable Isotopes in Oceanographic Studies and Paleotemperatures*. Consiglio Nazionale delle Ricerche Laboratoria di Geologia Nucleare – Pisa, Spoleto, 9–130.

Dansgaard, W., 1964, Stable isotopes in precipitation: *Tellus*, v. 16, 436-468.

Debajyoti P., Skrzypek G., 2007, Assessment of carbonate-phosphoric acid analytical technique performed using GasBench II in continuous flow isotope ratio mass spectrometry: *Int. J. Mass Spec.*, v. 262, 180-186.

Dreybrodt, W. 1988, Processes in karst systems: physics, chemistry and geology: Springer Series in Physical Environment, v. 4: Springer, Berlin/Heidelberg/New York.

Dreybrodt, W., Scholz, D., 2010, Climatic dependence of stable carbon and oxygen isotope signals recorded in speleothems: From soil water to speleothem calcite: *Geochimica et Cosmochimica Acta*, v. 75, 734-752.

Edwards, R.L., Chen, J.H., Wasserburg, G.J., 1988, ^{238}U - ^{234}U - ^{230}Th systematics and precise measurement of time over the last 500,000 years: *Earth Planet. Sci. Lett.*, v. 81, 175-192.

Fairchild, I.J., Borsato, A., Tooth, A., Frisia, S., Hawkesworth, C.J., Huang, Y., McDermott, F., Spiro, B., 2000, Controls on trace element (Sr-Mg) compositions of carbonate cave water: Implications for speleothem climate records, *Chem. Geol.*, v. 166, 255-269.

Finch, A.A., Shaw, P.A., Holmgren, K., Lee-Thorp, J., 2003, Corroborated rainfall records from aragonitic stalagmites: *Earth and Planetary Science Letters*, v. 215, 265-273.

Folk, R.L., 1974, The natural history of crystalline calcium carbonate: effect of magnesium content and salinity: *Journal of Sedimentary Petrology*, v. 44, 40-53.

Ford, D., 1997, Dating and Paleo-Environmental Studies of Speleothems: Cave Minerals of the World. 2nd Ed. Hill, C. and Forti, P, editors, National Speleological Society. Huntsville, Alabama.

Fox, D.L., Koch, P.L., 2003, Tertiary history of C4 biomass in the Great Plains, USA: *Geology*, v. 31, 809-12.

Frisia, S., Borsato, A., Fairchild, I.F., McDermott, F., 2000, Calcite fabrics, growth mechanisms, and environments of formation in speleothems from the Italian Alps and southwestern Ireland: *Journal of Sedimentary Research*, v. 70, no. 5, 1183-1196.

Frisia, S., Borsato, A., Fairchild, I.J., McDermott, F., Selmo, E.M., 2002, Argonite-calcite relationships in speleothems (Grotte de Clamouse, France): environment, fabrics, and carbonate geochemistry: *Journal of Sedimentary Research*, v. 72, no. 5, 687-699.

Gat, J.R., 1996, Oxygen and hydrogen isotopes in the hydrologic cycle: *Annual Review of Earth and Planetary Sciences*, v. 24, 225-262.

Gil-Romero, G., Scott, L., Marias, E., Brook, G.A., 2006, Middle- to late- Holocene moisture changes in the desert of northwest Namibia, derived from fossil hyrax dung pollen: *The Holocene*, v. 16, 1073-1084.

Gil-Romero, G., Scott, L., Marais, E., Brook, G., 2007, Late Holocene environmental change in the northwestern Namib Desert margin: New fossil pollen evidence from hyrax middens: *Palaeogeography, Palaeoclimatology, Paeoecology*, v. 249, 1-17.

Given, R.K., Wilkinson, B.H., 1985, Kinetic control of morphology, composition, and mineralogy of abiotic sedimentary carbonates: *Journal of Sedimentary Petrology*, v. 55, 109-119.

Gonzalez L.A. & Lohmann K.C., 1987, Controls on mineralogy and composition of spelean carbonates: Carlsbad Cavern, New Mexico. In: James N.P. & Choquette P.W. (Ed.): *Paleokarst*, Springer-Veriag, 81-101.

Gonzalez, L.A., Carpenter, S.J., Lohmann, K.C., 1992, Inorganic calcite morphology: roles of fluid chemistry and fluid flow: *Journal of Sedimentary Petrology*, v. 62, no. 3, 382-399.

Harmon, R.S., Atkinson, T.C., Atkinson, J.L., 1983, The mineralogy of Castleguard Cave, Columbia Icefields, Alberta Canada: *Arctic and Alpine Research*, v. 15, 503-516.

Heine, K., 2005, Holocene climate of Namibia: A review based on geoarchives: *African Study Monographs*, suppl. 30, 119-133.

Hendy, C.H., 1971, The isotopic geochemistry of speleothem I: the calculation of the effects of different modes of formation on the isotopic composition of speleothems and their applicability as palaeoclimatic indicators, *Geochimica et Cosmochimica Acta*, v. 35, 801-824.

Hodell, D.A., Curtis, J.H., Jones, G.A., Higuera-Gundy, A., Brenner, M., Binford, M.W., Dorsey, K.T., 1991, Reconstruction of Caribbean climate change over the past 10,500 year: *Nature*, v. 352, 790-793.

Hodell, D.A., Brenner, M., Curtis, J.H., Guilderson, T., 2001, Solar forcing of drought frequency on the Maya Lowlands: *Science*, v. 292, 1367-1370.

Holmgren, K., Karlen, W., Shaw, P., 1995, Paleoclimatic significance of the stable isotopic composition and petrology of a late Pleistocene stalagmite from Botswana: *Quaternary Research*, v. 43, 320-328.

Holmgren, K., Karlen, W., Lauritzen, S.E., Lee-Thorp, J.A., Partridge, T.C., Piketh, S., Repinski, P., Stevenson, C., Svanered, O., Tyson, P.D., 1999, A 3000-year high-resolution stalagmite-based record of palaeoclimate for northeastern South Africa: *The Holocene*, v. 9, no. 3, 295-309.

Holmgren, K., Lee-Thorp, J.A., Cooper, G.R.J., Lundblad, K., Partridge, T.C., Scott, L., Sithaldeen, R., Siep Talmaf, A., Tyson, P.D., 2003, Persistent millennial-scale climatic variability over the past 25,000 years in Southern Africa: *Quaternary Science Reviews*, v. 22, is. 21-22, 2311-2326.

Holzkämper, S., Holmgren, K., Lee-Thorp, J., Talma, S., Mangini, A., Partridge, T., 2009, Late Pleistocene stalagmite growth in Wolkberg Cave, South Africa, *Earth and Planetary Science Letters*, v. 282, 212-221.

Irish, J., Marais, E., Juberthie, C. and Decu, V., 2001, Namibia. *Encyclopedia Biospeologica*, 1639-1650.

Johnsen, S.J., Dahl-Jensen, D., Gundestrup, N., Steffensen, J.P., Clausen, H.B., Miller, H., Masson-Delmotte, V., Sveinbjörnsdóttir, A.E., White, J., 2001, Oxygen isotope and palaeotemperature records from six Greenland ice-core stations: Camp Century, Dye3, GRIP, GISP2, Renland and NorthGRIP: *Journal of Quaternary Science*, v. 16, 299-307.

Kim, S. T., O'Neil, J. R., 1997, Equilibrium and non-equilibrium oxygen isotope effects synthetic carbonates: *Geochimica et Cosmochimica Acta*, v. 61, 3461-3475.

Kottek, M., J. Grieser, C. Beck, B. Rudolf, and F. Rubel, 2006, World Map of the Köppen-Geiger climate classification updated, (Ed.) *Meteorol. Z.*, v. 15, 259-263.

Lachinet, M.S., 2009, Climate and environmental controls on speleothem oxygen-isotope values: *Quaternary Science Reviews*, v. 28, 412-432.

- Lahann, R.W., 1978, A chemical model for calcite crystal growth and morphology control: *Journal of Sedimentary Petrology*, v. 48, 337-344.
- Lebron, I., and Suarez, D.L., 1996, Calcite nucleation and precipitation kinetics as affected by dissolved organic matter at 25°C and pH>7.5: *Geochimica et Cosmochimica Acta*, v. 60, 2765-2776.
- Maslin, M. A., Christensen, B., 2007, Tectonics, orbital forcing, global climate change, and human evolution in Africa: introduction to the African paleoclimate special volume: *Journal of Human Evolution* v. 53, 443-464.
- Mayewski, P.A., Rohlings, E.E., Stager, J.C., Karlen, W., Maasch, K.A., Holmgren, K., Lee-Thorp, J., Rosqvist, G., Rack, F., Staubwasser, M., Schneider, R., Steig, E.J., 2004, Holocene climate variability: *Quaternary Research*, v. 62, 243-255.
- McCrea, J.M., 1950, The isotopic geochemistry of carbonates and a paleotemperature scale: *Journal of Chemistry and Physics*, v. 18, 849-857.
- McDermott, F., 2004, Paleo-climate reconstruction from stable isotope variations in speleothems: a review: *Quaternary Science Reviews*, v. 23, 901-918.
- McDermott, F., Schwarcz, H., Rowe, P.J., 2005, Isotopes in speleothems, (Ed.) Leng, M.J., *Isotopes in Palaeoenvironmental Research*, v. 10, 185-225, Springer, Netherlands.
- McDonald J., Dyrsdale, R., Hill, D., 2004, The 2002-2003 El Nino recorded in Australian cave drip waters: implications for reconstructing rainfall histories using stalagmites: *Geophysical Research Letterse*, v. 31, L22202.
- Mendelsohn, J., Jarvis, A., Roberts, C., Robertson, T., 2002, *Atlas of Namibia*. David Philip, Cape Town.
- Meyer, H.J., 1984, The influence of impurities on the growth rate of calcite: *Journal Crystal Growth*, v. 66, 646.
- Mickler, P.J., Stern, L., Banner, J.L., 2006, Large kinetic isotope effects in modern speleothems: *Geological Society of America Bulletin*, v. 118, 65-81.
- Miller, R.McG., 1983, The Pan-African Damara Orogen of South West Africa, evolution of the Damara Orogen of South West Africa/Namibia, (Ed.) Miller, R.McG.,:Special publication of the Geological Society of South, Pretoria, v. 11, 431-515.
- Miller, R. McG., 1997, Chapter 11 The Owambo basin of northern Namibia: *Sedimentary Basins of the World*, v. 3, 237-268.
- Mühlinghause, C., Scholz, D., Mangini, A., 2009, Modelling fractionation of stable isotopes in stalagmites: *Geochimica et Cosmochimica Acta*, v. 73, 7275-7289.
- Penman, H.L., 1948, Natural evaporation from open water, bare soil and grass: *Proceedings of the Royal Meteorological Society (series A)*, v. 193, 120-146.
- Preston-Whyte, R.A., Tyson, P.D., 1988, *The atmosphere and weather of southern Africa*: Oxford University Press, Cape Town.

Railsback, L.B., Brook, G.A., Chen, J., Kalin, R., and Fleisher, C. J., 1994, Environmental controls on the petrology of a late Holocene speleothem from Botswana with annual layers of aragonite and calcite: *Journal of Sedimentary Research*, v. 64, no. 1, 147-155.

Railsback, L.B., 2010, Some Fundamentals of Mineralogy and Geochemistry, <http://www.gly.uga.edu/railsback/Fundamentals/1121KarstSpeleoPptn03.jpg>.

Railsback, L.B., Liang, F., Romani, J.V., d'Anglade, A.G., Rodríguez, M.V., Fidalgo, L.S., Mosquera, D.F., Cheng, H., Edwards, R.L., 2011 (in press), Petrographic and isotopic evidence for Holocene long-term climate change and shorter-term environmental shifts from a stalagmite from the Serra do Courel of northwestern Spain, and implications for climatic history across Europe and the Mediterranean: *Palaeogeography, Palaeoclimatology, Palaeoecology*.

Repinski, P., Holmgren, K., Lauritzen, S.E., Lee-Thorp, J.A., 1999, A late Holocene climate record from a stalagmite, Cold Air Cave, Northern Province, South Africa: *Palaeogeography, Palaeoclimatology, Palaeoecology*, v. 150, is. 3-4, 269-277.

Romanek, C.S., Grossman, E.L., and Morse, J.W., 1992, Carbon isotopic fractionation in synthetic aragonite and calcite: Effects of temperature and precipitation rate: *Geochimica et Cosmochimica Acta*, v. 56, 419-430.

Romanov, D., Kaufmann, G., Dreybrodt, W., 2008, Modeling stalagmite growth by first principles of chemistry and physics of calcite precipitation: *Geochimica et Cosmochimica Acta*, v. 72, 423-437.

Rozanski, K., Araguas-Araguas, L., Gonfiantini, R., 1993, Isotopic patterns in modern global precipitation, In: Swart, P.K., Lohmann, K.L., McKenzie, J., Savin S. (Eds.), *Climate Change in Continental Records*: American Geophysical Union, Washington, DC, 1-37.

Scott, L., Cooremans, B., de Wet, J.S., Vogel, J.C., 1991, Holocene environmental changes in Namibia inferred from pollen analysis of swamp and lake deposits: *The Holocene*, v. 1, 8-13.

Shen, C.C., Edwards, R.L., Cheng, H., Dorale, J.A., Thomas, R.B., Moran, S.B., Weinstein, S.E., and Edmonds, H.N., 2002, Uranium and thorium isotopic and concentration measurements by magnetic sector inductively coupled plasma mass spectrometry: *Chemical Geology*, v. 185, 165-178.

Shopov, Y.Y., 1997, *Luminescence of Cave Minerals: Cave Minerals of the World*. 2nd Ed. Hill, C. and Forti, P, editors, National Speleological Society. Huntsville, Alabama.

Shopov, Y.Y., 2006, Speleothem paleoluminescence – The past twenty years, *GSA Special Papers*, v. 404, 319-330.

Sonzogni, C., Bard, E., Rostek, F., 1998, Tropical sea-surface temperatures during the last glacial period: a view based on alkenones in Indian Ocean sediments: *Quaternary Science Reviews*, v. 17, 1185–1201.

Talma, A.S., Vogel, J.C., Partridge, T.C., 1974, Isotopic contents of some Transvaal speleothems and their palaeoclimatic significance: *South African Journal of Science*, v. 70, 135-140.

Talma, A.S., Vogel, J.C., 1992, Late Quaternary paleotemperature derived from a speleothem from Cango Cave, Cape Province, South Africa: *Quaternary Research*, v. 37, 203-213.

Tarashtan, A.N., 1978, Luminescence of minerals: Kiev, Naukova Dumka, 296. In Russian.

Treble, P.C., Chappell, J., Shelley, J.M., 2005, Complex speleothem growth processes revealed by trace element mapping and scanning electron microscopy of annual layers: *Geochimica et Cosmochimica Acta*, v. 69, 4855-4863.

Tyson, P.D., 1986, *Climatic change and variability in southern Africa*: Oxford University Press, Cape Town.

Tyson, P.D., Karlen, W., Holmgren, K., Heiss, G.A., 2000, The Little Ice Age and medieval warming in southern Africa: *South African Journal of Science*, v. 96, 121-126.

van Beynen, P.E., Soto, L., Pace-Craczyk, K., 2008, Paleoclimate reconstruction derived from speleothem strontium and $\delta^{13}\text{C}$ in Central Florida: *Quaternary International*, v. 187, 76-83.

Walter, L.M., 1986, Relative efficiency of carbonate dissolution and precipitation during diagenesis: a progress report on the role of solution chemistry, in Gautier, D.L., ed., *Roles of Organic Matter in Sediment Diagenesis*: Soc. Econ. Pal. Min. Special Publication, v. 38, 1-11.

APPENDIX A

DP1 SAMPLE, STABLE ISOTOPE, AND FABRIC DATA

UA Sample	UGA Sample	Position (mm)	$\delta^{13}\text{C}$	$\delta^{18}\text{O}$	Transformed	Transformed	^{230}Th	Calculated	Thin	Mineralogy	Fabric
ID	ID	from top)	VPDB	VPDB	$\delta^{13}\text{C}$ VPDB	$\delta^{18}\text{O}$ VPDB	Dates (BP)	Dates (BP)	Section #		ID
	DP1-T	2					14	14			
	DP1-5	5	-6.6	-8.1	-8.3	-8.9		18	1	Aragonite	IA
	DP1-ISO-6	6	-7.2	-8.5	-8.9	-9.3		19	1	Aragonite	MBNA
	DP1-10	10	-7.4	-8.4	-9.1	-9.2		24	1	Aragonite	IA
	DP1-ISO-11	11	-7.7	-8.7	-9.4	-9.5		25	1	Aragonite	IA
	DP1-15	15	-7.8	-8.6	-9.5	-9.4		31	1	Aragonite	MNA
	DP1-ISO-20	21	-7.0	-8.2	-8.7	-9.0		38	1	Aragonite	MNA
	DP1-25	25	-7.2	-8.4	-7.2	-8.4		43	1	Calcite	CC
	DP1-ISO-25	26	-9.4	-9.2	-9.4	-9.2		45	1	Calcite	CC
	DP1-30	30	-7.3	-8.5	-7.3	-8.5		50	1	Calcite	CC
	DP1-ISO-32	34	-9.7	-9.5	-9.7	-9.5		55	1	Calcite	CC
	DP1-35	35	-8.8	-9.5	-10.5	-10.3		56	1	Aragonite	IA
	DP1-ISO-40	41	-8.2	-9.4	-9.9	-10.2		64	1	Aragonite	MNA
	DP1-45	45	-6.9	-8.8	-8.6	-9.6		69	1	Aragonite	MNA
	DP1-ISO-48	49	-6.3	-8.4	-8.0	-9.2		74	1	Aragonite	MNA
	DP1-50A	50	-6.9	-8.9	-8.6	-9.7		75	1	Aragonite	MNA
	DP1-ISO-55	55	-7.5	-9.3	-9.2	-10.1		82	1	Aragonite	MNA
	DP1-60	60	-7.3	-9.6	-7.3	-9.6		88	1	Calcite	CC
	DP1-ISO-64	64	-9.5	-10.6	-9.5	-10.6		93	1	Calcite	CC
	DP1-65	65	-7.8	-10.0	-7.8	-10.0		94		Calcite	
	DP1-ISO-69	69	-9.7	-10.6	-9.7	-10.6		100	2	Calcite	CC
	DP1-70	70	-7.9	-10.1	-9.6	-10.9		101	2	Aragonite	MNA
	DP1-75	75	-6.6	-8.9	-8.3	-9.7		107	2	Aragonite	MNA
	DP1-ISO-76	76	-6.9	-9.2	-8.6	-10.0		109	2	Aragonite	MNA
	DP1-80	80	-7.2	-10.0	-8.9	-10.8		114	2	Aragonite	MNA
	DP1-ISO-85	85	-7.4	-9.8	-9.1	-10.6		120	2	Aragonite	MBNA
	DP1-90	90	-9.2	-10.6	-10.9	-11.4		126	2	Aragonite	CC
	DP1-ISO-95	95	-9.9	-10.7	-9.9	-10.7		133	2	Calcite	CC
	DP1-100	100	-10.2	-10.8	-10.2	-10.8		139	2	Calcite	CC
	DP1-ISO-101	101	-9.9	-10.7	-9.9	-10.7		140	2	Calcite	CC
	DP1-103	103					143	143			
	DP1-ISO-109	109	-6.8	-9.5	-8.5	-10.3		153		Aragonite	
	DP1-ISO-116	116	-7.1	-9.6	-8.8	-10.4		164	3	Aragonite	MBNA
	DP1-120	120	-9.8	-11.4	-9.8	-11.4		170	3	Calcite	CC
	DP1-ISO-122	121	-9.2	-11.0	-9.2	-11.0		172	3	Calcite	CC
	DP1-125	125	-9.4	-11.0	-9.4	-11.0		178	3	Calcite	CC
	DP1-130	130	-10.0	-11.4	-10.0	-11.4		186	3	Calcite	CC
	DP1-ISO-132	131	-9.7	-11.2	-9.7	-11.2		188	3	Calcite	CC
	DP1-135	135	-10.3	-11.6	-10.3	-11.6		194	3	Calcite	CC
	DP1-140	140	-9.7	-11.2	-9.7	-11.2		202	3	Calcite	CC
	DP1-ISO-143	143	-7.9	-9.7	-9.6	-10.5		207	3	Aragonite	MBNA
	DP1-145	145	-9.6	-10.4	-9.6	-10.4		210	3	Calcite	IA
	DP1-ISO-146	146	-7.3	-9.5	-7.3	-9.5		212	3	Calcite	CC
	DP1-150	150	-9.9	-10.5	-9.9	-10.5		218	3	Calcite	CC
	DP1-ISO-155	155	-9.3	-10.3	-11.0	-11.1		226	4	Aragonite	MBNA
	DP1-160	160	-9.7	-10.3	-9.7	-10.3		234	4	Calcite	CC
	DP1-ISO-161	161	-9.5	-10.4	-9.5	-10.4		236	4	Calcite	CC
	DP1-165	165	-7.7	-9.6	-9.4	-10.4		242	4	Aragonite	MNA
DP1-UAL-168	DP1-ISO-168	168	-5.9	-8.5	-7.6	-9.3		247	4	Aragonite	MNA
	DP1-170	170	-7.2	-9.2	-8.9	-10.0		250	4	Aragonite	MNA
	DP1-175	175						258	4		
	DP1-ISO-180	180	-9.6	-10.1	-9.6	-10.1		267	4	Calcite	CC
	DP1-ISO-185	185	-10.0	-10.2	-10.0	-10.2		275	4	Calcite	CC
	DP1-190	190						283			
	DP1-ISO-191	192	-7.2	-9.1	-7.2	-9.1		286		Aragonite	
	DP1-195	195	-6.2	-9.5	-6.2	-9.5		291		Aragonite	
	DP1-200	200	-6.6	-9.7	-6.6	-9.7		299		Aragonite	
	DP1-ISO-203	204	NA	NA				305			
	DP1-ISO-209	210	-9.4	-10.8	-9.4	-10.8		315	6	Calcite	CC
	DP1-ISO-217	218	-9.2	-10.6	-9.2	-10.6		327	6	Calcite	CC
	DP1-ISO-229	230	-10.0	-10.8	-10.0	-10.8		347	6	Calcite	CC

UA Sample	UGA Sample	Position (mm)	$\delta^{13}\text{C}$	$\delta^{18}\text{O}$	Transformed	Transformed	^{230}Th	Calculated	Thin	Mineralogy	Fabric
ID	ID	from top)	VPDB	VPDB	$\delta^{13}\text{C}$ VPDB	$\delta^{18}\text{O}$ VPDB	Dates (BP)	Dates (BP)	Section #		ID
	DP1-ISO-235	236	-8.0	-9.9	-9.7	-10.7		356	6	Aragonite	MBNA
	DP1-ISO-240	241	-5.5	-7.5	-7.2	-8.3		364	6	Aragonite	MBNA
	DP1-ISO-245	246	-5.6	-7.4	-7.3	-8.2		372	6	Aragonite	NA
	DP1-ISO-250	252	-7.0	-9.1	-8.7	-9.9	382	382		Aragonite	
	DP1-ISO-261	263	-6.0	-8.2	-7.7	-9.0		437	7	Aragonite	NA
	DP1-ISO-266	268	-5.2	-7.3	-6.9	-8.1		462	7	Aragonite	MNA
	DP1-ISO-272	275	-6.6	-8.1	-8.3	-8.9		496	7	Aragonite	MBNA
	DP1-ISO-276	278	-6.9	-8.5	-8.6	-9.3		511	7	Aragonite	MNA
	DP1-ISO-280	283	-6.1	-7.1	-7.8	-7.9		536	7	Aragonite	MNA
	DP1-ISO-285	288	-7.1	-7.6	-8.8	-8.4		561	7	Aragonite	MNA
	DP1-ISO-290	293	-6.5	-7.2	-8.2	-8.0		586	7	Aragonite	MNA
	DP1-ISO-295	298	-10.1	-9.0	-10.1	-9.0		611	7	Calcite	CC
	DP1-ISO-299	302	-9.4	-9.2	-9.4	-9.2		630	7	Calcite	CC
	DP1-ISO-306	308	-10.4	-10.3	-10.4	-10.3		660	7	Calcite	CC
	DP1-ISO-314	316	-7.2	-8.6	-7.2	-8.6		700	7	Calcite	CC
	DP1-315	316					700	700			
	DP1-ISO-321	323	-8.1	-8.4	-8.1	-8.4		706		Calcite	CC
DP1-UAL-325	DP1-ISO-325	328	-9.6	-9.6	-9.6	-9.6		710	8	Calcite	CC
	DP1-ISO-330	333	-9.6	-9.7	-9.6	-9.7		714	8	Calcite	CC
DP1-UAL-335	DP1-ISO-335	338	-6.5	-8.6	-8.2	-9.4		719	8	Aragonite	MBNA
	DP1-ISO-340	343	-9.9	-10.1	-9.9	-10.1		723	8	Calcite	CC
	DP1-ISO-345	348	-6.4	-8.8	-8.1	-9.6		727	8	Aragonite	IA
DP1-UAL-349	DP1-ISO-349	352	-7.0	-9.2	-8.7	-10.0		730	8	Aragonite	IA
DP1-UAL-355	DP1-ISO-355	357	-9.4	-10.2	-9.4	-10.2		734	8	Calcite	CC
	DP1-ISO-360	363	-9.7	-10.2	-9.7	-10.2		740	8	Calcite	CC
	DP1-ISO-365	367	-9.7	-10.2	-9.7	-10.2		743	8	Calcite	CC
	DP1-ISO-370	372	-10.4	-10.3	-10.4	-10.3		747	8	Calcite	CC
	DP1-ISO-375	377	-9.4	-9.1	-9.4	-9.1		751	8	Calcite	CC
	DP1-ISO-380	382	-10.3	-9.4	-10.3	-9.4		756	9	Calcite	CC
	DP1-ISO-384	387	-9.2	-8.6	-9.2	-8.6		760	9	Calcite	CC
	DP1-ISO-388	391	-10.0	-8.9	-10.0	-8.9		763	9	Calcite	CC
DP1-UAL-393	DP1-ISO-393	394	-8.8	-9.4	-8.8	-9.4		766	9	Calcite	CC
	DP1-ISO-398	399	-9.4	-10.0	-9.4	-10.0		770	9	Calcite	CC
	DP1-ISO-408	409	-9.5	-10.2	-9.5	-10.2		778	9	Calcite	CC
	DP1-ISO-418	418	-9.4	-10.5	-9.4	-10.5		786	9	Calcite	CC
	DP1-ISO-427	427	-9.4	-10.6	-9.4	-10.6		793	9	Calcite	CC
	DP1-ISO-431	431	-6.9	-9.5	-8.6	-10.3		797	9	Aragonite	NA
	DP1-ISO-436	435	-6.8	-9.2	-8.5	-10.0		800	9	Aragonite	NA
	DP1-ISO-441	440	-7.2	-9.1	-8.9	-9.9		804		Aragonite	
	DP1-ISO-446	445	-6.5	-9.0	-8.2	-9.8		808	10	Aragonite	NA
	DP1-448	448					811	811			
	DP1-ISO-451	450	-5.8	-8.8	-7.5	-9.6		817	10	Aragonite	NA
	DP1-ISO-456	458	-5.8	-8.7	-7.5	-9.5		841	10	Aragonite	NA
	DP1-ISO-461	464	-6.1	-8.5	-7.8	-9.3		859	10	Aragonite	MNA
	DP1-ISO-471	474	-5.7	-8.0	-7.4	-8.8		889	10	Aragonite	NA
	DP1-ISO-476	479	-5.6	-8.2	-7.3	-9.0		904	10	Aragonite	MNA
	DP1-ISO-481	484	-6.1	-8.6	-7.8	-9.4		919	10	Aragonite	MNA
	DP1-ISO-490	493	-7.0	-9.0	-8.7	-9.8		946	10	Aragonite	MNA
	DP1-ISO-495	497	-5.7	-7.7	-7.4	-8.5		958	10	Aragonite	NA
DP1-UAL-500	DP1-ISO-500	502	-6.5	-7.7	-8.2	-8.5		972		Aragonite	
	DP1-ISO-505	506	-6.1	-8.1	-7.8	-8.9		984	11	Aragonite	MNA
	DP1-ISO-509	511	-7.0	-8.6	-8.7	-9.4		999	11	Aragonite	MNA
	DP1-ISO-515	516	-6.3	-8.0	-8.0	-8.8		1014	11	Aragonite	MNA
	DP1-ISO-520	520	-6.4	-8.5	-8.1	-9.3		1026	11	Aragonite	MNA
	DP1-ISO-524	525	-6.2	-7.8	-7.9	-8.6		1041	11	Aragonite	MNA
DP1-UAL-529	DP1-ISO-529	530	-6.0	-8.0	-7.7	-8.8		1056	11	Aragonite	MNA
DP1-UAL-535	DP1-ISO-535	535	-6.3	-8.0	-8.0	-8.8		1071	11	Aragonite	MNA
	DP1-ISO-541	540	-6.4	-8.0	-8.1	-8.8		1086	11	Aragonite	MNA
DP1-UAL-546	DP1-ISO-546	549	-5.7	-7.8	-7.4	-8.6		1113	11	Aragonite	MBNA
	DP1-550	551					1119	1119			
	DP1-ISO-554	554	-9.2	-9.8	-9.2	-9.8		1124	11	Calcite	CC

UA Sample	UGA Sample	Position (mm)	$\delta^{13}\text{C}$	$\delta^{18}\text{O}$	Transformed	Transformed	^{230}Th	Calculated	Thin	Mineralogy	Fabric
ID	ID	from top	VPDB	VPDB	$\delta^{13}\text{C}$ VPDB	$\delta^{18}\text{O}$ VPDB	Dates (BP)	Dates (BP)	Section #		ID
	DP1-ISO-559	559	-9.2	-9.6	-9.2	-9.6		1131	11	Calcite	CC
	DP1-ISO-564	564	-9.6	-9.9	-9.6	-9.9		1139	11	Calcite	CC
	DP1-ISO-568	568	-6.5	-9.1	-8.2	-9.9		1145	11	Aragonite	MNA
	DP1-570	570					1148	1148			
	DP1-ISO-575	574	-8.5	-10.2	-8.5	-10.2		1153	12	Calcite	CC
	DP1-ISO-586	585	-9.0	-10.5	-9.0	-10.5		1168	12	Calcite	CC
	DP1-ISO-591	590	-9.4	-10.6	-9.4	-10.6		1175	12	Calcite	CC
	DP1-ISO-597	596	-9.4	-10.6	-9.4	-10.6		1183	12	Calcite	CC
	DP1-ISO-602	601	-6.4	-8.9	-8.1	-9.7		1189	12	Aragonite	MBNA
	DP1-ISO-611	609	-9.6	-10.1	-9.6	-10.1		1200	12	Calcite	CC
	DP1-ISO-615	613	-6.1	-8.7	-7.8	-9.5		1205	13	Aragonite	MNA
	DP1-ISO-621	619	-6.7	-8.4	-8.4	-9.2		1213	13	Aragonite	MNA
	DP1-ISO-631	629	-9.6	-9.2	-9.6	-9.2		1227	13	Calcite	CC
	DP1-ISO-636	634	-9.4	-9.3	-9.4	-9.3		1233	13	Calcite	CC
	DP1-ISO-641	638	-9.3	-10.3	-9.3	-10.3		1239	13	Calcite	CC
DP1-UAL-646	DP1-ISO-646	644	-9.5	-11.1	-9.5	-11.1		1247	13	Calcite	CC
	DP1-ISO-652	650	-9.9	-11.3	-9.9	-11.3		1255	13	Calcite	CC
	DP1-ISO-657	655	-9.3	-11.5	-9.3	-11.5		1261	13	Calcite	CC
	DP1-ISO-661	659	-6.3	-9.5	-8.0	-10.3		1267	13	Aragonite	MNA
	DP1-ISO-667	665	-6.9	-9.4	-8.6	-10.2		1275	13	Aragonite	MNA
	DP1-ISO-673	671	-8.7	-10.3	-8.7	-10.3		1283	13	Calcite	CC
	DP1-671	672					1284	1284			
	DP1-ISO-678	676	-6.0	-8.4	-7.7	-9.2		1284	13	Aragonite	IA
	DP1-ISO-684	682	-5.6	-7.8	-7.3	-8.6		1284		Aragonite	
	DP1-ISO-689	685	-9.5	-9.6	-9.5	-9.6		1285	14	Calcite	CC
	DP1-ISO-694	690	-6.5	-8.3	-8.2	-9.1		1285	14	Aragonite	MBNA
	DP1-690	693					1285	1285			
	DP1-ISO-699	695	-5.5	-8.9	-7.2	-9.7		1291	14	Aragonite	NA
	DP1-ISO-703	700						1307			
	DP1-ISO-713	710	-5.5	-8.1	-7.2	-8.9		1338	14	Aragonite	NA
	DP1-ISO-718	715	-5.7	-8.7	-7.4	-9.5		1354	14	Aragonite	MNA
	DP1-709	717					1360	1360			
	DP1-ISO-723	720	-5.8	-8.7	-7.5	-9.5		1366	14	Aragonite	MNA
	DP1-ISO-728	724	-6.3	-9.0	-8.0	-9.8		1375	15	Aragonite	MNA
	DP1-ISO-734	730	-6.9	-9.0	-8.6	-9.8		1388	15	Aragonite	MNA
	DP1-ISO-740	736	-6.0	-8.5	-7.7	-9.3		1401	15	Aragonite	MNA
	DP1-ISO-745	741	-7.7	-9.4	-7.7	-9.4		1411	15		MNA
	DP1-ISO-751	746	-7.4	-10.0	-9.1	-10.8		1422	15	Aragonite	MNA
	DP1-ISO-756	751	-6.1	-9.7	-7.8	-10.5		1433	15	Aragonite	MNA
	DP1-ISO-761	756	-5.8	-9.4	-7.5	-10.2		1443	15	Aragonite	NA
	DP1-ISO-770	765	-6.3	-8.7	-8.0	-9.5		1463	15	Aragonite	MNA
	DP1-ISO-775	770	-6.3	-10.0	-8.0	-10.8		1473	15	Aragonite	MNA
	DP1-775	775					1484	1484			
	DP1-ISO-783	778	-7.0	-9.7	-8.7	-10.5		1491	15	Aragonite	IA
	DP1-ISO-797	784	-6.0	-8.5	-7.7	-9.3		1506	15	Aragonite	NA
	DP1-ISO-802	788	-4.6	-8.1	-6.3	-8.9		1516	15	Aragonite	CA
	DP1-ISO-809	795	-7.3	-10.4	-9.0	-11.2		1534	16	Aragonite	MNA
	DP1-ISO-814	800	-7.0	-10.1	-8.7	-10.9		1546	16	Aragonite	MNA
	DP1-ISO-819	805	-7.0	-10.2	-8.7	-11.0		1559	16	Aragonite	MNA
	DP1-ISO-825	811	-7.1	-10.0	-8.8	-10.8		1574	16	Aragonite	IA
	DP1-ISO-830	816	-6.7	-9.4	-8.4	-10.2		1586	16	Aragonite	NA
	DP1-ISO-837	823	-6.9	-9.4	-8.6	-10.2		1604	16	Aragonite	NA
	DP1-ISO-842	828	-6.2	-8.5	-7.9	-9.3		1616	16	Aragonite	IA
	DP1-859	830					1621	1621			
	DP1-ISO-847	833	-7.2	-9.1	-8.9	-9.9		1641	17	Aragonite	IA
	DP1-ISO-852	838	-5.6	-7.8	-7.3	-8.6		1673	17	Aragonite	NA
	DP1-ISO-857	843	-8.3	-9.0	-10.0	-9.8		1706	17	Aragonite	NA
DP1-UAL-865	DP1-ISO-865	851	-7.1	-8.9	-7.1	-8.9		1758			
	DP1-ISO-870	856	-6.7	-9.7	-8.4	-10.5		1791	17	Aragonite	NA
	DP1-ISO-875	861	-6.4	-9.0	-8.1	-9.8		1823	17	Aragonite	NA
DP1-UAL-880	DP1-ISO-880	867	-6.0	-8.3	-7.7	-9.1		1863	17	Aragonite	IA

UA Sample	UGA Sample	Position (mm)	$\delta^{13}\text{C}$	$\delta^{18}\text{O}$	Transformed	Transformed	^{230}Th	Calculated	Thin	Mineralogy	Fabric
ID	ID	from top)	VPDB	VPDB	$\delta^{13}\text{C}$ VPDB	$\delta^{18}\text{O}$ VPDB	Dates (BP)	Dates (BP)	Section #		ID
DP1-UAL-886	DP1-ISO-886	872	-6.9	-8.0	-8.6	-8.8		1895	17	Aragonite	NA
	DP1-ISO-891	877	-7.1	-8.2	-8.8	-9.0		1928	17	Aragonite	IA
	DP1-ISO-896	883	-7.0	-8.4	-8.7	-9.2		1967	17	Aragonite	IA
	DP1-ISO-905	892	-6.3	-8.5	-8.0	-9.3		2026	17	Aragonite	NA
	DP1-ISO-910	897	-4.3	-6.9	-6.0	-7.7		2059		Aragonite	
	DP1-ISO-915	902	-4.7	-7.9	-6.4	-8.7		2091	18	Aragonite	CA
	DP1-ISO-919	906	-4.0	-7.2	-5.7	-8.0		2117	18	Aragonite	CA
	DP1-ISO-924	911	-4.1	-8.0	-5.8	-8.8		2150	18	Aragonite	CA
	DP1-ISO-929	916	-5.1	-8.3	-6.8	-9.1		2183	18	Aragonite	NA
	DP1-ISO-935	922	-4.4	-8.0	-6.1	-8.8		2222	18	Aragonite	CA
	DP1-ISO-941	928	-3.1	-8.1	-4.8	-8.9		2261	18	Aragonite	CA
	DP1-ISO-947	934	-3.6	-7.7	-5.3	-8.5		2300	18	Aragonite	CA
	DP1-ISO-955	941	-4.2	-8.1	-5.9	-8.9		2346	18	Aragonite	CA
	DP1-ISO-960	946	-4.3	-8.0	-6.0	-8.8		2379	18	Aragonite	NA
	DP1-ISO-967	952	-5.4	-8.8	-7.1	-9.6		2418	18	Aragonite	NA
	DP1-ISO-973	958	-4.3	-7.2	-6.0	-8.0		2457	18	Aragonite	NA
	DP1-ISO-979	963	-4.6	-7.1	-6.3	-7.9		2490	19	Aragonite	CA
	DP1-ISO-985	968	-4.1	-8.1	-5.8	-8.9		2522	19	Aragonite	CA
	DP1-ISO-990	972	-3.0	-6.1	-4.7	-6.9		2548	19	Aragonite	CA
	DP1-ISO-995	977	-4.0	-7.5	-5.7	-8.3		2581	19	Aragonite	CA
	DP1-ISO-1001	983	-3.8	-8.1	-5.5	-8.9		2620	19	Aragonite	CA
	DP1-ISO-1006	988	-3.9	-7.9	-5.6	-8.7		2653	19	Aragonite	CA
	DP1-ISO-1012	994	-4.3	-7.1	-6.0	-7.9		2692	19	Aragonite	NA
	DP1-ISO-1018	1000	-4.3	-8.1	-6.0	-8.9		2731	19	Aragonite	NA
	DP1-ISO-1023	1005	-4.5	-7.9	-6.2	-8.7		2764	19	Aragonite	IA
	DP1-1003	1009					2790	2790			
	DP1-ISO-1030	1012	-4.9	-8.1	-6.6	-8.9		2809	19	Aragonite	IA
	DP1-ISO-1036	1017	-4.8	-8.5	-6.5	-9.3		2840	19	Aragonite	IA
	DP1-ISO-1042	1022	-4.7	-7.3	-6.4	-8.1		2872	19	Aragonite	IA
	DP1-ISO-1046	1026	-5.3	-7.4	-7.0	-8.2		2897		Aragonite	
	DP1-ISO-1051	1031	-4.0	-8.4	-5.7	-9.2		2929		Aragonite	
	DP1-ISO-1057	1036	-3.8	-7.9	-5.5	-8.7		2960	20	Aragonite	CA
	DP1-ISO-1062	1041	-4.6	-7.0	-6.3	-7.8		2992	20	Aragonite	NA
	DP1-ISO-1067	1046	-4.8	-6.7	-6.5	-7.5		3023	20	Aragonite	NA
	DP1-ISO-1072	1051	-4.7	-5.8	-6.4	-6.6		3055	20	Aragonite	NA
	DP1-1052	1056					3086	3086			CA
	DP1-ISO-1082	1061	-4.1	-7.3	-5.8	-8.1		3097	20	Aragonite	
	DP1-ISO-1087	1066	-4.5	-7.2	-6.2	-8.0		3107	20	Aragonite	CA
	DP1-ISO-1091	1070	-4.9	-8.2	-6.6	-9.0		3116	20	Aragonite	NA
	DP1-ISO-1096	1075	-5.4	-8.5	-7.1	-9.3		3126	20	Aragonite	IA
	DP1-ISO-1101	1080	-5.0	-6.7	-6.7	-7.5		3137	20	Aragonite	NA
DP1-UAL-1108	DP1-ISO-1108	1087	-5.8	-9.0	-7.5	-9.8		3152	20	Aragonite	NA
	DP1-ISO-1113	1092	-6.7	-9.8	-8.4	-10.6		3162		Aragonite	
	DP1-ISO-1118	1097	-5.7	-8.3	-7.4	-9.1		3173	20	Aragonite	NA
	DP1-ISO-1123	1102	-5.4	-8.2	-7.1	-9.0		3183	21	Aragonite	NA
	DP1-ISO-1128	1106	-5.2	-8.5	-6.9	-9.3		3192	21	Aragonite	IA
DP1-UAL-1133	DP1-ISO-1133	1111	-5.9	-8.8	-7.6	-9.6		3202	21	Aragonite	IA
DP1-UAL-1140	DP1-ISO-1140	1118	-5.5	-8.1	-7.2	-8.9		3217	21	Aragonite	MNA
DP1-UAL-1145	DP1-ISO-1145	1123	-6.2	-9.1	-7.9	-9.9		3228	21	Aragonite	IA
DP1-UAL-1149	DP1-ISO-1149	1127	-5.7	-8.0	-7.4	-8.8		3236	21	Aragonite	IA
DP1-UAL-1153	DP1-ISO-1153	1130	-5.3	-9.0	-7.0	-9.8		3243	21	Aragonite	MNA
DP1-UAL-1159	DP1-ISO-1159	1136	-6.1	-8.8	-7.8	-9.6		3255	21	Aragonite	NA
	DP1-ISO-1168	1144	-6.2	-9.2	-7.9	-10.0		3272	21	Aragonite	MNA
DP1-UAL-1173	DP1-ISO-1173	1149	-6.6	-8.2	-8.3	-9.0		3283	21	Aragonite	MNA
DP1-UAL-1182	DP1-ISO-1182	1158	-5.4	-8.7	-7.1	-9.5		3302	21	Aragonite	NA
DP1-UAL-1188	DP1-ISO-1188	1164	-5.8	-9.1	-7.5	-9.9		3315	22	Aragonite	IA
DP1-UAL-1193	DP1-ISO-1193	1169	-6.9	-9.2	-8.6	-10.0		3325	22	Aragonite	IA
DP1-UAL-1197	DP1-ISO-1197	1173	-5.2	-8.0	-6.9	-8.8		3334	22	Aragonite	NA
	DP1-ISO-1201	1176	-5.8	-7.9	-7.5	-8.7		3340	22	Aragonite	NA
DP1-UAL-1207	DP1-ISO-1207	1182	-6.1	-8.3	-7.8	-9.1		3353	22	Aragonite	NA
	DP1-1084	1185					3359	3359			

UA Sample	UGA Sample	Position (mm)	$\delta^{13}\text{C}$	$\delta^{18}\text{O}$	Transformed	Transformed	^{230}Th	Calculated	Thin	Mineralogy	Fabric
ID	ID	from top)	VPDB	VPDB	$\delta^{13}\text{C}$ VPDB	$\delta^{18}\text{O}$ VPDB	Dates (BP)	Dates (BP)	Section #		ID
DP1-UAL-1214	DP1-ISO-1214	1189	-6.5	-9.0	-8.2	-9.8		3410	22	Aragonite	IA
DP1-UAL-1218	DP1-ISO-1218	1193	-5.6	-9.3	-7.3	-10.1		3462	22	Aragonite	IA
DP1-UAL-1222	DP1-ISO-1222	1197	-5.1	-9.0	-6.8	-9.8		3513	22	Aragonite	NA
	DP1-1131	1202					3577	3577			
DP1-UAL-1239	DP1-ISO-1239	1213	-5.8	-8.1	-7.5	-8.9		3609		Aragonite	
DP1-UAL-1246	DP1-ISO-1246	1221	-6.7	-8.7	-8.4	-9.5		3633		Aragonite	
DP1-UAL-1250	DP1-ISO-1250	1225	-5.7	-7.9	-7.4	-8.7		3645		Aragonite	
	DP1-ISO-1255	1230	-5.6	-8.0	-7.3	-8.8		3659		Aragonite	
DP1-UAL-1262	DP1-ISO-1262	1237	-5.7	-8.9	-7.4	-9.7		3680		Aragonite	
DP1-UAL-1268	DP1-ISO-1268	1243	-6.0	-9.4	-7.7	-10.2		3698		Aragonite	
DP1-UAL-1274	DP1-ISO-1274	1249	-6.2	-9.3	-7.9	-10.1		3715		Aragonite	
DP1-UAL-1278	DP1-ISO-1278	1253	-5.6	-10.0	-7.3	-10.8		3727		Aragonite	
DP1-UAL-1283	DP1-ISO-1283	1258	-4.9	-9.0	-6.6	-9.8		3742		Aragonite	
DP1-UAL-1287	DP1-ISO-1287	1262	-5.3	-8.8	-7.0	-9.6		3754		Aragonite	
DP1-UAL-1292	DP1-ISO-1292	1267	-4.9	-7.4	-6.6	-8.2		3768		Aragonite	
	DP1-ISO-1296	1271	-5.4	-8.1	-7.1	-8.9		3780		Aragonite	
DP1-UAL-1300	DP1-ISO-1300	1274	-5.3	-8.1	-7.0	-8.9		3789		Aragonite	
DP1-UAL-1304	DP1-ISO-1304	1278	-5.4	-8.7	-7.1	-9.5		3801		Aragonite	
DP1-UAL-1306	DP1-ISO-1306	1280	-5.6	-8.6	-7.3	-9.4		3807		Aragonite	
DP1-UAL-1310	DP1-ISO-1310	1284	-5.7	-9.3	-7.4	-10.1		3818		Aragonite	
DP1-UAL-1314	DP1-ISO-1314	1288	-5.5	-9.4	-7.2	-10.2		3830		Aragonite	
	DP1-1189	1292					3842	3842			
DP1-UAL-1321	DP1-ISO-1321	1295	-5.6	-8.7	-7.3	-9.5		3851		Aragonite	
DP1-UAL-1326	DP1-ISO-1326	1300	-5.5	-8.2	-7.2	-9.0		3866	24	Aragonite	NA
	DP1-ISO-1331	1305	-5.6	-8.7	-7.3	-9.5		3881	24	Aragonite	NA
DP1-UAL-1338	DP1-ISO-1338	1312	-5.6	-8.2	-7.3	-9.0		3902	24	Aragonite	MNA
DP1-UAL-1344	DP1-ISO-1344	1317	-5.3	-7.9	-7.0	-8.7		3917	24	Aragonite	MNA
DP1-UAL-1349	DP1-ISO-1349	1321	-5.5	-7.6	-7.2	-8.4		3929	24	Aragonite	NA
DP1-UAL-1355	DP1-ISO-1355	1327	-5.6	-7.9	-7.3	-8.7		3947	24	Aragonite	MBNA
DP1-UAL-1359	DP1-ISO-1359	1331	-6.5	-8.3	-8.2	-9.1		3959	24	Aragonite	MNA
	DP1-1234	1335					3971	3971			
DP1-UAL-1366	DP1-ISO-1366	1338	-6.0	-8.6	-7.7	-9.4		3979	24	Aragonite	MNA
DP1-UAL-1370	DP1-ISO-1370	1342	-6.3	-8.0	-8.0	-8.8		3989	24	Aragonite	MBNA
	DP1-ISO-1374	1346	-6.5	-8.2	-8.2	-9.0		4000	24	Aragonite	MNA
DP1-UAL-1380	DP1-ISO-1380	1351	-6.0	-9.1	-7.7	-9.9		4013	24	Aragonite	MNA
DP1-UAL-1391	DP1-ISO-1391	1360	-6.5	-9.3	-8.2	-10.1		4036		Aragonite	
DP1-UAL-1396	DP1-ISO-1396	1365	-6.5	-8.8	-8.2	-9.6		4049		Aragonite	
DP1-UAL-1402	DP1-ISO-1402	1370	-6.1	-8.5	-7.8	-9.3		4062		Aragonite	
DP1-UAL-1407	DP1-ISO-1407	1374	-6.7	-8.5	-8.4	-9.3		4073		Aragonite	
	DP1-1285	1381					4091	4091			
DP1-UAL-1414	DP1-ISO-1414	1381	-6.1	-8.4	-7.8	-9.2		4091		Aragonite	
DP1-UAL-1419	DP1-ISO-1419	1386	-7.3	-9.1	-9.0	-9.9		4108		Aragonite	
DP1-UAL-1423	DP1-ISO-1423	1390	-7.3	-9.2	-9.0	-10.0		4122		Aragonite	
DP1-UAL-1428	DP1-ISO-1428	1395	-6.4	-9.0	-8.1	-9.8		4139		Aragonite	
DP1-UAL-1433	DP1-ISO-1433	1400	-6.1	-9.3	-7.8	-10.1		4156		Aragonite	
DP1-UAL-1439	DP1-ISO-1439	1405	-6.9	-9.5	-8.6	-10.3		4174	26	Aragonite	NA
	DP1-ISO-1446	1412	-5.4	-7.2	-7.1	-8.0		4198	26	Aragonite	IA
DP1-UAL-1450	DP1-ISO-1450	1416	-6.2	-8.4	-7.9	-9.2		4212	26	Aragonite	IA
DP1-UAL-1455	DP1-ISO-1455	1421	-5.3	-8.3	-7.0	-9.1		4229	26	Aragonite	IA
DP1-UAL-1461	DP1-ISO-1461	1427	-6.0	-8.7	-7.7	-9.5		4250	26	Aragonite	NA
	DP1-ISO-1466	1432	-6.5	-8.8	-8.2	-9.6		4267	26	Aragonite	MNA
DP1-UAL-1470	DP1-ISO-1470	1436	-5.9	-8.3	-7.6	-9.1		4281	26	Aragonite	
DP1-UAL-1475	DP1-ISO-1475	1441	-6.8	-8.8	-8.5	-9.6		4298	26	Aragonite	MNA
DP1-UAL-1480	DP1-ISO-1480	1446	-7.6	-10.0	-9.3	-10.8		4315	26	Aragonite	MNA
	DP1-ISO-1486	1452	-6.5	-8.8	-8.2	-9.6		4336	26	Aragonite	NA
DP1-UAL-1495	DP1-ISO-1495	1461	-6.3	-8.8	-8.0	-9.6		4367		Aragonite	
DP1-UAL-1499	DP1-ISO-1499	1465	-7.0	-9.2	-8.7	-10.0		4380		Aragonite	
DP1-UAL-1504	DP1-ISO-1504	1470	-6.0	-8.4	-7.7	-9.2		4398		Aragonite	
	DP1-1374	1473					4408	4408	27		MNA
	DP1-ISO-1508	1474	-7.0	-8.9	-8.7	-9.7		4410	27	Aragonite	MNA
DP1-UAL-1516	DP1-ISO-1516	1481	-6.4	-7.8	-8.1	-8.6		4425	27	Aragonite	MNA

UA Sample ID	UGA Sample ID	Position (mm from top)	$\delta^{13}\text{C}$ VPDB	$\delta^{18}\text{O}$ VPDB	Transformed $\delta^{13}\text{C}$ VPDB	Transformed $\delta^{18}\text{O}$ VPDB	^{230}Th Dates (BP)	Calculated Dates (BP)	Thin Section #	Mineralogy	Fabric ID
DP1-UAL-1520	DP1-ISO-1520	1485	-6.6	-7.9	-8.3	-8.7		4434	27	Aragonite	MNA
	DP1-ISO-1527	1492	-6.7	-9.2	-8.4	-10.0		4449	27	Aragonite	MNA
DP1-UAL-1531	DP1-ISO-1531	1496	-6.6	-9.3	-8.3	-10.1		4457	27	Aragonite	MNA
DP1-UAL-1536	DP1-ISO-1536	1500	-5.8	-8.4	-7.5	-9.2		4466	27	Aragonite	MNA
DP1-UAL-1547	DP1-ISO-1547	1511	-6.2	-8.8	-7.9	-9.6		4489	27	Aragonite	MNA
	DP1-B	1559					4592	4592			
	DP1-1475	1584					4614	4614			